THE ELECTRICAL PROPERTIES OF NANOSCALE PARALLEL SEMICONDUCTOR INTERFACES

Thesis by

Robert C. Rossi

In Partial Fulfillment of the Requirements

For the Degree of

Doctor of Philosophy

California Institute of Technology

Pasadena, California

2002

(Defended June 11, 2001)

This material is based upon work supported under a National Science Foundation Graduate Fellowship. Any opinions, findings, conclusions, or recommendations expressed in this publication are those of the author and do not necessarily reflect the views of the National Science Foundation.

Acknowledgments

My graduate career has differed from that of most of my peers in that I have spent it working alone on a single project. That said, the work presented here would not have been possible without the help of many others. I apologize in advance for the omissions I know I will make in my attempt to enumerate those who have contributed.

My research advisor, Nathan Lewis, entrusted me with an important but challenging project that he believed in. I thank him for allowing me to stick with it even when the going got tough and progress was nowhere to be found. Nate gave me a chance to make this project pay off, and offered me guidance without telling me what to do. I thank him for both his patience and impatience. I am happy to say that in the end I think we pulled it off. I am also indebted to Nate for his (eventual) understanding of my passion for teaching and his encouragement and support in pursuit of my dreams.

The National Science Foundation provided financial support for this work through grant CHE-99974562 and a Graduate Research Fellowship. I am thankful to our nation's taxpayers for their trust and I hope these were good investments…better, at least, than $525 military-issue toilet seats.

I met Brent Morgan and Karen Kavanagh at the University of California – San Diego when we attempted to look at my nanopatterned samples using their ballistic electron emission microscopy system. That investigation turned out to be a complete bust, but this was nonetheless the most scientifically productive trip I've ever taken. Brent and Karen helped me realize the folly of working with the Si/Au system and clarified several issues in silicide chemistry that proved essential to the eventual success of this project. At least as important, both shared with me a sense of perspective and vigor that I desperately needed at the time. I am particularly indebted to Brent for his hospitality while I was in San Diego and for his continued support and encouragement.

This work also benefited directly from the advice of Prof. R. P. Van Duyne of Northwestern University, who suggested we try nanosphere lithography, and of his student J. C. Hulteen, who revealed some limitations of the technique. The thousands of micrographs critical to this work would not have been possible without the tutelage of Guru Kumaraswamy, who taught me the power and limitations of atomic force microscopy and handed me the keys to a fully functional Beckman Institute Microscopy Center. Dr. Steve Barrett, the author of ImageSXM, made measuring electrode areas and particle sizes a relative breeze, and I would like to thank him and Wayne Resband for placing their computer code (ImageSXM/ImageNIH) in the public domain.

Chris Kenyon was completing his thesis when I arrived in the Lewis group as a puppy-eyed first year student. I wondered at the time why he was so grumpy. Now I understand completely. Despite the incredible pressure of completing his graduate work, Chris took the time to point out several critical issues I needed to understand if I was ever to get anywhere. I now realize what a difference a few moments of Chris' time made for me, and I have tried my best to emulate his good example in my twilight here.

My early years as a graduate student also benefited greatly from the mentoring and kindness of postdocs Mark Lonergan, Olaf Krüger, Steve Doig, and Marion Cass. Their emphasis on helping the lab as a whole, not just themselves, developed in me high expectations of postdoctoral scholars that none save Joel Haber and Glen Walker have subsequently managed to live up to. Senior graduate students Arnel Fajardo, Erik Severin, and Kathy Pomykal took time out of their busy lives to help me learn the ropes, make me laugh, and warn me of rocks ahead. I thank them for their warmth and wisdom, and for not laughing at me too hard. My graduate classmate Will Royea *did* laugh at me real hard, but coming from him it didn't sting. Will always made me laugh at least twice as hard as I ever managed with him, anyway. Will's snappy intelligence and common-sense attitude fueled and made productive many a late-night brainstorming session, and I couldn't have hoped for a better person to discuss science (as well as some really important stuff) with.

I owe a deep professional thanks to Ray Tung and his colleagues for writing a clear and coherent explanation of the pinch-off effect, and for sticking their necks out by making quantitative predictions about it for me to test. Until I met him this year, I'd always envisioned Ray as a cryptic theoretician. Discovering him to be an outgoing experimentalist, and a very nice guy to boot, led me to question some of my prejudices.

My close friends and family have seen me grow distant as a result of the focus I have put into my research as a graduate student. I am particularly thankful to my love, Alex, for her patience during my final year, and to my family for their boundless and unconditional support throughout my graduate career. My sister and brother have gone through important phases in each of their lives that I have largely missed, being trapped so far from home. I hope in the end I do not regret the tradeoffs I have chosen to make. Cynthia Kiser demonstrated by her example that it was possible to get through one's defense without turning into a monster, something I have reminded myself of many times over in the past few months, and I thank her for the inspiration. Cynthia and my other friends Len Flier, John Klemic, Brent Morgan, Leah and Ben Gordon, and Lowell Schwartz have been particularly good about staying in touch when I've been impossible to talk with, and I thank them for reminding me there's a world outside the confines of lab.

I dedicate this work to the scientific community, and in particular those folks in the Lewis group who find *Science* and *J. Phys. Chem.* a good read, with my thanks for the assurance that the advancement of science shall continue in their capable hands. Florian Gstrein and Agnes Juang have been good friends and colleagues and (lucky them) the job of playing the old fogy around here now falls to them. My thanks to Joe Nemanick for his interest in carrying on this research field; I hope in the end it proves as fruitful for him as it has for myself. A parting observation to any researcher reading this...nothing in lab is ever easy…and when it seems easy, it usually means you're missing something.

Abstract

Nanosphere lithography has been used to prepare a series of ordered, periodic arrays of low barrier height *n*-Si/Ni nanometer-scale contacts interspersed amongst high barrier height n-Si/liquid contacts. To form the arrays, crystalline bilayers of close-packed latex spheres were deposited onto (100)-oriented *n*-type single crystal Si surfaces. The spheres formed a physical mask through which Ni was evaporated to produce regularly spaced and regularly sized Si/Ni contacts. By varying the diameter of the latex spheres from 174 nm to 1530 nm, geometrically self-similar Si/Ni structures were produced having triangular Si/Ni regions with edge dimensions of 100 - 800 nm. The resulting Si surfaces were used as electrodes in contact with a methanolic solution of $LiClO_4$ and 1,1'-dimethylferrocene$^{+/o}$. The current-voltage and photoresponse properties of these mixed barrier height contacts were strongly dependent on the size of the Ni regions, even though the fraction of the Si surface covered by Ni remained constant. Electrodes formed from large-dimension Si/Ni and Si/electrolyte contacts behaved as expected for two area-weighted Schottky diodes operating independently and in parallel, whereas electrodes having nanoscale Si/Ni and Si/liquid contacts behaved in quantitative accord with effective barrier height theories that predict a "pinch-off" effect for mixed barrier height systems of sufficiently small physical dimensions.

Table of Contents

I. BACKGROUND

I.1 Motivation

Fossil fuels presently serve as humanity's principal primary energy source because they offer several important advantages over all competing primary sources. Foremost amongst these are their relatively low cost and the existence of a well-developed infrastructure for their extraction and utilization. The cost of producing a kilowatt of electricity from solar power has always far exceeded that of obtaining the same power from fossil fuels, and thus today, as in the past, the application of solar power as an anthropogenic primary energy source has been limited to specialized applications such as aerospace and to remote locations where there is no energy distribution infrastructure in place. There is a growing concern, particularly within the scientific community, that the rapid release of greenhouse gasses into the atmosphere, associated with our use of fossil fuels, may have a serious impact on our terrestrial environment. If this concern spreads to the world population in general, factors other than price may come to moderate the mixture of primary energy sources used by humans.[1] Even if this does not come to motivate actual change, however, our use of fossil fuels at the current rate is an unsustainable practice. While the timing is a subject of intense debate, there is no question that our planet's fossil fuel reserves are being consumed faster than they are being formed – and thus over time the real cost of energy derived from fossil fuel sources must eventually rise. At some point, other means of satisfying terrestrial primary energy demands will have to replace the burning of fossil fuels derived from ancient sources, and thus even today research is being done into how the cost of energy so generated might be reduced.

The direct conversion of sunlight into electricity and/or chemical fuels at efficiencies significantly superior to those attained by plants was realized some time ago, but the economic value of the energy so generated has been and remains small relative to the reasonably amortized cost of the solar energy conversion devices employed. Thus

research on solar energy conversion has focused on reducing the cost of these devices, while attempting to maintain acceptable energy conversion efficiencies. A significant portion of the cost of a solid-state photoelectric device is associated with the formation of the impurity profile inside it which allows it to function as a diode and thus produce electric power. The same result may be obtained in a far less expensive manner by moving away from a purely solid-state device to one involving a liquid medium containing a redox-active species. Such devices are called photoelectrochemical solar energy conversion devices, and they offer significant device cost advantages when employed in the generation of either electricity or fuels from solar energy.

A long-standing challenge in the development of practical photoelectrochemical solar energy conversion devices has been their long-term stabilization in realistic terrestrial environments. Silicon and most other mid-gap semiconductors otherwise ideal for solar photoelectrochemical applications readily corrode or passivate when used as photoanodes in the presence of either water or oxygen, both ubiquitous on the earth's surface. Most photocathodes capable of carrying out meaningful reductions plate out trace metals from any electrolyte that has not been rigorously purified, leading to marked reductions in their practical efficiencies. A variety of means for stabilizing semiconductor surfaces have been developed, including competing kinetically with undesired reactions, and protectively coating semiconductor surfaces with electrochemically stable materials. Both approaches are relevant to the fundamental investigations described herein.

In order for the desired reaction at a photoelectrode to compete kinetically with undesired side reactions, it must occur very rapidly. Given the inherent electrochemical properties of a given semiconductor surface, this requires finding a redox couple, having a suitable redox potential, which undergoes very rapid electron transfer at the native semiconductor surface. These simultaneous constraints typically limit the options to outer-sphere, one-electron couples with small reorganization energies, and even so the concentration of other electroactive species in the cell must be kept to a minimum. Rarely can

direct fuel-producing reactions be carried out subject to these constraints, as a given reaction is unlikely to be simultaneously thermodynamically and kinetically optimal at a given semiconductor surface. Were it possible to thermodynamically match a fuel reaction to a semiconductor without having to simultaneously settle for whatever kinetics are available at the native semiconductor surface, the prospects for practical, efficient photoelectrochemical cells would be markedly brighter.

If a material is to serve as a functional protective coating for a photoelectrode, it must protect the surface without acting as a major impediment to the passage of photons, and without hampering the semiconductor's ability to direct the flow of electrons. Metals figure prominently among the less vulnerable materials used to coat photoelectrochemical semiconductors, but they tend to fail in both respects. First, metal films tend to be relatively opaque to the transmission of light, reducing the efficiency of any photoelectric device on which they are employed. Second, and more problematically, metals are exceptionally unpolarizable materials. Thus even a thin metal film determines the band bending in a semiconductor/metal [SC/M] contact, and prevents electrochemical control (via solution composition) of the barrier height of the diode formed at a solid-liquid interface. Were SC/M barrier heights generally high, this would in fact be advantageous, but this is not the case. Rather, metals tend to exhibit barrier heights appreciably lower than theory would predict, and lower than those readily obtained at properly designed semiconductor/liquid contacts.

Some early photoelectrochemical work indicated that if the metal film on a semiconductor were made very thin – and thus discontinuous – electrochemical control of the band bending in the semiconductor could be maintained while the metal continued to protect the semiconductor surface from chemical degradation. Though extensive, research on this topic remains controversial because the vast majority of the semiconductor/electrolyte [SC/E] systems investigated have been aqueous and thus inherently unstable, and the structure of the metal films employed has not been well-defined.

However, models have been developed which provide some theoretical rationale for expecting that under certain conditions metals can be put on a semiconductor surface without completely losing electrochemical control of the junction energetics. (The history of these investigations is detailed in §I.3, and the models are explained in Section III.) Research and theoretical calculations performed by Adam Heller and his colleagues in the mid-eighties[2, 3] indicated that non-interconnected metal particles smaller than the wave-length of visible light are optically transparent. Such nanoscopic metal particles are also expected to allow the maintenance of electrochemical control over the barrier energetics of a parallel semiconductor/metal, semiconductor/electrolyte [SC/M|E] interface. Together, these ideas suggest the possibility of placing metal catalyst particles on semiconductor surfaces without disrupting the light absorption and charge separation functions of photoelectrochemical semiconductor/liquid junctions, enabling independent optimization of the thermodynamics and the kinetics of photoelectrochemical reaction systems.

I.2 Fundamentals

I.2.1 Semiconductor Heterojunctions and Interfacial Energetics[4-7]

Although theoretical descriptions of ideal semiconductor heterojunction interfacial energetics were advanced by Schottky[8] and Mott[9] in 1938, the search for ways to make junctions conform to these ideal expectations remains a challenge today. The contact potential difference, V_c, across a semiconductor heterojunction is equal in magnitude to the difference between the work function of the semiconductor and that of the contacting phase ($qV_c = |\phi_{sc} - \phi_{cp}|$). As shown in Figure 1, in the ideal case essentially the entire contact potential drops across the depletion region of the semiconductor, such that the band bending in the semiconductor at equilibrium (commonly referred to as the "built-in" voltage), U_{bi}, is equal to the contact potential (V_c).

Semiconductor/metal heterojunctions, the first to be thoroughly investigated, were generally found to display far weaker rectification than their work function differentials

suggested they should theoretically be capable of. The reason for this is a matter of some controversy even today, although it is generally agreed there are often multiple factors at work, their relative importance hinging on the conditions under which the SC/M contact is formed.

Currently, the most prominent explanations for non-ideal interfacial energetics and current transport properties at semiconductor heterojunctions are as follows:

1) An appreciable fraction of the contact potential drops across an insulating layer present between the contacting phase and the semiconductor; the magnitude of this effect increases with the work function differential and with the thickness of the oxide layer (Figure 2a).
2) A new compound with energetic states at a cluster of energies inside the semiconductor bandgap is formed at the interface. (Often this occurs as the result of a chemical reaction between the contacting material and the semiconductor.) These states ionize preferentially, being very close to the interface, and modify the potential drop over the semiconductor depletion region. The magnitude of this effect will vary with the work function differential, and will be most pronounced when the equilibrating Fermi level must move through the surface state energy[10] (Figure 2b).
3) Weak chemical bonds to the semiconductor form a set of interfacial states with a wide distribution of energies within the bandgap. These drop a portion of the contact potential proportional to the work function differential, provided they are uniformly distributed in energy. This can also occur as a result of "dangling bonds" or other surface bond states at the semiconductor surface (Figure 2c).

It should be emphasized that these effects commonly occur simultaneously, with the latter two leading to what has come to be called "Fermi level pinning," a weakened dependence of the rectification properties of a semiconductor heterojunction on the work function differential.

Although Fermi level pinning is not generally observed on highly ionic semiconductors, SC/M junctions involving intermediate bandgap semiconductors generally exhibit strong Fermi-level pinning.[11] Techniques have been found that can reduce the impact of the aforementioned phenomena,[12, 13] but the search for additional means to control the interfacial properties of semiconductor heterojunctions continues.

Initial work at semiconductor/electrolyte heterojunctions seemed to suggest that here too, interfacial energetics were commonly upset by Fermi level pinning.[14, 15] This was not universally true, however, with junctions as simple as Si/H_2O known, as early as 1960, to respond in a nearly ideal manner to changes in the interfacial work function differential.[4] A more immediate concern plaguing the early studies of SC/E junctions was the general instability of illuminated moderate bandgap semiconductors in solution, be this as a result of corrosion or oxidation (at *n*-type semiconductors) or the reductive plating-out of solids from solution (at *p*-type semiconductors). Although these problems have been overcome for specific systems, using non-aqueous solvents, kinetic competition, protective coatings, and other approaches, general methods for the long-term stabilization of moderate bandgap semiconductors in solution remain a topic of intense interest.

I.2.2 Photoexcitation and Separation of Charge Carriers

When a semiconducting solid is illuminated with photons of sufficient energy, electrons are excited from the ground state continuum of valence band orbitals into the delocalized band of conduction band orbitals. In the absence of an electric field, these electrons quickly relax to their ground states, returning to the (now positively charged) sites in the semiconductor lattice from which they came. (These positively charged ions in the lattice are commonly referred to as "holes.") Photocurrents and photovoltages are observed across semiconductor heterojunctions under illumination when photogenerated electrons and holes are separated by an electric field; such a field is naturally present at most semiconductor heterojunction interfaces,[16] its form governed by the criteria described in the preceding section. A schematic representation of this process appears in

Figure 3. Separated photogenerated charge carriers have a thermodynamic tendency to recombine, which can be harnessed to do useful work; this is the basis of photochemical and photoelectric conversion of solar energy.

I.2.3 Carrier Transport and Charge Transfer Kinetics

The issue of carrier transport is generally simplified by assuming one of two limiting cases. In semiconducting and conducting solids, electrons and holes move incredibly fast. Therefore, in the dark or under moderate illumination, carrier profiles in metals and semiconductors are generally assumed to conform to the local electric field, being essentially flat at all locations free of an electric field. Additionally, the relative carrier concentrations at any two points are simply related by a Boltzmann term incorporating the difference in electric potential between the two points. In contrast, charges in a liquid phase are associated with solvated ions, which move relatively slowly. As a result, their distributions are far more likely to reflect local generation or consumption rates, tempered only in part by diffusion, migration, and convection effects.

In actuality, the situations of interest in the research described here arise as a direct result of the fact that although charge carriers in a semiconductor such as silicon *do* have incredibly large mobilities, situations can arise where relative local carrier concentrations *are not* simply determined by local electrostatics. The rate at which charges "flow" over a potential maximum in a semiconductor is given by Bethe's thermionic emission theory.[17] The flux exhibits an exponential dependence on the local electric potential and can thus become quite small in the presence of strong electric fields. When a large potential barrier divides two regions of a semiconductor, the charge carriers in the two regions need not be in thermal equilibrium with each other.

A brief introduction to the topic of electron transfer across semiconductor heterojunctions is also in order, although the topic can not begin to be done justice here. For a more complete discussion, the reader is referred to the literature.[10, 18-20] The issue of interfacial charge-transfer kinetics arises primarily as a complicating factor in the work

discussed subsequently; however, in this respect it is quite important. Application of the Franck-Condon principle to charge transfer across a heterojunction suggests that the interfacial electron exchange rate should depend on the concentration of isoenergetic states on each side of the interface, and the ease with which electrons may move from states on one side of the interface to those on the other.

At semiconductor/metal heterojunctions, the density of isoenergetic states is extremely large for energies outside the bandgap. In contrast, the density of energetic states within the semiconductor bandgap is extremely small, nil in the ideal case. Further, in the absence of an intervening impurity layer, the isoenergetic states in the metal and those in the semiconductor are in such close physical proximity that their wavefunctions overlap appreciably. As a result, charge transfer across an SC/M interface is extremely rapid for energies outside the bandgap, but essentially forbidden for energies within it.

The situation is appreciably more complex at semiconductor/liquid heterojunctions. In the liquid, the density of states of a given energy and occupation is generally much smaller, and is determined by the concentration of species in the liquid phase, their solvent environments and vibrational states, and their standard potentials. The form of these dependencies are known, and have been developed into easily visualized form by Marcus, Gerischer, and others. For our purposes, it is sufficient to note that the rate of charge transfer to a species in solution is often the rate-limiting step in a photoelectrochemical process, and that in solution the electron transfer rate constants at the two band edges of a semiconductor often differ by many orders of magnitude. Whether electron transfer is dominated by exchange via the conduction band or via the valence band is contingent on many factors, but an important property of SC/E interfaces is that the solution identity plays a key role in determining interfacial charge transfer kinetics, whereas the metal used as a contacting phase in an SC/M junction will have essentially no effect on the kinetics of charge transfer.

I.3 History

I.3-1 Solid-State

The electrical behavior of solid-state SC/M contacts having spatially inhomogeneous barrier heights has attracted much theoretical,[21-32] computational,[33-42] and experimental[27, 28, 43-66] attention.[67-70] Of specific interest is the regime in which the scale length of the barrier height nonuniformities is comparable to or smaller than the depletion width of the semiconductor. In this regime, analytic theories[21, 22] and numeric simulations[33-35] have indicated that the current density through small, low barrier height regions on the surface of an otherwise high barrier height SC/M contact should be a strong function of the band bending in the semiconductor and of the spatial dimensions of the low barrier height regions. Specifically, the "effective" barrier height of such regions is predicted to be much higher than the barrier height that would be obtained with nonuniformities of larger spatial dimensions on an otherwise identical SC/M interface. Freeouf et al. discussed this effect in 1982[33] and coined the term "pinch-off" to describe the modulation of electric potential profiles behind nanometer-scale barrier height spatial nonuniformities in a SC/M contact. Tung and co-workers subsequently performed more detailed numeric simulations[34] and Tung developed a set of analytic equations[21, 22] to describe the current density-voltage [J-V] behavior of pinched-off systems. Based on these results, Tung and co-workers argued that microscopic variations in local barrier heights could explain several widely observed anomalies of ostensibly homogeneous SC/M contacts, including the T_o effect,[71, 72] the frequent observation of diode quality (ideality) factors appreciably greater than unity,[21] and the discrepancies typically observed between Schottky barrier heights measured by differential capacitance-voltage and J-V techniques.[46, 73] Subsequent ballistic electron emission microscopy [BEEM] studies have clearly indicated that the barrier height across SC/M contacts is often highly spatially inhomogeneous,[60-68] and with few exceptions[40-42, 74, 75] the pinch-off model developed by Tung[21, 22] has been found to provide an adequate explanation of the

behavior of such contacts.[30, 55, 58, 59, 76, 77] Efforts have also been made to directly verify the existence of the pinch-off phenomenon using BEEM[78] and dark J-V measurements at different temperatures[43] at intentionally inhomogeneous Schottky contacts prepared using two distinct contacting metals [SC/M_1|M_2 interfaces].[66] These studies provided strong qualitative support for the pinch-off hypothesis, but were quantitatively limited by a lack of information about the physical extent of the low-barrier-height contacts and of their unperturbed barrier heights.

I.3-2 Semiconductor Electrochemistry

Concurrent with the aforementioned studies of SC/M interfaces, electrode surfaces possessing lateral variations in local barrier height, usually arising from the deposition of metal particles onto semiconductor photoelectrodes, have attracted significant attention in the electrochemical literature.[79-101]

I.3-2.1 Initial Discovery, Early Studies, and Unsatisfying Explanations

In 1976, Nakato and Tsubomura[102]reported that thin metal films formed by the rapid evaporation of Au on *n*-GaP produced electrodes whose electrochemical behavior in aqueous electrolyte solutions buffered to pH 4.7 differed markedly from that of otherwise similar electrodes formed by slower metal evaporation. They speculated that the rapidly evaporated films were porous, their constituent particles separated from the GaP by thin interfacial gold oxide layers that formed upon immersion of the electrode in aqueous solution. They suggested these particles scavenged photogenerated holes from the GaP surface, protecting it from oxidation in the normally corrosive aqueous solution.

Soon after, Pinson[103] and Wilson et al.[104, 105] reproduced Nakato and Tsubomura's results, but on the basis of direct measurements of the gold overlayer's potential they concluded that no chemical reaction could be taking place at the metal surfaces in the solutions used. Instead, they suggested the porous metal acted as a diffusion barrier, increasing the etch rate of photochemically grown oxide at the electrode surface such that it did not passivate but instead exhibited a large, non-decreasing

photocorrosion current. Wilson et al. drove their point home by producing similar results by coating *n*-GaP electrodes with porous films of insulating lacquer.

Subsequently, some of the work involving metal-coated semiconductors immersed in electrolyte solutions [SC/M/E junctions] focused on semiconductor stabilization, using thin but non-porous metal layers forming pinned SC/M junctions, with the contacting solutions used solely to overcome the high resistivity of the optically thin metal films.[106-108] More extensively, SC/M and SC/E junctions operating in parallel on the same surface (SC/M|E junctions) were employed in attempts at catalysis,[86, 97, 109-113] utilizing extremely small metal particles electrodeposited onto semiconductors from aqueous solutions; these particles did not seem to significantly modify the thermodynamics of the semiconductor/liquid interfaces whose interfacial reactions they served to catalyze. Although several explanations were advanced for the fact these deposited metal particles did not dominate the electrical character of the junctions, the reason for this phenomenon was not the subject of central interest in these studies.

Nakato and Tsubomura revisited this subject in 1982, looking at metal films on *n*-TiO_2, for which photocorrosion is not a concern.[114] They concluded that the barrier height at TiO_2/Au and TiO_2/Pd junctions increased appreciably under illumination in 1N $NaOH_{(aq)}$, provided that such junctions were formed with porous metal films. They attributed this, as they had in 1976, to the growth of thin oxide layers at the SC/M interfaces under illumination.

Subsequently, Adam Heller and his colleagues investigated the electrocatalytic[84, 115] and optical properties[2, 3] of noble metal deposits on InP electrodes in contact with aqueous acidic electrolytes.[116] They specified large barrier heights and low surface recombination rates at catalytic SC/M interfaces as necessary conditions for the success of SC/M|E catalytic systems.[84] That evidence for a high barrier was found at even the *p*-InP/Pt junction, which is normally ohmic, was explained by a change in the surface dipole component of the work function of the metal catalyst upon exposure to

hydrogen, and supported by a demonstration of this occurring in a dry H_2 gas atmosphere.[116] Although they provided strong support for their conclusions, subsequent investigations by the same authors at other metal-covered semiconductors suggested this explanation could not be generalized beyond the *p* InP/M system.[116, 117]

I.3-2.2 Parallel Nanocontacts Revisited: A New Model

In 1985 Nakato and Tsubomura returned to the topic of SC/M|E junctions, presenting a new theoretical explanation for the results they had obtained at discontinuous metal film-covered semiconductors over the past decade.[118] Their theory explained how, for certain geometries, small parallel nanocontacts could have a minimal effect on the macroscopically apparent band bending in the semiconductor, while still mediating charge transfer and thus impacting the macroscopic operational behavior of the electrode. Although their first attempt at explaining this new theory was rather obfuscatory, clarification was provided in later papers.[119, 120] Their theory is qualitative, but otherwise effectively identical to that described in Section III.

In their 1985 paper and in subsequent work, Nakato, Tsubomura, and their co-workers performed experiments that supported, albeit did not rigorously test, their new theory.[119-127] They demonstrated that while the photoelectrochemical behavior of semiconductor electrodes covered with large metal islands did not respond to changes in the redox potential of the solution in which they were immersed, the behavior of similar electrodes covered with extremely minute metal islands (obtained in a variety of ways) did respond to such changes – although not always in an ideal manner. Light-induced charging of the metal particles and elevated zero-point energies in quantized potential wells,[118, 119, 123, 126] as well as electrostatic arguments analogous to the pinch-off effect,[80, 120, 127, 128] were invoked to account for the J-V behavior of such systems.

I.3-2.3 SC/M|E Research in the Lewis Group

In 1988, Amit Kumar attempted to reproduce the results reported by Nakato et al. in their 1985-7 papers.[129] He encountered rapid passivation in aqueous solutions, and was unable to reproduce the stabilization properties described by Nakato et al. for any electrode not displaying typical "pinned" SC/M junction behavior; even when he employed samples provided by Tsubomura himself. Experiments in non-passivating media, coupled with energy dispersive X-ray and scanning electron microscopy analyses, suggested that large photovoltages were only observed for those electrodes whose deposited metal was completely removed by processing steps aimed at making the deposited metal layers "discontinuous."

The viability of Nakato and Tsubomura's reported 680+ mV open-circuit voltage, V_{oc}, values was also called into question, in light of limitations on effective minority carrier diffusion lengths imposed by the physical dimensions of semiconductor wafers. In the thin Si wafers typically used in work such as this, the presence of an ohmic contact covering the back surface and the absence of an electric field in the bulk of the semiconductor limit effective minority carrier diffusion lengths to less than half the wafer thickness, irrespective of the quality of the semiconductor crystal used in preparing the electrode. A minority carrier in the field-free bulk at the center of the semiconductor wafer has an equal probability of meandering to the ohmic back contact, where it is guaranteed to recombine, as it does of reaching the edge of the depletion region. Hence it may be said that thin, indirect-bandgap semiconductor electrodes made from high-quality single-crystal materials are in fact "back contact recombination limited." Application of this principle to the results of Nakato and Tsubomura suggests that unless their Si wafers were several millimeters thick, their cells somehow overcame this limitation.[129] Si is very rarely found cut into such thick wafers. An alternative explanation for these large V_{oc} values is the contribution of a corrosion potential to the measured V_{oc}.

It should be noted that Nakato and Tsubomura's large V_{oc} values might be seen as more tenable if their electrodes had small ohmic back contacts, not covering the entire back surface of their electrodes. If the probability of minority carriers "bouncing off" the back of the semiconductor wafer were non-zero, the "back contact recombination" limit might be overcome to some extent. Nonetheless, Kumar's results raised serious questions within our research group about the validity of both the experimental results and the theoretical explanation provided by Nakato and Tsubomura concerning parallel nanocontacts to semiconductor substrates.

These results did not quench our interest in the intriguing theoretical ideas advanced by Nakato and Tsubomura, however. The research work described herein evolved from a research proposal advanced in 1991 by Ming Tan, another former researcher in our laboratory.[130] She made quantitative estimates of the size of metal nanocontacts needed on a SC/M|E surface to enter the interesting theoretical regimes predicted by Nakato and Tsubomura's theory, and proposed testing these predictions in non-corrosive electroactive solutions using semiconductor electrodes patterned with metallic nanocontacts formed by electron beam lithography. Work was subsequently performed in our laboratories by Christopher Karp along exactly these lines,[131] but the results he obtained were inconclusive. Karp observed behavior in concordance with Tan's predictions at *n*-Si/Au|E junctions, but obtained results contradicting theoretical expectations at *n*-Si/Pt|E junctions. While interlayer oxide formation would explain the increase in apparent leakage current that Karp observed upon immersing his *n*-Si/Pt|E electrodes in solution (the photocurrent collection efficiency improved at short circuit by the low-resistance Si/E pathways only available in solution), it would not readily explain the low V_{oc} values he observed at nanopatterned Si/Pt|E electrodes. Because of the expense involved in preparing nanopatterned electrodes by electron-beam lithography, and the lack of a clear and conclusive result from Karp's attempt, an alternative means of preparing electrodes suitable for these investigations was sought.

I.3-2.4 Recent SC/M|E Research

Since 1994, Nakato and his co-workers have verified that the colloidal Pt particles they use in stabilizing Si surfaces in aqueous solution are not removed during their electrodes' preparation or electrochemical characterization.[132] They have also attempted to use Langmuir-Blodgett techniques to put down organized patterns of colloidal Pt particles on *n*-Si.[132] Unfortunately, the films thus obtained have been disorganized, and formed using polymer-stabilized colloids. The latter fact implies that Si/surfactant/Pt nanocontacts of an unpredictable nature were formed, making interpretation of the results obtained from these systems nebulous. This was stated explicitly in a more recent paper,[133] where several other issues of concern were also addressed. More tenable open circuit photovoltages (≈ 630 mV) were reported, and the inexplicably large photovoltages (680+ mV) previously reported were described as difficult both to explain and to reproduce. Hole diffusion lengths were measured and found to be independent of metal coverage and nearly equal to half the thickness of the silicon wafers used. The photovoltage temperature dependence of these systems was also reported, and suggested these systems to be bulk-recombination limited, or nearly so.

In the mid-1990's, Dieter Meissner and his co-workers studied the effects of colloidal gold deposits on aqueous p-GaAs electrodes.[134, 135] They observed results that could not be interpreted in terms of two types of semiconductor heterocontacts behaving independently and in parallel, the classic expectation for parallel contacts on a semiconductor surface. More recently, Hiesgen and Meissner have used photocurrent scanning tunneling microscopy[136] to investigate the local barrier heights around copper particles electrodeposited onto WSe_2.[137] These measurements demonstrated a size dependence in the barrier heights of nanoscopic WSe_2/Cu Schottky contacts, though the nature of the WSe_2/Cu junctions was not fully understood and particle charging was again suggested as a possibility.

I.3-3 Historical Synopsis

Given the extensive history of parallel semiconductor heterocontact systems, it is worthwhile to attempt to summarize the current status of research on the subject. Experimental observations have been made at parallel nanocontact systems, in both the solid state and photoelectrochemical literature, that seem to defy explanation on the basis of conventional models[44] which expect parallel semiconductor contacts to behave independently of one another. A new model has been developed (independently in the two fields, it seems) to explain these observations. (This model will be subsequently referred to as the "pinch-off," or "interacting contact," model.) The pinch-off model applies to parallel heterocontacts that are extremely small, smaller than the expected large-structure depletion widths of the heterojunctions in question, and is described in Section III. (It is best viewed as a new understanding of the consequences of presently accepted semiconductor heterojunction theory, rather than as a novel theory in its own right.) The pinch-off model has been shown to account for some previously unexplained observations, and has also been found to agree qualitatively with most experimental observations made subsequent to its introduction. However, there has not been a well-designed experiment performed specifically to put this new model to a quantitative test. Where such experiments have been attempted, they have failed to be conclusive because key variables such as the contact area and the barrier height of the constituent contacts have not been independently determined and have had to be assumed in order to attempt to model the interfacial transport properties. In many SC/M|E systems, the inherent stability of the component contacts has not generally been demonstrated, a source of additional concern in interpreting those results.

II. INTRODUCTION

II.1 Prospects

Photoelectrode stability is typically enhanced when continuous layers of metal are coated onto semiconductor surfaces; however, recombination is concomitantly increased due to the facile thermionic emission of majority carriers over the low SC/M barrier.[84, 110] Reducing the coverage of metal reduces recombination but also reduces the fraction of the surface kinetically stabilized against corrosion and passivation.

The pinch-off effect might prove highly advantageous in the application of semiconductor electrodes to photoelectrochemical energy conversion.[127, 135] Dense arrays of nanometer-sized metallized regions operating in the pinch-off regime might be expected to retain most of their catalytic functionality without significantly disrupting the rectification properties of a high barrier height SC/E contact covering the majority of a semiconductor surface.[120] At a pinched-off SC/M|E contact, majority carriers would not experience the low barrier height characteristic of a macroscopic SC/M contact, but would instead experience the relatively high barrier height imposed by the surrounding SC/E contact. While the potential profile responsible for this will also tend to push photogenerated minority charge carriers to the semiconductor surface rather than into the metal particles, the activation barrier for a majority carrier transferring from the semiconductor surface into a metal particle is relatively small, and the transfer should be facile. The continuum of energetic states available in any metal suggests that unless the metal particles charge appreciably, the concentration of majority carriers in the metal particles should vastly exceed that at the semiconductor surface. As a result, the rapid interfacial transfer of minority charge carriers from the semiconductor to the metal and through the metal to the redox species of interest should readily occur, with metal capable of performing an electrocatalytic role. The pinched-off metal contacts would thereby

provide a facile path for directing minority carriers to participate in desirable, possibly multi-electron transfer, interfacial redox processes.

If the pinch-off effect can be exploited, semiconductor electrodes coated with nanoscopic metal particles could be made to effectively direct minority carriers toward catalytic metal sites without incurring the majority carrier recombination effects that would otherwise deleteriously affect the properties of a semiconductor interface having an appreciable fraction of its area covered with (low barrier height) metal contacts. The metal could be chosen purely for its electrocatalytic suitability, without regard for the rectifying properties of the SC/M contact; even contacts that would normally be ohmic could be made strongly rectifying if the contacts were nanoscopic and the surrounding SC/E interface was strongly rectifying.

II.2 Objectives

A quantitative test of the pinch-off phenomenon requires a spatially nonuniform rectifying contact system composed of two stable, well-defined types of contacts having known and controllable dimensions. In addition, the difference in barrier height between the two types of contacts should be sufficiently large that the putative pinch-off effect can be readily observed using conventional interfacial transport measurements on macroscopic electrodes. It is desirable to prepare and electrically characterize structures that consist entirely of each individual contact type in a manner identical to that used in fabricating and analyzing the mixed contact structures. Direct experimental observations of the behavior of these characteristic electrodes could then provide the input parameters for prediction of the behavior of the spatially nonuniform mixed contact systems within the framework of the pinch-off model.

II.3 Approach

The approach described herein involves the formation of ordered, periodic arrays of low barrier height Ni contacts on an etched (100)-oriented crystalline *n*-Si surface.

"Nanosphere" (or "natural") lithography provides a facile method for producing self-similar patterns of metal that scale with the size of the microspheres employed in the lithographic process.[138, 139] The lithographic step is followed by the formation of a Si/liquid contact, which produces high barrier height regions on the unmetallized portions of the surface and which also forms a massively parallel electrical contact to the Ni features.

n-Si/Ni diodes are poor rectifiers, having room-temperature exchange current densities, J_o, on the order of 10^{-4} A·cm^{-2}; these exchange currents are dominated by thermionic emission over a 0.6 V barrier height, Φ_B.[140, 141] The ability of Ni to form silicide contacts at low temperatures[142] provides strong mechanical adherence, stability in electronic behavior over time, and reproducibility in barrier height over multiple experiments.[143] A solution of 1,1'-dimethylferrocene/dimethylferrocenium [$Me_2Fc^{+/o}$] in methanol forms a high (≈ 1.0 V) barrier height contact at *n*-Si[144-146] and provides a convenient second component to form the structured nonuniform barrier height electrode. The barrier height of a Si/CH_3OH–$Me_2Fc^{+/o}$ interface is large enough that the rate of thermionic emission over the potential barrier is negligible relative to other recombination rates in the semiconductor.[101, 144, 147] $Me_2Fc^{+/o}$ competes effectively with oxidation of *n*-Si under illumination,[101, 148] providing an electrochemical contact that is stable over long time periods when care is taken to exclude water and oxygen from the nonaqueous electrochemical cell.

In the absence of interaction between the two different barrier height regions, one would expect a Ni contact covering as little as 1% of an *n*-Si surface to have a significant deleterious effect on the photoresponse of an *n*-Si electrode in contact with CH_3OH–$LiClO_4$–$Me_2Fc^{+/o}$. In contrast, if the pinch-off effect were operative, then theoretically > 10% of the surface could be covered with metal without significantly affecting the majority carrier recombination current density at the semiconductor surface.

III. THEORY

III.1 Tung's Pinch-Off Model

III.1-1 Dipole Layer Perturbation Approach

Tung's perturbation-theory approach to calculating the electric potential field in a semiconductor behind a contact having a laterally inhomogeneous surface potential, U_s, is summarized briefly in this section.[21, 22] The electric potential in the bulk of the semiconductor is chosen as the zero for the electric potential scale, and throughout this work the electrochemical-standard sign conventions described in Appendix X will be employed.[149] Starting from a nominal band bending in the semiconductor, U_{bb}, a perturbation, $\delta(x, y)$, is chosen such that the actual electric potential at any point along the semiconductor surface is given by

$$U_s \equiv U(x, y, 0) = U_{bb} + \delta(x, y) \tag{1}$$

(This perturbation may be viewed as an oriented dipole layer, located at the semiconductor surface, superimposed on an interface with a uniform surface potential U_s.) Employing the depletion approximation, the electric potential, $U(x, y, z)$, within the depletion region of the semiconductor ($0 < z < W$) is then well-described by the expression

$$U(x,\ y,\ z) \ = \ U_{bb}\left(1 - \frac{z}{W}\right)^2 + \iint \frac{\delta(x, y)}{2\pi} \frac{z}{\left[z^2 + (x_1 - x)^2 + (y_1 - y)^2\right]^{3/2}}\, dx_1\ dy_1 \tag{2}$$

where W is the depletion width in the semiconductor when the band bending is U_{bb}, all electric potentials are measured relative to that of the semiconductor bulk, and the axes are oriented as shown in Figure 4a. The depletion width, W, in equation 2 is given by

$$W \ = \ \sqrt{\frac{2\,\varepsilon_s\,U_{bb}}{q\,N_X}} \tag{3}$$

where ε_s is the dielectric permittivity of the semiconductor (1.05×10^{-12} Coulombs·V^{-1}·cm^{-1} for Si), q is the elementary charge, and N_X is the majority carrier dopant density in the semiconductor.

When the surface potential is uniform everywhere except within a circular patch of radius R_o centered at the coordinate origin, within which the surface potential has a uniform value of $U_{bb} - \Delta$ (Figure 4b), equation 2 can be translated into cylindrical coordinates and simplified (details are given in Appendix D) to yield the following:

$$V(\rho,\ z) \ = \ V_{bb}\left(1 - \frac{z}{W}\right)^2 - \frac{\Delta}{2\pi}\int_0^{2\pi}\int_0^{R_o} \frac{\rho_1\ z}{\left[z^2 + \rho^2 + \rho_1^2 - 2\rho\rho_1\cos(\theta_1)\right]^{3/2}}\ d\rho_1\ d\theta_1 \tag{4}$$

Numeric integration of this expression under the conditions manifest in the experimental portion of this work produces the potential contours shown in Figure 5. The modulation of potential profiles within a model SC/M|E system, based on numeric solution of this equation, is demonstrated in Figure 6.

The potential along the z axis is given by the following expression:

$$U(0,\ z) \ = \ U_{bb}\left(1 - \frac{z}{W}\right)^2 - \Delta\left(1 - \frac{z}{\sqrt{z^2 + R_o^2}}\right) \tag{5}$$

A low barrier height contact is said to be pinched-off when, in moving from the bulk of the semiconductor to the surface behind the low barrier height patch, a majority charge carrier must overcome a potential barrier larger than that present at the interface. A band diagram applicable to this scenario appears in Figure 7. Mathematically, pinch-off occurs when the electric potential exhibits a local maximum along $\rho = 0$ in $(0 \le z \le W)$. Analysis of the derivative of equation 5 with respect to z yields

$$\frac{\Delta}{U_{bb}} \ > \ \frac{2\,R_o}{W} \quad \Rightarrow \quad R_o \ < \ \frac{W\,\Delta}{2\,U_{bb}} \tag{6}$$

as the critical condition for manifestation of the pinch-off effect. Pinch-off occurs when the difference between the two barrier heights, Δ, is large relative to the band bending in the semiconductor, and/or when the physical size of the low barrier height contact is small compared with the depletion width.[21]

III.1-2 The Point Dipole Approximation

Tung has also developed an analytic treatment to describe the electrical behavior of a small, isolated, low-barrier height region on a semiconductor surface otherwise covered with a high-barrier height contact.[21, 22] The situation of relevance to the present work is that of a Schottky (SC/M) contact to an *n*-type semiconductor containing a circular low barrier height patch (or "dot") of radius R_o situated on a uniformly high barrier height field (Figure 4c). Tung demonstrated that the peak potential behind such a contact can be effectively predicted for highly pinched-off dots by modeling the dot with a single point dipole, as opposed to with an oriented dipole layer. The point dipole employed has a total moment equal to that of the dipole layer it replaces, and serves as an adequate surrogate at points reasonably distant from the interface. When the point-dipole approximation is employed, the electric potential along the z axis is given by the following:[34]

$$U(0, z) = U_{bb}\left(1 - \frac{z}{W}\right)^2 - \Delta\left(\frac{R_o^2}{2\,z^2}\right) \qquad (7)$$

For strongly pinched-off dots, this approximation is reliable at the point where the electric potential reaches its local maximum, and the thermionic emission current from the low barrier height region is effectively controlled by this peak potential. The analytic expression for the approximate current through a dot, cast in terms of a thermionic emission current over an effective barrier height, Φ_{eff}, and through an effective contact area, S_{eff}, is

$$I_{dot} = I_{o,\,dot}\left[1 - \exp\left(\frac{-q\,V_{app}}{A_{dots}\,k\,T}\right)\right] \qquad (8)$$

$$I_{o,\ dot} = A^{**}\ T^2\ S_{eff}\ \exp\left(\frac{-q\,\Phi_{eff}}{k\,T}\right) \tag{9}$$

$$S_{eff} = \frac{4\,\pi\,\gamma\,\eta^{2/3}\,k\,T}{9\,q\left(U_{bb}\right)^{2/3}} \tag{10}$$

$$\Phi_{eff} = \Phi_B^o - \frac{\gamma\left(U_{bb}\right)^{1/3}}{\eta^{1/3}} \tag{11}$$

where the barrier height of the region around the dot is Φ_B^o while that of the dot itself is $\Phi_{B,\ patch}$, k is the Boltzmann constant, T is the temperature in Kelvins, q is the fundamental charge, A_{dots} is the diode quality (ideality) factor of a large homogeneous SC/M contact identical to that constituting the dot, and A^{**} is the effective Richardson constant. The other variables in these expressions are defined as follows:

$$\Delta \equiv \Phi_B^o - \Phi_{B,\ patch} \tag{12}$$

$$\gamma \equiv 3\left(\frac{R_o^2\,\Delta}{4}\right)^{1/3} \tag{13}$$

$$\eta \equiv \frac{\varepsilon_s}{q\,N_D} \tag{14}$$

$$U_{bb} = \Phi_B^o - V_n + V_{app} \tag{15}$$

In these equations and those that follow, N_D, N_C, and ε_s are the *n*-type semiconductor's donor density, effective density of states in the conduction band, and dielectric permittivity, respectively, while V_{app} is the external potential applied across the junction. The quantity qV_n is the energy difference between the Fermi level and the conduction band energy minimum in the bulk of the *n*-type semiconductor, given by

$$qV_n = k\,T\,\ln\left(\frac{N_C}{N_D}\right) \tag{16}$$

Note that Φ_{eff} and S_{eff} are both dependent on applied potential in that they vary with the band bending in the semiconductor, U_{bb}. The current through the low barrier height patch

is expected to exhibit a diode quality factor that varies with U_{bb}, and thus with applied bias:

$$A_{observed} = A_{dot} + \Gamma \tag{17}$$

$$\Gamma \equiv \left(\frac{R_o^2 \, \Delta}{4 \, \eta \, U_{bb}^2} \right)^{1/3} \tag{18}$$

The model presented in this section was developed to describe abrupt SC/M junctions having locally varying Schottky barrier heights. As such, a diode quality factor of $A_{dot} = 1$ was assumed, and thermionic emission was assumed to be the dominant recombination mechanism at all points on the surface under all bias conditions.

III.2 Modification of Tung's Model to Describe SC/M|E Junctions

The solid/liquid parallel heterojunction (SC/M|E) electrodes investigated in this work differ in several important respects from the microscopic Schottky barrier regions described in Tung's model. Equation 8 describes the current expected to flow through a single low-barrier height patch – in our case a single Ni dot on the *n*-Si surface. A straightforward extension of this equation to describe measurements performed on macroscopic electrodes populated with large quantities of dots is obtained by replacing the effective area term (S_{eff}) with an effective area fraction, f_{eff}, defined as

$$f_{eff} = \text{Effective Area Fraction} \equiv S_{eff} \, \rho_{dots} \tag{20}$$

where S_{eff} is the effective area of each dot, as defined in equation 10, and ρ_{dots} is the number of Ni dots per unit area found on the surface of a nanopatterned electrode. The resulting expression describes the contribution of the metal dots to the total current through a nanopatterned electrode:

$$\begin{aligned} J_{dots} &= \frac{\text{Total current through the metal dots}}{\text{Total projected area of the electrode}} \\ &= J_{o,\,dots} \left[1 - \exp\left(\frac{-q \, V_{app}}{A_{dot} \, k \, T} \right) \right] \end{aligned} \tag{21}$$

where $$J_{o,\ dots} = A^{**}\ T^2 \left(S_{eff}\ \rho_{dots}\right) \exp\left(\frac{-q\ \Phi_{eff}}{k\ T}\right) \quad (22)$$

Generally the current through the metal dots dominates the total current through an SC/M|E electrode, but when pinch-off is extreme, the current associated with the unmetallized portions of the electrode makes an appreciable contribution to the total interfacial charge carrier flux. To account for this contribution, the expression for the total current density expected at a nanopatterned electrode[21] should include a term, J_{bare}, accounting for the current through the unmetallized portions of the electrode. This term can be calculated based on the observed behavior of a homogeneous bare (SC/E) electrode, weighted by the actual fraction of the nanopatterned electrode that is bare, $(1 - f_{actual})$:

$$\begin{aligned} J_{bare} &= \frac{\text{Total current through the unmetallized portions of electrode surface}}{\text{Total projected area of the electrode}} \\ &= J_{o,bare}\left[1 - \exp\left(\frac{-q\ V_{app}}{A_\ell\ k\ T}\right)\right] \end{aligned} \quad (23)$$

where

$$J_{o,\ bare} = (1 - f_{actual})\ J_{o,\ \ell} \quad (24)$$

$f_{actual} \equiv$ Actual fraction of electrode surface covered by metal

$J_{o,\ \ell} \equiv$ Observed exchange current density at homogeneous liquid contact

and $A_\ell \equiv$ Observed diode quality factor at homogeneous liquid contact

This approach effectively assumes that the electrical behavior of the bare portions of the nanopatterned electrodes is unaffected by the presence of the metal islands, and that the metal dots are far enough apart that they do not interact with each other.[21]

Additional considerations must be introduced to account for the properties of the *n*-Si/CH_3OH–$Me_2Fc^{+/o}$ contacts used in this work. As an *n*-type semiconductor contact is exposed to solutions with increasingly positive redox potentials, the size of the depletion region in the semiconductor grows correspondingly larger. However, a point is eventually reached at which any further potential drop across the semiconductor causes

ionization of the lattice atoms at the semiconductor surface, with essentially no further growth of the depletion region.[150, 151] Surface transconductivity measurements have demonstrated that the CH_3OH–$Me_2Fc^{+/o}$ contact induces strong carrier inversion in *n*-Si under equilibrium conditions.[144] The depletion width at which the strong inversion condition sets in is as follows:[152]

$$W_{max} = \sqrt{\frac{2\,\varepsilon_s\,U_{inv}}{q\,N_D}} \tag{25}$$

where U_{inv} is the maximum electric potential drop across the depletion region,

$$U_{inv} = \frac{2\,k\,T}{q}\ln\left(\frac{N_D}{n_i}\right) \tag{26}$$

and n_i is the intrinsic carrier density in the semiconductor (1.45×10^{10} cm^{-3} for Si). Once the semiconductor lattice atoms begins to ionize, the contacting solution becomes the more polarizable of the two contacting phases and essentially all the contact potential beyond U_{inv} drops across the solution. Thus the band bending in the semiconductor for which the depletion region is responsible becomes fixed at essentially U_{inv}, which in turn depends only on well-known properties of the semiconductor itself. Use of the *n*-Si/CH_3OH–$Me_2Fc^{+/o}$ contact thus simplifies the otherwise formidable task of reliably measuring the electric potential drop across the semiconductor depletion region.

Though defined in terms of (Schottky) barrier heights (Φ_B), Tung's V_{bb} (here U_{bb}) and Δ parameters actually serve to describe the band bending manifest in the depletion region of the semiconductor. A direct link exists between barrier height and the band bending in the depletion region of a non-inverted Schottky contact, so that U_{bb} and Δ may be straightforwardly defined in terms of the barrier heights for the case he considered. At a strongly inverted contact, however, the band bending in the depletion region of the semiconductor is determined by U_{inv} and the applied potential, and is independent of Φ_B^o, provided the barrier height is larger than the critical barrier height Φ_B^* needed to induce strong inversion. Adaptation of Tung's model to describe the situation

for a strongly inverted high barrier height contact thus requires replacing his Φ_B^o with the surrogate quantity $\Phi_B^* \equiv V_{inv} + V_n$. (Figure 4d)

Ideal Schottky barriers exhibit diode quality factors very close to unity. However, the observed diode quality factors of our uniformly metallized *n*-Si/Ni contacts were generally significantly greater than 1.0. We have therefore chosen to employ the diode quality factor observed at the homogeneous metal contacts, A_M, as an approximation for A_{dot}. Possible reasons for the non-ideal diode quality factors observed are considered in Section VI.

Other factors worthy of consideration do not ultimately require modifications of the model. The concentrations of redox-active species and supporting electrolyte in our solutions are sufficiently high that the solution resistance is small, and the mass transport limit is high under the vigorous stirring employed during our measurements. This, coupled with our choice of the kinetically facile, outer-sphere, one-electron redox couple $Me_2Fc^{+/o}$, implies that the overpotential for electron transfer between the Ni particles and the solution is negligible up to the mass transport limit. The mass transport demands associated with the high current densities expected at the metal particles are offset by the efficiency of radial diffusion to these small, isolated contacts.[134, 135] Were this not the case, issues of lateral diffusion of electrons on the electrode surface[80, 135] and charging of the metal particles,[80, 111, 118] would clearly complicate any attempt to predict the behavior of the nanopatterned electrodes. In purely solid state systems the spreading resistance associated with the preferential flow of charge carriers through the portions of the semiconductor behind the low barrier height contacts can become important.[77] However, the mass transport limits imposed by the solution contacts employed herein ensure that current fluxes large enough to warrant correction for this effect are never reached.

The expression for the dark current expected at a nanopatterned electrode (SC/M|E contact) composed of interacting contacts, based on Tung's analytic model and the modifications and additions described above, is therefore

$$\begin{aligned} J_{nanopatterned} &= J_{dots} + J_{bare} \\ &= J_{o,\ dots}\left[1 - \exp\left(\frac{-q\ V_{app}}{A_{dots}\ k\ T}\right)\right] \\ &\quad + J_{o,\ bare}\left[1 - \exp\left(\frac{-q\ V_{app}}{A_{\ell}\ k\ T}\right)\right] \end{aligned} \tag{27}$$

where the contributing terms are defined in Table 1. With appropriate modification of the exchange current densities, $J_{o,\ dots}$ and $J_{o,\ bare}$, equation 27 can also be used to describe the current expected to flow through a SC/M|E contact if it is assumed that no interaction occurs between the two types of contacts.[21, 77] The definitions of the variables appropriate to this "independent contact" case are given in Table 2. Note that the pinch-off model does not reduce to the independent contact case for small Δ or large R_o, because the point-dipole approximation on which the analytic pinch-off model is predicated becomes increasingly unphysical.

III.3 Predicting the Photoresponse of SC/M|E Parallel Heterojunctions

Our experimental investigations also involved measuring the photoresponses of nanopatterned electrodes, so it is useful to extend the models described in the preceding section to predict the photoresponse properties of SC/M|E systems.[153, 154] The photogenerated current, J_{ph}, is assumed to be collected with 100% efficiency under short-circuit conditions, such that the current measured at short circuit under illumination, J_{sc}, serves as a reliable measure of the photogenerated current. Under open-circuit conditions, the photogenerated current must be dissipated entirely by the internal recombination mechanisms of the semiconductor device. Provided that the metal particles do not charge (a reasonable assumption at moderate biases given the effectiveness of radial diffusion and our use of a kinetically fast, outer-sphere, one-electron redox couple) the recombination

current is described by equation 27. Thus $J_{ph} = -J_{nanopatterned}$ at open circuit under illumination, where the electrode potential is $-V_{oc}$. The expected photoresponse relationship (V_{oc} vs J_{sc}) for the nanopatterned electrodes may therefore be determined using equation 27 if open-circuit voltages ($-V_{oc}$) are substituted for the corrected applied biases (V_{app}), and the dark current density ($J_{nanopatterned}$) is replaced with the short-circuit current density (J_{sc}):

$$\begin{aligned} J_{sc} &= J_{ph} \\ &= J_{o,\,dots}\left[\exp\left(\frac{q\,V_{oc}}{A_{dots}\,k\,T}\right) - 1\right] + J_{o,\,bare}\left[\exp\left(\frac{q\,V_{oc}}{A_{\ell}\,k\,T}\right) - 1\right] \end{aligned} \tag{28}$$

As with equation 27, the variable definitions appropriate to the interacting and independent contact cases are those in Tables 1 and 2, respectively.

IV. EXPERIMENTAL

IV.1 Preparation of Substrates

Single-crystal, (100)-oriented, P-doped, *n*-type Si wafers were obtained from Silicon Sense, Inc., of Nashua, NH. The wafers were 525 ± 18 μm thick, prime-grade samples cut from the same boule, and had resistivities of 5.7 ± 0.5 Ω·cm. Individual wafer resistivities were measured in the dark using a four-point probe (Alessi Model 541S, 250 μm radius Os-tipped probe, obtained from Cascade Microtech of Beaverton, OR) and were translated into dopant densities using a published empirical relationship.[155] Table 3 presents selected characteristics of these wafers.

The Si wafers were scribed on their back (unpolished) surface and then broken into small segments, approximately 1 cm × 2 cm. Before use, each segment was briefly but vigorously sonicated (40 kHz, 250 W "Genesis" system in full wave mode; Crest Ultrasonics, Trenton, NJ) in 18.0 MΩ·cm resistivity water obtained from a Barnstead Inc. Nanopure water purification system. Each piece was then degreased by rinsing sequentially in room temperature methanol; acetone; 1,1,1-trichloroethane; dichloromethane; 1,1,1-trichloroethane; acetone; and methanol. This process was followed by another brief, vigorous sonication in water. Each sample was subsequently immersed into gently agitated ammonium fluoride/hydrofluoric acid buffer [buffered HF] ($36\%_{wt}$ $NH_4F_{(aq)}$ / $7\%_{wt}$ $HF_{(aq)}$, pH 5.0, Transene Corp., Danvers, MA) until the surface became uniformly hydrophobic, which usually required ≈ 30 s. After rinsing with water and blowing the surface dry with a 100 psig stream of purified, filtered $N_{2(g)}$, each sample was etched for 4 min in a vigorously sonicated, warm (≈ 38°C) saturated aqueous solution of semiconductor-grade potassium hydroxide (Aldrich, Milwaukee, WI). The sample was removed from the basic etchant while still undergoing sonication, and immediately rinsed with water freshly drawn from the water purification system.[156] Finally, each silicon sample was blown dry with compressed $N_{2(g)}$ and immediately transferred to the apparatus used to prepare the two-dimensional nanosphere crystals.

IV.2 Methods For Nanopatterning And Deposition Of Metals

"Nanosphere" (also called "natural") lithography was used to prepare the metal dot patterns of interest.[138, 139] Polystyrene nanospheres of highly uniform diameters are commercially available over a wide range of sizes from a handful of specialty manufacturers. The dispersity of nanosphere radii varies not only from one manufacturer to another, but also from lot to lot. Because the vast majority of dislocations and low-angle grain boundary defects in a self-assembled nanosphere crystal can be traced to the presence of spheres having significant size dispersion, the nanospheres used were selected from the most uniform batches of commercially available particles (Table 8). These particles were supplied as aqueous sols of ionically stabilized polystyrene nanospheres. In some cases the concentration of surfactant (left over from the emulsion polymerization process) was appreciable in the materials supplied by the manufacturer. In these cases the as-supplied sols were centrifuged until the spheres settled out of solution, the supernatant liquid removed, and the spheres then re-suspended in pure water. This process was repeated until the sol would no longer foam appreciably under vigorous agitation.

To form the nanosphere lithographic masks, the etched, hydrophilic silicon samples were individually clamped into the apparatus shown in Figure 8 (DC motor servo-controlled dipping system from a "Minitrough" Langmuir-Blodgett system, KSV Instruments, Helsinki, Finland) and their lower portions immersed into a dilute (2.5 - 10.0 $\%_{wt}$) aqueous sol of polystyrene spheres of a chosen diameter. The samples were withdrawn from the sol at a constant rate (between 2 and 4 $\mu m\ s^{-1}$) in an environment of slowly flowing $N_{2(g)}$. The relative humidity of the ambient, and thus the rate of hydrodynamic flow into the growing crystal, was tightly controlled by adjusting the rate of $N_{2(g)}$ flow relative to the rate of evaporation of water from the sol. Typical crystal growth conditions are presented in Table 4. When the pulling process was complete, the self-assembled layers were characterized by optical microscopy (Stereozoom 4, 30x,

Bausch & Lomb, Rochester, NY; Scanjet 6100c Scanner, Hewlett Packard, Palo Alto, CA) and by TappingMode atomic force microscopy [TMAFM] (Multimode Nanoscope IIIa using TESP Probes, Digital Instruments, Santa Barbara, CA) and stored in a $N_{2(g)}$ environment (Figures 9a and 9b).

Each collection of samples having overlayers prepared using polystyrene spheres of a given diameter, D_s, was divided into three groups. The first group (nanopatterned, *n*-Si/Ni|E, or SC/M|E samples) consisted of those samples having the largest well-ordered polymer sphere bilayer crystals on their surfaces. The edges of the largest contiguous bilayer crystal(s) on these samples were marked off using a fine-tipped high-viscosity ink pen (nearly dry extra-fine point Sharpie permanent markers, Sanford North America, Bellwood, IL). The members of the second group (fully metallized, *n*-Si/Ni, or SC/M samples) were vigorously sonicated in water to remove the spheres, and an active area defined by masking off a macroscopic region with a permanent marker (fine point Sharpie, Sanford North America, Bellwood, IL). The third set of samples (bare samples, *n*-Si/E, or SC/E samples) were left undisturbed. None of the samples were re-etched at this point in the process.

All three groups of samples were transferred to a diffusion-pumped high-vacuum evaporation chamber (Vacuum Coating Unit Type LCI-14B, Consolidated Vacuum Corp., Rochester, NY) and the chamber evacuated to and maintained at a pressure of $\leq 3 \times 10^{-6}$ torr. Even the samples onto which no metal overlayer was deposited (bare samples) underwent this procedure, but such samples were kept in covered petri dishes to prevent their metallization. Between 14 and 53 nm of Ni (99.994%$_{wt}$, Alpha Aesar, Ward Hill, MA), as indicated by a quartz crystal oscillator thickness monitor (TM-100, R.D. Mathis, Long Beach, CA), was thermally evaporated onto the exposed substrates at a rate of ≤ 0.3 nm·s^{-1} from a tungsten filament (F2-3×.025 W filaments, R.D. Mathis, Long Beach, CA) positioned either 12 or 25 cm directly above the samples. The nanosphere mask was removed from the nanopatterned *n*-Si/Ni|E samples by gentle

sonication (Bransonic 1210R-MT, Branson Ultrasonics Corp., Danbury, CT) in water. Sonication in CH_3OH removed the ink mask from the fully metallized *n*-Si/Ni samples. The bare *n*-Si/E samples were sonicated vigorously in water to remove the nanospheres, leaving behind a bare silicon surface. None of the samples were re-etched at this point in the process. The collection of samples for a given sphere diameter thus consisted of one subset of silicon samples patterned with triangular Ni regions covering ≈ 8% of an otherwise bare surface (nanopatterned *n*-Si/Ni|E samples; see Figures 9c and 9d), another subset covered with a continuous Ni layer, and a third subset having completely bare surfaces. In each case, the silicon samples were carefully fractured into smaller pieces that incorporated only the useful portion(s) of each sample. All surfaces were stored in a $N_{2(g)}$ environment prior to use, and the time between substrate preparation and electrochemical characterization was kept to a minimum, in no case exceeding one week.

IV.3 Preparation of Electrodes

An ohmic back contact was formed on each sample by rubbing the liquid above a room-temperature In-rich mixture of In [99.999%$_{wt}$ (metals basis), Alfa Aesar, Ward Hill, MA] and Ga (99.99+%$_{wt}$, Aldrich), containing about 18%$_{at}$ In,[157] over the entire back surface of each silicon sample. The sample was then attached to a tinned copper wire (22 AWG, Belden, Richmond, IN) using conductive silver print (GC Electronics, Rockford, IL). The wire was encased in a glass rod and the back and edges of the resulting electrode were sealed with epoxy (Epoxy Patch Kit 1C, Dexter Corp., Seabrook, NH). The epoxy was extended to the edge of the properly nanopatterned regions on the nanopatterned electrodes and to the edge of the contiguous metal film on the completely metallized samples. The shape and area of the exposed portions of the bare electrodes was kept similar to that of the nanopatterned and completely metallized electrodes.

IV.4 Electrochemical Measurements

Electrochemical experiments were performed at room temperature under a $N_{2(g)}$ atmosphere, in freshly prepared solutions of 0.10 M 1,1'-dimethylferrocene [Me_2Fc^o], 0.015 M 1,1'-dimethylferrocenium tetrafluoroborate [$Me_2Fc^+BF_4^-$], and 1.0 M $LiClO_4$ in CH_3OH. Me_2Fc^o (Strem, Newburyport, MA) was purified by sublimation and $Me_2Fc^+BF_4^-$ was synthesized by chemical oxidation of Me_2Fc^o using procedures described previously.[101] $LiClO_4$ (J.T. Baker, Phillipsburg, NJ) was dried by melting the as-received material at 300°C under vacuum in an organic-free quartz tube,[158] and CH_3OH (Omnisolv grade; EM Science, Gibbstown, NJ) was dried over Mg turnings and distilled under $N_{2(g)}$. The solid reagents were stored and weighed out in a drybox (Vacuum Atmospheres Corp. M040-1, Hawthorne, CA). The electrolyte and redox compounds were maintained under $N_{2(g)}$ while they were loaded into the cell vessel and dissolved in the solvent.

All electrochemical measurements were performed under $N_{2(g)}$ using a three-electrode potentiostatic arrangement, with a silicon working electrode and a large platinum mesh counter electrode. A platinum wire submersed in the solution referenced the measured potentials to the bulk solution potential, which was periodically measured relative to SCE via a calibrated methanolic $||LiCl_{(sat'd)}|HgCl_{2(sat'd)}|Hg_{(\ell)}$ reference. Each time a new cell was prepared, the Pt counter and reference electrodes were cleaned by immersion in aqua regia [a 3:1 (v/v) solution of concentrated $HCl_{(aq)}$ (EM Science) and concentrated $HNO_{3(aq)}$ (EM Science)] for approximately 5 min. The working and counter electrodes were submerged ≈ 3 cm apart at opposite ends of a glass cell, with the reference ≈ 1 cm perpendicular to the midpoint between them. The working (semiconductor) electrode faced the wall of the electrochemical cell, such that it could be illuminated. A Princeton Applied Research Model 273 Digital Potentiostat-Galvanostat (EG&G PARC, Princeton, NJ) was used in its high-stability potentiostatic mode without

iR compensation. The cell resistance and mass-transport-limited current densities were determined from the current-voltage properties of an epoxy-masked platinum working electrode having one exposed face of approximately the same shape, size, and orientation as the silicon samples to be studied, swept at 100 mV s^{-1} well into the anodic and cathodic mass-transport limited current regimes.

Immediately before use, each of the silicon electrodes (even those having a continuous Ni film on their surface[159]) were immersed into mechanically agitated buffered HF for 30 s and then rinsed with water before being thoroughly dried with compressed $N_{2(g)}$. The samples were then transferred to the electrochemical cell and connected to the potentiostat, the transfer occurring under a $N_{2(g)}$ blanket to protect the cell solution from the laboratory atmosphere.

Illumination was provided with a 250 W tungsten-halogen projection lamp (General Electric SpectraStar ENH, dichroic rear reflector; Top Bulb Supply, East Chicago, IN) whose intensity was varied using neutral optical density filters (glass ND-70 filters, Hoya Optics, Fremont, CA). The infrared portion of the lamp output was filtered using a water filter with a 10 cm path length. Aluminum foil, coated on both sides with flat black paint, was used to produce a shroud around the cell, preventing stray light from reaching the electrodes. The entire experimental apparatus was housed in a lightproofed fumehood, making it possible to obtain reliable data at extremely low illumination intensities. The temperature of the cell was continuously monitored with a thermometer immersed in the solution, and care was taken to minimize heating of the cell. All photoresponse measurements were taken between 22.7°C and 29.3°C. It was possible to collect dark J-V measurements within a much tighter temperature range, as indicated in Table 9.

The current-voltage [I-V] characteristics of each electrode were measured in complete darkness and at three different light intensities. The potential of the silicon electrode began at the cell potential, was swept upward to +300 mV vs cell, swept down

to –600mV vs cell, and then returned to the cell potential. Under each illumination condition, two such sweeps were performed before the digitized data was collected. The sweep rate used was 40 $mV \cdot s^{-1}$. Once the I-V data were collected, the photoresponse of each electrode was also determined. Open-circuit voltage, V_{oc}, vs short-circuit current, I_{sc}, data were collected manually, through the potentiostat electronics but with the control loop disengaged for the V_{oc} measurements and set to maintain 0 V vs cell (the reference) for the short-circuit current measurements. This procedure was performed at each of ten exponentially spaced light intensities, selected by variation of the number of neutral density optical filters employed. All measurements were made in magnetically stirred solutions of electrolyte and redox couple.

IV.5 Data Analysis

Following electrochemical characterization, the exposed area of each electrode was determined from a digitized image of the electrode positioned next to a reference grid of known dimensions (Scanjet 4c and ImageSXM,[160] Steve Barrett, University of Liverpool, U.K.). The electrode areas were used to convert all measured currents into current densities, J.

The digitized dark J-V curves were corrected for resistance and concentration overpotential losses using the equation:

$$V_{app} = V_{nominal} - \eta_{conc} - IR_s \qquad (29)$$

The corrected applied potential ,V_{app}, is reduced in magnitude from the nominal value, $V_{nominal}$, by accounting for the concentration overpotential, η_{conc}, and for the potential drop across the cell, as given by the product of the total current, I, and the series resistance, R_s. For a given redox solution and electrode configuration, the limiting anodic current density, $J_{lim,\,a}$, and the limiting cathodic current density, $J_{lim,\,c}$, were determined first, from visual inspection of the J-V properties of the model platinum working electrode. These limiting current densities were then used to partially correct the

potential of the platinum electrode for concentration overpotential losses at each current density, using the following formula:

$$E_{\text{partly corrected}} = E_{\text{nominal}} - \eta_{\text{conc}} \tag{30}$$

where

$$\eta_{\text{conc}} = \left(\frac{R\,T}{n\,F}\right)\left[\ \ln\left(\frac{J_{\text{lim, a}}}{-\,J_{\text{lim, c}}}\right) - \ln\left(\frac{J_{\text{lim, a}} - J}{J - J_{\text{lim, c}}}\right)\ \right] \tag{31}$$

and where J is the current density at the electrode in question, R is the gas constant, *n* is the number of electrons transferred (one, in this case), and F is the Faraday constant.[161] The series resistance was then determined from the slope of the linear portion of the overpotential-corrected platinum J-V curve. Use of the resulting parameters in equation 29 allowed for the complete correction of the applied potentials at the silicon electrodes. Series resistances encountered in this work were typically on the order of 30 Ω and were due primarily to solution resistance. Typical limiting anodic and cathodic current densities were approximately 30 mA cm^{-2} and –4 mA cm^{-2}, respectively.

Once these corrections were applied to the dark J-V data, the sets of applied potentials for the different electrodes were no longer identical. To average results obtained from replicate electrodes, the J-V data were converted into a universal set of 5 mV applied potential increments, using the current density measured at the closest corrected applied potential. The raw, uncorrected data were taken at 2 mV potential increments, making the error introduced by this procedure minimal. All dark J-V data for a replicate set of electrodes were then averaged to obtain a geometric mean current density at each selected corrected potential. Fitting these data to the diode equation,[162]

$$J = J_o\left[1 - \exp\left(\frac{-q\,V_{\text{app}}}{A\,k\,T}\right)\right] \tag{32}$$

in which the exchange current J_o is defined as

$$J_o = A^{**}\,T^2\,\exp\left(\frac{-q\,\Phi_{\text{obs}}}{k\,T}\right) \tag{33}$$

and V_{app} is the corrected applied potential, allowed the extraction of the observed effective barrier heights, Φ_{obs} , and diode quality factors, A. The effective Richardson constant, A^{**},[162] used in this work was 120 $A \cdot cm^{-2} \cdot K^{-2}$.

The photoresponse measurements were taken at a small number of discrete light intensities, and thus could not be geometrically averaged at a consistent set of open-circuit voltages. At high light intensities it is likely that there was some uncompensated voltage drop across the solution under short-circuit conditions, but this could not be corrected for without assuming a form for the photoresponse. Thus the photoresponse results are presented as collected, but are restricted to current densities below the measured mass-transport limit for each system. The diode equation (equation 32) was modified to predict photoresponses by replacing J with J_{ph} and V_{app} with V_{oc}, as per the discussion leading up to equation 28.

IV.6 Nanopattern Characterization

Statistical data concerning the size distribution of the Ni particles on the nanopatterned *n*-Si samples was obtained from TMAFM images of such surfaces.[163] These images were analyzed using a computer program (ImageSXM,[160] Steve Barrett, University of Liverpool, U.K.) capable of automatically measuring the areas of particles defined as the collection of data pixels of a height greater than some minimum threshold value. Effective particle radii (R_o) were determined from the measured area of each triangular particle by calculating the radius of a circular region having the same total area. The actual area fraction of the nanopatterned electrodes covered by Ni (f_{actual}) was determined from the total area of the particles divided by the total image area, averaged over a series of high-quality images of the nanopatterned surfaces. Defects were included in these calculations, but an effort was made to avoid counting microscopic dust and debris on the images as particles.

Statistics on defects in the nanopatterns were also collected from TMAFM images. Defects were classified into three categories: point vacancies, dislocations, and grain boundaries, as shown in Figures 9c and 9d. The size of the largest particle associated with each observed point vacancy was determined in a manner analogous to that used to determine the size of the particles in general, except that the defect particles were separated into separate particles at points where they resembled an isthmus. The total length of dislocations and grain boundaries present within each TMAFM image was measured to obtain an estimate of the prevalence and potential impact of these defects. Dislocations were further characterized by measuring the distribution of particle sizes associated with such defects, employing the same method as that employed for the point vacancies. An upper limit on the number density of particles associated with dislocation-type defects was calculated by assuming that a larger-than-usual particle appears on either side of a dislocation, with the same spacing as that observed in the crystals. Thus the maximum number density of defect particles associated with dislocations is

$$\rho_{\text{dislocation particles}} = 2\left[\frac{\left(\frac{\text{total dislocation length}}{\text{total image area}}\right)}{\text{interparticle spacing}}\right] \left[=\right] \text{cm}^{-2} \qquad (34)$$

In practice, dislocation defects often only resulted in one defect particle per interparticle spacing length, so the value obtained from equation 34 serves as an upper bound on the number density of defect particles. Grain sizes in the lithographic masks were large enough that direct measurement by TMAFM was not practical. However, a lower limit was calculated from the measured grain boundary densities by assuming the grains to be squares of side length s. Since each grain boundary borders two grains, a total grain area of $2s^2$ is associated with every 4s of grain boundary, and the lower limit on grain size is

thus

$$\left(\frac{\text{total length of grain boundary}}{\text{total image area}}\right) = \left(\frac{2\,s^2}{4\,s}\right)$$
$$\Rightarrow \quad s = 2\left(\frac{\text{total length of grain boundary}}{\text{total image area}}\right) [=] \text{ cm} \tag{35}$$

The actual crystallites that formed the nanosphere lithographic masks had meandering edges and were thus appreciably larger than this lower limit.

The surfaces of a limited number of SC/M|E electrodes were analyzed with TMAFM subsequent to their electrochemical characterization, to verify that the Ni particles remained on the surface. This required removing the nanopatterned *n*-Si from the epoxy used to encapsulate the electrodes, which was accomplished by soaking the electrode for 72 h in N,N-dimethyl formamide (EM Science, Gibbstown, NJ) at 65°C, followed by several sequential 24 h baths in fresh N,N-dimethyl formamide spiked with traces of water at the same temperature but under intermittent vigorous sonication. Even after such processing the electrode surfaces were not clean enough that high-quality TMAFM images could be otained; however, it could be clearly seen that undamaged Ni nanopatterns were present on the electrode surfaces even after the electrochemically characterized *n*-Si/Ni|E substrates were removed from the electrodes.

V. RESULTS

V.1 Characteristics Of Natural Lithographic Masks And Of Nanopatterned Surfaces

Figures 9a and 9b are TMAFM images of nanosphere lithographic masks of the quality typically prepared in our work. Figures 9c and 9d show representative metal dot patterns produced using bilayer nanosphere crystals as lithographic masks for the thermal evaporation of Ni. TMAFM observations of SC/M|E electrode surfaces after their use in electrochemical experiments verified that the Ni nanopatterns were robust and survived the electrode preparation, etching, and electrochemical characterization processes.

Because our measurement methods required probing the electrical properties of macroscopic electrode areas, the typical quality of the nanopattern over the entire surface, not the optimum pattern quality obtained in selected locations and situations, is the critical parameter to consider in characterizing the nanopatterns. Table 5 summarizes the key properties observed for the masks and for the nanopatterned Ni films produced in this work. Typical non-defect particle cross-sections, as obtained by TMAFM, are shown in Figure 10, with the height cutoff used for particle sizing in each case also indicated. The distribution of measured particle sizes for each template nanosphere diameter is presented in Figure 11. These size distributions incorporate all particles, including those associated with defects.

Defects in the nanopatterns were classified into three distinct categories: point vacancies, dislocations, and grain boundaries; examples of each are illustrated in Figure 9. Table 5 includes data on the frequency with which each type of defect was observed in double-layer nanopatterns composed of spheres of each size employed in this study. Point vacancy defects were observed to appear preferentially in the upper layer of the nanosphere bilayer crystals, as evidenced in Figure 9c. Size distributions of the particles associated with point vacancy defects found in each type of mask appear in Figure 12.

Dislocations typically resulted in a slight shift in the crystal pattern, with no other change in registry (Figure 9c). Size distributions of the Ni particles found at dislocations appear in Figure 13. The observed grain boundaries were most often low-angle (Figure 9d), though large-angle grain boundaries were also occasionally observed. Both dislocations and low-angle grain boundaries were almost always found oriented parallel to the axis along which the substrates were pulled from the nanosphere-laden sol during the crystal growth process.

V.2 Current Density-Voltage Properties Of Electrodes In The Dark

Figure 14 summarizes the dark J-V behavior of the electrodes investigated in this work. These results are grouped by the diameter of the spheres (D_s) used in preparing the nanopatterned SC/M|E electrodes of each set. This grouping minimizes effects of variations in the wafer properties, metallizations, measurement temperatures, and other systematic variables over the extensive number of experiments and the long time period involved in this work. Levenberg-Marquardt fits to the diode equation (equation 32) for each type of electrode surface are shown in Figure 14, and the best fit parameters appear in Table 9. When the barrier height (Φ_{obs}) and diode quality factor (A) were both allowed to float, the diode equation fit all the observed responses remarkably well.

As shown in Figure 14d, the largest dots exhibited behavior in accord with the predictions of the independent contact model. Such behavior is that conventionally expected[44] for macroscopic parallel contacts on the same semiconductor surface. Specifically, the currents observed at a given potential for a surface patterned with 1530 nm diameter spheres were in excellent agreement with the values obtained by scaling the current density observed for a surface completely covered with Ni by the fractional area of Ni on the *n*-Si/Ni|E surface, as per equation 27 using the definitions in Table 2. A similar situation was observed for dots formed using the 760 nm diameter spheres (Figure 14c), although here the predictions of the interacting contact (pinch-off) model are

essentially identical to those of the independent contact model. Additionally, in both cases the forward bias current density observed for the metallized Si electrodes was much larger than the current density observed for a bare *n*-Si surface in contact with the CH_3OH–$Me_2Fc^{+/o}$ solution.

For the smaller dot sizes, current densities decreased with the size of the metal dots, even at essentially constant fractional area coverage of metal on the Si. For the smallest (D_s = 174 nm, R_o = 27.5 nm, Figure 14a) metal dot structures, the currents were within a factor of two of those observed for the bare *n*-Si electrodes, even though ≈ 8% of the surface was covered with Ni.

The predictions of the analytical SC/M|E interacting contact (pinch-off) model (equation 23 and Table 1), obtained using the measured parameters listed in Table 6 and no adjustable parameters, are shown for each set of nanopatterned electrodes, except for those with D_s = 1530 nm, for which the model does not apply because the pinch-off criterion (equation 5) is not satisfied. The predictions are in excellent agreement with experimental observations, and the data for the small dimension dot patterns differs significantly from what would be expected for a system that did not display the "pinch-off" phenomenon. The interacting contact predictions can be shifted upward or downward with essentially no change in curve shape by allowing either R_o or Φ_B^* to float; the values that provide the best least-squares fit of the interacting contact model to the experimental data are those given in Table 7. For comparison, Figure 14 also includes the predictions of the independent contact model (equation 23 and Table 2).

Over the course of preparing and characterizing many nanopatterned electrodes, it was found that a substantial number exhibited an unusually quick rise in current at small forward biases (Φ_{eff} on the order of those observed at *n*-Si/Ni contacts and unphysically large A values), only to return to "normal" behavior at large forward biases (Figure 15). This local inflection behavior was particularly common and pronounced on the electrodes patterned with the smallest spheres, i.e., those having metal features expected to be

almost completely pinched-off. This behavior was eventually associated with the disproportionate effect of a small number of large-area Ni defects on those electrodes, usually located at the edges of the electrodes where the epoxy did not completely cover the unpatterned regions of the substrates. Microscopic investigation of some of these electrodes allowed the large metal defects to be identified and covered with epoxy, and when this was done the local inflections in the J-V curves of the treated electrodes became far less pronounced. Because not all the nanopatterned electrodes exhibited this behavior, those that did exhibit it were eliminated from our analyses. It is possible that the local inflection is a result of the mass-transport flux limit being reached at the electrolyte/metal interface of unpinched-off, low-effective-barrier height defects, saturating the current they can contribute to the electrode under large forward biases. As the defects become mass-transport limited and unable to provide any more current, the behavior of such electrodes comes to more closely resemble that of an electrode lacking any large area defects and covered only with Ni particles of the intended (and numerically dominant) size.

V.3 Photoresponse of Nanopatterned Electrodes

Figure 16 shows the photoresponses, obtained by plotting J_{sc} vs V_{oc}, for each set of electrodes. The data are again grouped by the diameter of the spheres employed in the preparation of the nanopatterned electrodes of each set. This figure also contains the predicted photoresponses, based on the measured dark J-V properties and equation 28, overlaid onto the experimental photoresponse data.

A clear effect, correlated with the size of the metal dots, is apparent in the data. Even though the total coverage of metal was nearly identical for the various nanopatterned electrodes, those covered with metal dots having the smallest spatial dimensions exhibited the highest open-circuit voltages at a given short-circuit photocurrent density. The effect was significant in that at $J_{ph} \approx J_{sc} = 10$ mA cm^{-2}, V_{oc} increased from 250 mV to 400 mV as the effective radius of the Ni dots (R_o) decreased from 255 nm to 27.5 nm. At the

smallest Ni particle radii, the V_{oc} values were nearly equal to those of the unmetallized electrodes, indicating that recombination had been significantly suppressed even though ≈ 8% of the surface was still covered with metal.

Figure 16 also shows the predicted photoresponse properties based on measurements of the dark responses in conjunction with equation 28 and Table 1 or Table 2. For the Ni dots having R_o = 27.5 nm, V_{oc} was within ≈ 100 mV of the value obtained at a bare electrode, for which bulk recombination/diffusion has been shown to determine the current-voltage properties at sufficiently large forward bias voltages and/or illumination intensities.[101]

VI. DISCUSSION

VI.1 Growth of Nanosphere Masks

Initially observed by Perrin in 1909,[164] the self-assembly of uniform colloidal particles into regular arrays was developed as an extended-area lithographic technique by Deckman and Dunsmuir in 1982.[139] Our studies required the development of a method for preparing extended (many mm^2) crystalline structures of such spheres, close-packed in the plane parallel to the substrate surface and two sphere layers thick. Guided by the work of others interested in this technique,[138, 164, 165] we developed a process roughly analogous to Czochralski crystal growth which entails the slow extraction of a hydrophilic substrate from an aqueous sol of monodispersed-diameter nanospheres under a controlled-humidity ambient. Because the substrate and the ionically functionalized nanospheres are both very hydrophilic, sol is constantly drawn onto the non-submerged portion of the substrate, where the water evaporates and the nanospheres are left behind. Once a seed crystal forms on the substrate surface, the rate of evaporation from the water-logged crystal approaches steady state; thus the rate of sol flow into the non-submerged substrate region becomes constant, such that the crystal grows at a fixed rate and to a fixed thickness if the sample is extracted from the sol at a properly selected constant velocity. Growth conditions were optimized to obtain bilayer crystals. The resulting two-dimensional crystals that grew on the substrate surface consisted of two hexagonally close-packed layers, stacked on top of each other in an AB fashion (Figure 17).

Even though growth of bilayer crystals was more difficult than that of single-layer crystals, we employed bilayer crystals as our lithographic masks because of the sensitivity of the measured current density at *n*-Si/Ni|E electrodes to even a relatively small number of large-area metal defects. As shown in Figure 17, a point vacancy defect in a single-layer nanosphere mask leads to the formation of a metal patch equal in size to

the spheres used in the mask itself. In contrast, a similar defect in one layer of a bilayer mask leads to a much smaller metal defect. If single layer masks were used, a point vacancy defect at one lattice point in one thousand would be problematic in testing the pinch-off theory. A much higher defect rate is acceptable with double layer masks, provided that the defects in the two layers are not correlated. We have found experientially that the latter condition is satisfied. Bilayer masks also have the advantage of providing a nanopattern with relatively large spaces between the Ni dots, making it possible to treat the dots independently and thus allowing application of Tung's analytic model to the resulting nanostructured SC/M|E interfaces.

For the crystal growth system and conditions employed in this work, a definite correlation was observed between the size of the nanospheres employed and the difficulty encountered in growing highly ordered, low defect density bilayers. High quality bilayers were most readily obtained with spheres on the order of 400 nm in diameter, with the reliable generation of bilayer crystals becoming progressively more difficult as the spheres became larger or smaller. Repeated attempts to create ordered bilayers of 2500 nm diameter spheres were unsuccessful. We believe this size effect to be related to the natural thickness of the water layer that forms on the silicon substrate as it is pulled out of the sol.[164, 165] The use of different solvents and/or surface treatments may modify the optimal particle diameter and workable particle size range.

VI.2 Properties of Nanosphere Masks

TMAFM provided verification of the quality of the nanopatterns actually produced and of their integrity in the wake of electrode preparation, chemical etching, and electrochemical characterization. The atomic force probe had a tendency to pick up debris from the nanopatterned surface and thereby rapidly deteriorate the quality of the images obtained. TMAFM proved far more reliable in imaging the close-packed sphere layers prior to their use as a lithographic mask, and it was at this point that the most

complete and rigorous checks of nanosphere ordering were performed. TMAFM images akin to those of Figures 9a and 9b were routinely collected in order to assess the packing quality of the nanosphere bilayers before they were used in subsequent steps.

Despite the challenge of keeping the probe clean, TMAFM was also used to investigate the nanopatterned Ni deposits produced using the nanosphere lithographic masks. High-quality nanopatterns were produced from aqueous sols over macroscopic areas on *n*-Si surfaces without the use of surfactants or the creation of a thick oxide layer. When Ni was used as the deposited metal, the nanoscopic metal dots adhered to the surface and reliably withstood the rigors of electrode preparation and characterization.

The Ni particles constituting the double-layer nanopatterns prepared in our work were appreciably larger and more triangular than idealized geometric considerations would lead one to expect (cf. Figure 9 and Figure 17d).[138] This behavior might be ascribed to scattering of thermally evaporated Ni atoms off the sides of the nanospheres constituting the upper layer of the mask. It is clear from the particle cross-sections (Figure 10) that the Ni particles do not exhibit mesa-like structures at even the largest sphere diameters. (The largest defects observed at each particle size, on the other hand, did exhibit mesa-like cross-sections.) This behavior made obtaining meaningful estimates of the particle sizes challenging. The choice of the minimum threshold used in the sizing algorithm was to a certain extent necessarily subjective, as the particle cross-sections were essentially triangular and their edges not perfectly distinct. Although it is clear that the cutoffs used were consistently above the actual base of the particles, this was necessitated by the noise in some of the images, as is, for example, particularly visible in Figure 10b. An effort was made to keep the relative height cutoff consistent from image to image and from one nanosphere diameter to another; the net result is a reasonable precision in the measurements at the cost of a moderate (20% - 40%) systematic underestimation of the effective dot radii. The consistency in particle shape and cross-section observed across the range of particle sizes suggests that tip convolution effects were not substantial in

these images. Nonetheless, a slight overestimation is incorporated into the tabulated particle sizes as a result of not employing a tip convolution correction,[166] which offsets to some extent the underestimation associated with the height cutoff method used in sizing the particles.

While dislocations and grain boundaries were observed to occur in both the upper and lower layers of the nanosphere bilayer crystals, point vacancies were almost exclusive to the upper of the two layers. Because the nanospheres are thought to actually roll along the smooth substrate surface[164] in forming the lower layer, but must roll over the corrugated lower layer in forming the upper layer, this result is not surprising. The increase in point vacancy density with increasing sphere size (Table 5, appreciably more pronounced when considered on a per-lattice-point basis) is readily understood within the same framework.

Table 7 includes an indication of the fractional area of each nanopatterned surface statistically expected to be covered by particles having effective radii in excess of $2R_o$, formed as a result of point vacancy and dislocation defects. (Grain boundaries were not the dominant cause of large-area defects for any value of D_s.) These values are based on the measured defect densities in Table 7 and the observed particle size distributions shown in Figures 12 and 13. In no case does the defect area fraction exceed 1% of the total surface area; moreover, the fraction remains nearly constant for the three smallest values of D_s. While the defect density for the D_s=1530 nm spheres does approach 1%, it is for these largest spheres that large-area defects are not expected to behave any differently than the "normal" nanopattern particles, and where the electrode behavior is expected to depend solely on the fraction of the surface covered with Ni (f_{actual}).

VI.3 Dark Electrical Properties vs Size of Metal Dots

Qualitatively, our electrical characterizations indicate that the pinch-off effect can be clearly observed in the dark J-V behavior of nanopatterned *n*-Si/Ni|E parallel junctions

employing a kinetically rapid, high barrier height electroactive species in solution. The observation of this effect in the dark at small forward biases suggests that it is electrostatic in origin, and not the result of hydrogen evolution,[84, 115] the formation of an oxide layer,[102, 114] or metal particle charging associated with slow electron transfer out of the metal under illumination conditions,[111, 118, 126] as has in some cases been suggested in the photoelectrochemical literature.

Quantitative evaluation of the results described herein indicates that Tung's analytic model,[21, 22] formulated to describe transport across pinched-off inhomogeneous SC/M contacts, is also amenable to the description of SC/M|E contacts operating in the pinch-off regime. The results described above indicate that the modified model of equation 27 and Table 1 provides excellent agreement with experimental results for the *n*-Si/Ni|E system investigated here, in which the *n*-Si/E interface is known to induce strong inversion in the semiconductor and involves a fast, outer-sphere, one electron redox couple.[144]

The calculations made in this work implicitly assume that *n*-Si/Ni contacts are homogeneous: an assumption of questionable validity in light of BEEM observations made in the solid-state literature.[61] Nonetheless, we can assert – with some confidence, given the observed behavior of the *n*-Si/Ni|E electrodes patterned with the largest spheres – that at least a portion of the microscopic *n*-Si/Ni contacts formed in this work have extremely low barrier heights that would dominate the behavior of a dot-covered electrode if not for the pinch-off effect. We have also assumed the Si substrates of our *n*-Si/Ni|E electrodes to be planar. The required etch of the nanopatterned samples prior to their electrochemical characterization necessarily removes a surface layer of oxidized silicon (associated with the nanosphere crystal growth process) from the bare regions while leaving it in place under the Ni. To the extent that the silicon surface is somewhat raised underneath the metal particles and lowered on the bare regions of the nanopatterned electrodes, this would tend to enhance the pinch-off effect.[34] In contrast, to the extent

that the effective *n*-Si/Ni interface moves below the plane of the *n*-Si/E interface as a result of silicide formation,[167] the opposite consequence would be expected. Numeric simulations[34] indicate that non-planarities can have an appreciable effect on pinch-off even when they are much smaller than the depletion width.

The theory described herein is also built around the assumption of a round low barrier height patch. Our patches clearly had a triangular shape, but as Tung[22] points out, the point-dipole approximation is equally applicable to small patches of any shape. The technique described herein of using an equivalent radius for the triangles is appropriate because the triangles are reduced to the same point dipole as a would be produced by a truly circular patch. In other words, the electrical predictions of the point-dipole analytic theory employed herein would remain unchanged if the model were re-developed explicitly for equilateral triangles, because such a theory would reduce the Ni patches to point dipoles of the same total moment as those utilized in the present work.

The mass-transport current limit imposed by the use of a solution contact hampered our ability to extract reliable diode quality factor (A_M) [and to a lesser extent effective barrier height (Φ_M)] values for the low barrier height *n*-Si/Ni electrodes, because only a few decades of J-V data could be obtained before the solution's mass transport limit was reached. However, the diode quality factors for all the samples investigated in this work clearly tended to be larger than 1, and in fact very close to 2, for most of the samples studied. One possible explanation for this is the presence of an interfacial oxide layer between the silicon and the contacting Ni phase. The presence of such an oxide layer would lead to an apparent diode quality factor that varies with potential and can adopt any value greater than one, depending strongly on the oxide layer thickness.[168]

A substantial effort was made to ensure that the Ni contacts on the nanopatterned *n*-Si/Ni|E electrodes were identical to those on the completely metallized *n*-Si/Ni samples used as a benchmark, save for their physical extent. Similarly, the bare regions on the *n*-Si/Ni|E electrodes were made as similar as possible to those on the completely bare

n-Si/E reference electrodes studied for each value of D_s. Insofar as possible, the electrodes of each group went through the same processing steps, on the same substrate, at the same time. It would have been easier to prepare the largest scale nanopatterns using conventional photolithography, as the nanosphere crystallization technique employed is at the limit of its capability there, but we wanted to keep the method similar as possible for all the electrodes. The *n*-Si/Ni samples of the dark D_s = 760 nm series exhibited unusually high barrier heights, which is reflected in the *n*-Si/Ni|E results as well. However, the same trend was observed for all the measurements performed using wafer Si-E4 (including those of the D_s = 174 nm series), suggesting this behavior was a direct result of some abnormality of that particular wafer.

It is possible that in some cases the deposition was hotter and the silicide growth progressed further from the initially formed Ni-rich silicide phase (Ni_2Si) toward a silicide richer in Si having a different barrier height. The wide range of barrier heights observed at any given Ni silicide[61, 140, 168] makes it difficult to assess what phases might be involved. While uniform heat treatment of the samples would have reduced uncertainty about what silicide phase(s) were present, doing so would also have made accurate assessment of the physical extent of the silicide regions on the required nanometer scale nearly impossible.[167]

The analytic interacting contact model of equation 27 and Table 1 fits the data extremely well in the regime where it is applicable. However, as shown in Table 7 and Figure 18, the point dipole model becomes increasingly imprecise in predicting the saddle point potential (Φ_{eff}) as the extent of pinch off diminishes. Thus use of the point dipole model must be restricted to the pinch-off regime, i.e., to those situations that satisfy equation 6. For situations where equation 6 is not satisfied, the independent contact model of equation 27 and Table 2 applies.

VI.4 Photoresponse Properties vs Size of Metal Dots

While the results of our photoresponse measurements are not as amenable to quantitative analysis as the dark J-V data, they provide important verification of the portability of the electrostatic idea of pinch-off to the dynamic realm of photoelectrochemistry. Our results are consistent with a qualitative model proposed by Nakato and Tsubomura[120, 127] to describe the behavior of SC/M|E electrodes. The appreciable agreement between the predictions of the interacting contact model (based on the dark J-V data) and our photoresponse results suggests that the photoresponse of SC/M|E electrodes can be predicted using the analytic interacting contact (pinch-off) model.

The use of nanopatterned contacts seems promising for the investigation of mixed barrier height phenomena in both solid-state and semiconductor/liquid systems. With regard to SC/E contacts, we note that exploitation of the pinch-off effect is especially attractive because it provides a mechanism to introduce catalytically active metal sites on the semiconductor surface – thus promoting desirable minority carrier-based multi-electron transfer reactions – without suffering deleterious majority-carrier-based recombination.[127, 135] Furthermore, these results suggest that with proper tuning of the redox potential of the electrolyte solution, appreciable concentrations of (non-aggregated) nanoscopic particles of a catalyst material can be placed on (moderately doped) semiconductor surfaces (even materials which normally form ohmic contacts) without promoting thermionic emission to a position of dominance over the total recombination current. These conditions simultaneously satisfy the conditions expected to make such catalyst particles optically transparent,[2, 3] suggesting a possible strategy for the preparation of highly efficient SC/M|E electrodes capable of converting light energy into chemical fuels, possibly even those requiring multi-electron electrochemical reactions, such as the splitting of H_2O[98, 169] and the reduction of CO_2.[81-83] Utilizing the principle

that majority carriers can be effectively shielded from nanoscopic low barrier height regions by the pinch-off induced by surrounding high barrier height SC/E contacts, it seems feasible to produce desirable, novel behavior in photoelectrodes through exploitation of this phenomenon.[170]

VII. CONCLUSIONS

Bilayer masks formed from sols of monodisperse diameter latex spheres allowed the fabrication of regular, well-defined nanometer-scale patterns of thermally evaporated Ni on *n*-Si electrode surfaces. The self-similar nanopatterns were prepared using spheres of four different sizes: in each case the area fraction of the *n*-Si surface covered with Ni was essentially 8%, but the size and spacing of the metal dots scaled with the diameter of the spheres employed in the lithographic process. The dark J-V and photoresponse properties of such intentionally prepared inhomogeneous contacts immersed in electrochemical solutions capable of inducing strong inversion in the semiconductor were found to exhibit a strong dependence on the size of the low barrier height metal particles, with Ni particles of effective radius between 25 and 100 nm behaving in quantitative accord with the predictions of an analytic theory describing the electrostatic pinch-off phenomenon developed by Tung and modified herein to describe strongly inverted SC/M|E contacts. The behaviors of *n*-Si/Ni|E electrodes incorporating the largest Ni particles were found to fall outside the pinch-off regime and were thus well-described as the net effect of many independent *n*-Si/Ni and *n*-Si/E devices operating in parallel. We believe this work provides the strongest and most direct support to date for the quantitative validity of Tung's 1991 analytic "pinch-off" model, demonstrates its utility in predicting the behavior of SC/M|E electrodes in both the dark and under illumination, and vindicates a theoretical view of SC/M|E interfaces first clearly proposed by Nakato and Tsubomura in 1985.[120, 127, 128]

Nanostructured metal deposits offer a potentially attractive approach to obtaining novel photoelectrochemical device properties while minimizing the deleterious effects of metal-induced charge carrier recombination at SC/M|E surfaces. Our results provide a rigorous and quantitative framework for continued work in this area.

VIII. REFERENCES

[1] History offers little in the way of encouraging precedent regarding the hope that humanity might act collectively in response to an impending disaster in which no individual actor can be blamed. Immediate economics drives human decisions, and we have not yet found an effective means to pro-rate future economic consequences into present cost structures on the global scale that would be required to address this apparent problem.

[2] A. Heller, D. E. Aspnes, J. D. Porter, T. T. Sheng, and R. G. Vadimsky, *J. Phys. Chem.*, **89,** 4444 (1985).

[3] A. Heller, *Pure Appl. Chem.*, **58,** 1189 (1986).

[4] A. Kumar, W. C. A. Wilisch, and N. S. Lewis, *Crit. Rev. Solid State Mater. Sci.*, **18,** 327 (1993).

[5] M. S. Tyagi, *Physics of Schottky Barrier Junctions*, in Metal-Semiconductor Schottky Barrier Junctions and Their Applications; B. L. Sharma, Ed., Plenum: New York (1984), pp. 1-61.

[6] E. H. Rhoderick and R. H. Williams, Metal-Semiconductor Contacts, 2nd ed., Oxford University Press: New York (1988).

[7] H. J. Lewerenz, *J. Electroanal. Chem.*, **356,** 121 (1993).

[8] W. Schottky, *Naturwissenschaften*, **26,** 843 (1938).

[9] N. F. Mott, *Proc. Cambr. Phil. Soc.*, **34,** 568 (1938).

[10] H. Gerischer, *Semiconductor Electrochemistry*, in Physical Chemistry: An Advanced Treatise; H. Eyring, D. Henderson, and W. Yost, Ed., Academic Press: New York (1970), Vol. 9A, pp. 463-542.

[11] S. Kurtin, T. C. McGill, and C. A. Mead, *Phys. Rev. Lett.*, **22,** 1433 (1969).

[12] A. Zur, T. C. McGill, and M. A. Nicolet, *J. Appl. Phys.*, **57,** 600 (1985).

[13] A. Kumar, M. D. Rosenblum, D. L. Gilmore, B. J. Tufts, M. L. Rosenbluth, and N. S. Lewis, *Appl. Phys. Lett.*, **56,** 1919 (1990).

[14] N. S. Lewis, *Acc. Chem. Res.*, **23,** 176 (1990).

[15] A. J. Bard, A. B. Bocarsly, F. R. F. Fan, E. G. Walton, and M. S. Wrighton, *J. Am. Chem. Soc.*, **102,** 3671 (1980).

[16] H. Gerischer, *J. Electroanal. Chem.*, **58,** 263 (1975).

[17] S. M. Sze, The Physics of Semiconductor Devices, 2nd ed., Wiley: New York (1981), Section 5.4.1.

[18] R. A. Marcus, *Angew. Chem., Int. Ed. Engl.*, **32,** 1111 (1993).

[19] R. Memming, *Ber. Bunsen-Ges. Phys. Chem.*, **91,** 353 (1987).

[20] N. S. Lewis, *Annu. Rev. Phys. Chem.*, **42,** 543 (1991).

[21] R. T. Tung, *Phys. Rev. B: Condens. Matter*, **45,** 13509 (1992).

[22] R. T. Tung, *Appl. Phys. Lett.*, **58,** 2821 (1991).

[23] R. D. Thompson and K. N. Tu, *J. Appl. Phys.*, **53,** 4285 (1982).

[24] L. Zheng, R. P. Joshi, and C. Fazi, *J. Appl. Phys.*, **85,** 3701 (1999).

[25] J. Osvald, *Solid State Electron.*, **35,** 1629 (1992).

[26] G. D. Mahan, *J. Appl. Phys.*, **55,** 980 (1984).

[27] T. Okumura and K. N. Tu, *J. Appl. Phys.*, **54,** 922 (1983).

[28] J. H. Werner and H. H. Guttler, *J. Appl. Phys.*, **69,** 1522 (1991), and references therein.

[29] Z. J. Horvath, *Vacuum*, **46,** 963 (1995).

[30] R. F. Schmitsdorf, T. U. Kampen, and W. Monch, *J. Vac. Sci. Technol., B*, **15,** 1221 (1997).

[31] S. Chand and J. Kumar, *J. Appl. Phys.*, **80,** 288 (1996).

[32] S. Chand and J. Kumar, *Semicond. Sci. Technol.*, **12,** 899 (1997).

[33] J. L. Freeouf, T. N. Jackson, S. E. Laux, and J. M. Woodall, *J. Vac. Sci. Technol.*, **21,** 570 (1982).

[34] J. P. Sullivan, R. T. Tung, M. R. Pinto, and W. R. Graham, *J. Appl. Phys.*, **70,** 7403 (1991).

[35] I. Ohdomari and H. Aochi, *Phys. Rev. B: Condens. Matter*, **35,** 682 (1987).

[36] S. Chand and J. Kumar, *J. Appl. Phys.*, **82,** 5005 (1997).

[37] J. Osvald and E. Burian, *Solid State Electron.*, **42,** 191 (1998).

[38] E. Dobrocka and J. Osvald, *Appl. Phys. Lett.*, **65,** 575 (1994).

[39] J. Osvald and E. Dobrocka, *Semicond. Sci. Technol.*, **11,** 1198 (1996).

[40] J. Osvald, *J. Appl. Phys.*, **85,** 1935 (1999).

[41] J. Osvald, *J. Appl. Phys.*, **88,** 7368 (2000).

[42] R. T. Tung, *J. Appl. Phys.*, **88,** 7366 (2000).

[43] S. Anand, S. B. Carlsson, K. Deppert, L. Montelius, and L. Samuelson, *J. Vac. Sci. Technol., B*, **14,** 2794 (1996).

[44] I. Ohdomari and K. N. Tu, *J. Appl. Phys.*, **51,** 3735 (1980).

[45] M. V. Schneider, A. Y. Cho, E. Kollberg, and H. Zirath, *Appl. Phys. Lett.*, **43,** 558 (1983).

[46] I. Ohdomari, T. S. Kuan, and K. N. Tu, *J. Appl. Phys.*, **50,** 7020 (1979).

[47] S. Hasegawa and S. Ino, *Int. J. Mod. Phys. B*, **7,** 3817 (1993).

[48] S. Chand and J. Kumar, *Semicond. Sci. Technol.*, **11,** 1203 (1996).

[49] S. Chang, A. Raisanen, L. J. Brillson, J. L. Shaw, P. D. Kirchner, G. D. Pettit, and J. M. Woodall, *J. Vac. Sci. Technol., B*, **10,** 1932 (1992).

[50] R. S. Wardlaw and I. M. Dharmadasa, *Int. J. Electronics*, **81,** 59 (1996).

[51] A. Tanabe, K. Konuma, N. Teranishi, S. Tohyama, and K. Masubuchi, *J. Appl. Phys.*, **69,** 850 (1991).

[52] S. Chand and J. Kumar, *Appl. Phys. A*, **63,** 171 (1996).

[53] C. Ballif, M. Regula, F. Levy, F. Burmeister, C. Schafle, T. Matthes, P. Leiderer, P. Niedermann, et al., *J. Vac. Sci. Technol., A*, **16,** 1239 (1998).

[54] D. Defives, O. Noblanc, C. Dua, C. Brylinski, M. Barthula, and F. Meyer, *Mater. Sci. Eng., B*, **61-2,** 395 (1999).

[55] T. Clausen and O. Leistiko, *Appl. Surf. Sci.*, **123,** 567 (1998).

[56] C. Coluzza, G. Di Claudio, S. Davy, M. Spajer, D. Courjon, A. Cricenti, R. Generosi, G. Faini, et al., *J. Microsc.*, **194,** 401 (1999).

[57] M. Zacchigna, H. Berger, L. Sirigu, G. Margaritondo, G. F. Lorusso, H. Solak, and F. Cerrina, *J. Electron Spectrosc. Relat. Phenom.*, **103,** 671 (1999).

[58] R. T. Tung, A. Levi, J. P. Sullivan, and F. Schrey, *Phys. Rev. Lett.*, **66,** 72 (1991).

[59] H. H. Weitering, J. P. Sullivan, R. J. Carolissen, R. Perez-Sandoz, W. R. Graham, and R. T. Tung, *J. Appl. Phys.*, **79,** 7820 (1996).

[60] P. Niedermann, L. Quattropani, K. Solt, A. D. Kent, and O. Fischer, *J. Vac. Sci. Technol., B*, **10,** 580 (1992).

[61] Y. Hasegawa, Y. Kuk, R. T. Tung, P. J. Silverman, and T. Sakurai, *J. Vac. Sci. Technol., B*, **9,** 578 (1991).

[62] A. A. Talin, R. S. Williams, B. A. Morgan, K. M. Ring, and K. L. Kavanagh, *Phys. Rev. B: Condens. Matter*, **49,** 16474 (1994).

[63] A. A. Talin, R. S. Williams, B. A. Morgan, K. M. Ring, and K. L. Kavanagh, *J. Vac. Sci. Technol., B*, **12,** 2634 (1994).

[64] H. Palm, M. Arbes, and M. Schulz, *Phys. Rev. Lett.*, **71,** 2224 (1993).

[65] W. J. Kaiser and L. D. Bell, *Phys. Rev. Lett.*, **60,** 1406 (1988).

[66] A. Olbrich, J. Vancea, F. Kreupl, and H. Hoffmann, *J. Appl. Phys.*, **83,** 358 (1998).

[67] B. A. Morgan, K. M. Ring, K. L. Kavanagh, A. A. Talin, R. S. Williams, T. Yasuda, T. Yasui, and Y. Segawa, *J. Vac. Sci. Technol., B*, **14,** 1238 (1996).

[68] B. A. Morgan, A. A. Talin, W. G. Bi, K. L. Kavanagh, R. S. Williams, C. W. Tu, T. Yasuda, T. Yasui, et al., *Mater. Chem. Phys.*, **46,** 224 (1996).

[69] R. T. Tung, J. P. Sullivan, and F. Schrey, *Mater. Sci. Eng., B*, **14,** 266 (1992).

[70] R. T. Tung, *J. Vac. Sci. Technol., B*, **11,** 1546 (1993).

[71] E. H. Rhoderick and R. H. Williams, Metal-Semiconductor Contacts, 2nd ed., Oxford University Press: New York (1988), p. 139.

[72] M. S. Tyagi, *Physics of Schottky Barrier Junctions*, in Metal-Semiconductor Schottky Barrier Junctions and Their Applications; B. L. Sharma, Ed., Plenum: New York (1984), pp. 48–50.

[73] E. H. Rhoderick and R. H. Williams, Metal-Semiconductor Contacts, 2nd ed., Oxford University Press: New York (1988), pp. 51, 54, 69, and 72.

[74] O. S. Anilturk and R. Turan, *Semicond. Sci. Technol.*, **14,** 1060 (1999).

[75] O. S. Anilturk and R. Turan, *Solid State Electron.*, **44,** 41 (2000).

[76] S. Hardikar, M. K. Hudait, P. Modak, S. B. Krupanidhi, and N. Padha, *Appl. Phys. A*, **68,** 49 (1999).

[77] P. Lahnor, K. Seiter, M. Schulz, and W. Dorsch, *Appl. Phys. A*, **61,** 369 (1995).

[78] A. Olbrich, J. Vancea, F. Kreupl, and H. Hoffmann, *Appl. Phys. Lett.*, **70,** 2559 (1997).

[79] T. Sakata, T. Kawai, and K. Hashimoto, *Chem. Phys. Lett.*, **88,** 50 (1982).

[80] Y. Nosaka, K. Norimatsu, and H. Miyama, *Chem. Phys. Lett.*, **106,** 128 (1984).

[81] R. Hinogami, T. Mori, S. J. Yae, and Y. Nakato, *Chem. Lett.*, 1725 (1994).

[82] R. Hinogami, Y. Nakamura, S. Yae, and Y. Nakato, *J. Phys. Chem. B*, **102,** 974 (1998).

[83] R. Hinogami, Y. Nakamura, S. Yae, and Y. Nakato, *Appl. Surf. Sci.*, **121,** 301 (1997).

[84] A. Heller, E. Aharon-Shalom, W. A. Bonner, and B. Miller, *J. Am. Chem. Soc.*, **104,** 6942 (1982).

[85] A. Heller, H. J. Leamy, B. Miller, and W. D. Johnson, Jr., *J. Phys. Chem.*, **87,** 3239 (1983).

[86] A. Heller and R. G. Vadimsky, *Phys. Rev. Lett.*, **46,** 1153 (1981).

[87] G. Oskam, D. Vanmaekelbergh, and J. J. Kelly, *Electrochim. Acta*, **38,** 291 (1993).

[88] C. C. Chen, C. S. C. Bose, and K. Rajeshwar, *J. Electroanal. Chem.*, **350,** 161 (1993).

[89] C. S. C. Bose and K. Rajeshwar, *J. Electroanal. Chem.*, **333,** 235 (1992).

[90] G. Oskam, L. Bart, D. Vanmaekelbergh, and J. J. Kelly, *J. Appl. Phys.*, **74,** 3238 (1993).

[91] P. Allongue, E. Souteyrand, and L. Allemand, *J. Electroanal. Chem.*, **362,** 89 (1993).

[92] A. Bansal, M. X. Tan, B. J. Tufts, and N. S. Lewis, *J. Phys. Chem.*, **97,** 7309 (1993).

[93] P. Allongue and E. Souteyrand, *J. Electroanal. Chem.*, **269,** 361 (1989).

[94] P. Allongue, E. Souteyrand, and L. Allemand, *J. Electrochem. Soc.*, **136,** 1027 (1989).

[95] M. Szklarczyk and J. O. M. Bockris, *J. Phys. Chem.*, **88,** 5241 (1984).

[96] A. Heller, *J. Phys. Chem.*, **89,** 2962 (1985).

[97] M. Szklarczyk and J. O. M. Bockris, *J. Phys. Chem.*, **88,** 1808 (1984).

[98] A. Heller, *Science*, **223,** 1141 (1984).

[99] T. Sakata, K. Hashimoto, and T. Kawai, *J. Phys. Chem.*, **88,** 5214 (1984).

[100] J. S. Curran, J. Domenech, N. Jaffrezic-Renault, and R. Philippe, *J. Phys. Chem.*, **89,** 957 (1985).

[101] A. Kumar and N. S. Lewis, *J. Phys. Chem.*, **95,** 7021 (1991).

[102] Y. Nakato, K. Abe, and H. Tsubomura, *Ber. Bunsen-Ges. Phys. Chem.*, **80,** 1002 (1976).

[103] W. E. Pinson, *Nature*, **269,** 316 (1977).

[104] R. H. Wilson, L. A. Harris, and M. E. Gerstner, *J. Electrochem. Soc.*, **124,** 1233 (1977).

[105] R. H. Wilson, L. A. Harris, and M. E. Gerstner, *J. Electrochem. Soc.*, **124,** 1511 (1977).

[106] K. W. Frese, Jr., M. J. Madou, and S. R. Morrison, *J. Electrochem. Soc.*, **128,** 1939 (1981).

[107] S. Menezes, A. Heller, and B. Miller, *J. Electrochem. Soc.*, **127,** 1268 (1980).

[108] B. Miller, S. Menezes, and A. Heller, *J. Electrochem. Soc.*, **126,** 1483 (1979).

[109] W. Kautek, J. Gorbrecht, and H. Gerischer, *Ber. Bunsen-Ges. Phys. Chem.*, **84,** 1034 (1980).

[110] R. N. Dominey, N. S. Lewis, J. A. Bruce, D. C. Bookbinder, and M. S. Wrighton, *J. Am. Chem. Soc.*, **104,** 467 (1982).

[111] Y. Nakato, M. Shioji, and H. Tsubomura, *Chem. Phys. Lett.*, **90,** 453 (1982).

[112] M. Szklarczyk and J. O. M. Bockris, *J. Phys. Chem.*, **88,** 5241 (1984).

[113] See, for example, A. Heller, E. Aharon-Shalom, W. A. Bonner, and B. Miller, *J. Am. Chem. Soc.*, **104,** 6942 (1982), and references 1-26 therein.

[114] Y. Nakato and H. Tsubomura, *Isr. J. Chem.*, **22,** 180 (1982).

[115] A. Heller, *Hydrogen-Generating Solar Cells Based on Platinum-Group Metal Activated Photocathodes*, in Energy Resources Through Photochemistry and Catalysis; M. Grätzel, Ed., Academic: New York (1983), pp. 385-420.

[116] D. E. Aspnes and A. Heller, *J. Phys. Chem.*, **87,** 4919 (1983).

[117] D. E. Aspnes and A. Heller, *J. Vac. Sci. Technol., B*, **1,** 602 (1983).

[118] Y. Nakato and H. Tsubomura, *J. Photochem.*, **29,** 257 (1985).

[119] H. Tsubomura and Y. Nakato, *New J. Chem.*, **11,** 167 (1987).

[120] Y. Nakato, K. Ueda, H. Yano, and H. Tsubomura, *J. Phys. Chem.*, **92,** 2316 (1988).

[121] Y. Nakato, H. Yano, and H. Tsubomura, *Chem. Lett.*, 987 (1986).

[122] Y. Nakato, K. Ueda, and H. Tsubomura, *J. Phys. Chem.*, **90,** 5495 (1986).

[123] Y. Nakato and H. Tsubomura, *Ber. Bunsen-Ges. Phys. Chem.*, **91,** 405 (1987).

[124] Y. Nakato, S. Nishiura, H. Oshika, and H. Tsubomura, *Jpn. J. Appl. Phys.*, **28,** L261 (1989).

[125] K. Ueda, Y. Nakato, N. Suzuki, and H. Tsubomura, *J. Electrochem. Soc.*, **136,** 2280 (1989).

[126] Y. Nakato, H. Yano, S. Nishiura, T. Ueda, and H. Tsubomura, *J. Electroanal. Chem.*, **228,** 97 (1987).

[127] Y. Nakato and H. Tsubomura, *Electrochim. Acta*, **37,** 897 (1992).

[128] Y. Nosaka, Y. Ishizuka, and H. Miyama, *Ber. Bunsen-Ges. Phys. Chem.*, **90,** 1199 (1986).

[129] A. Kumar, Ph.D. Thesis: California Institute of Technology (1991), pp. 74-96.

[130] M. X. Tan, Research Proposal: California Institute of Technology, Division of Chemistry and Chemical Engineering (1991).

[131] C. D. Karp, Masters Thesis: California Institute of Technology, Division of Chemistry and Chemical Engineering (1995), pp. 18-55.

[132] S. Yae, R. Tsuda, T. Kai, K. Kikuchi, M. Uetsuji, T. Fuji, M. Fujitani, and Y. Nakato, *J. Electrochem. Soc.*, **141,** 3090 (1994).

[133] J. G. Jia, M. Fujitani, S. Yae, and Y. Nakato, *Electrochim. Acta*, **42,** 431 (1997).

[134] A. Meier, I. Uhlendorf, and D. Meissner, *Electrochim. Acta*, **40,** 1523 (1995).

[135] A. Meier and D. Meissner, *Multiple Nano Contacts*, in Nanoparticles in Solids and Solutions; J. H. Fendler and I. Dékány, Ed., Kluwer: Netherlands (1996), pp. 421-449.

[136] R. Hiesgen and D. Meissner, *Adv. Mater.*, **10,** 619 (1998).

[137] R. Hiesgen and D. Meissner, *J. Phys. Chem. B*, **102,** 6549 (1998).

[138] J. C. Hulteen and R. P. Van Duyne, *J. Vac. Sci. Technol., A*, **13,** 1553 (1995).

[139] H. W. Deckman and J. H. Dunsmuir, *Appl. Phys. Lett.*, **41,** 377 (1982).

[140] S. M. Sze, The Physics of Semiconductor Devices, 2nd ed., Wiley: New York (1981), pp. 291-2.

[141] E. H. Rhoderick and R. H. Williams, Metal-Semiconductor Contacts, 2nd ed., Oxford University Press: New York (1988), p. 55.

[142] R. D. Thompson and K. N. Tu, *Thin Solid Films*, **93,** 265 (1982).

[143] F.-R. F. Fan, R. G. Keil, and A. J. Bard, *J. Am. Chem. Soc.*, **105,** 220 (1983).

[144] P. E. Laibinis, C. E. Stanton, and N. S. Lewis, *J. Phys. Chem.*, **98,** 8765 (1994).

[145] H. Kobayashi, N. Takeda, H. Sugahara, and H. Tsubomura, *J. Phys. Chem.*, **95,** 813 (1991).

[146] K. E. Pomykal, A. M. Fajardo, and N. S. Lewis, *J. Phys. Chem.*, **100,** 3652 (1996).

[147] M. L. Rosenbluth, C. M. Lieber, and N. S. Lewis, *Appl. Phys. Lett.*, **45,** 423 (1984).

[148] G. A. Shreve, C. D. Karp, K. E. Pomykal, and N. S. Lewis, *J. Phys. Chem.*, **99,** 5575 (1995).

[149] Tung's work emerges from the solid-state physics community, and as a result the signs of the currents and electrochemical potentials in his original equations are reversed in sign relative to those herein.

[150] A. Many, Y. Goldstein, and N. B. Grover, Semiconductor Surfaces, North-Holland Publishing Co.: New York (1965), Chapter 4.

[151] C. G. B. Garrett and W. H. Brattain, *Phys. Rev.*, **99,** 376 (1955).

[152] S. M. Sze, The Physics of Semiconductor Devices, 2nd ed., Wiley: New York (1981), Section 7.2.1.

[153] M. X. Tan, P. E. Laibinis, S. T. Nguyen, J. M. Kesselman, C. E. Stanton, and N. S. Lewis, *Prog. Inorg. Chem.*, **41,** 21 (1994).

[154] N. S. Lewis and M. Rosenbluth, *Theory of Semiconductor Materials*, in Photocatalysis: Fundamentals and Applications; N. Serpone and E. Pelizzetti, Ed., John Wiley & Sons: New York (1989), pp. 45-98.

[155] ASTM, "Standard Practice for Conversion Between Resistivity and Dopant Density for Boron-Doped and Phosporus-Doped Silicon," ASTM (1988).

[156] Stagnant water absorbs carbon dioxide and other acidic gasses from the atmosphere and slowly acidifies. It was found that rinsing with even moderately acidic solutions reduced or even reversed the necessary hydrophilicity imparted to the samples by the KOH etch.

[157] T. B. Massalski, H. Okamoto, P. R. Subramanian, and L. Kacprzak, Ed., Vol. 2: *Binary Alloy Phase Diagrams*, ASM International: Materials Park, OH, (1990), pp. 1812-4.

[158] CAUTION: Lithium perchlorate reacts explosively with organics at these temperatures. Great care must be taken to ensure that no organic material is exposed to the molten salt. Lithium perchlorate also decomposes (presumably to $LiCl + O_2$) at temperatures above 400°C, so the temperature of the liquid salt must not approach this value.

[159] A measurable change in the properties of fully-metallized *n*-Si/Ni electrodes was reproducibly observed following their immersion in aqueous buffered HF solutions.

[160] Image SXM is a version of the Macintosh public domain software NIH Image extended to handle scanning probe microscopy images, developed by Dr. Steve Barrett and available from http://reg.ssci.liv.ac.uk. NIH Image was developed at the U.S. National Institutes of Health and is available on the Internet at http://rsb.info.nih.gov/nih-image/. I would like to thank Dr. Wayne Resband of the National Institutes of Health and Dr. Steve Barrett of the University of Liverpool for placing their computer code (ImageNIH / ImageSXM) in the public domain.

[161] A. J. Bard and L. R. Faulkner, Electrochemical Methods: Fundamentals and Applications, John Wiley & Sons: New York (1980), p. 30.

[162] S. M. Sze, The Physics of Semiconductor Devices, 2nd ed., Wiley: New York (1981), pp. 262-4.

[163] Several attempts were made to characterize the SC/M|E electrode surfaces by scanning electron microscopy (SEM). While this technique was more efficient than TMAFM for the analysis of large scale nanopatterns, it was not capable of sufficient contrast between the Ni and Si regions at low enough noise levels to provide reliable particle size statistics for the smallest particles. In the interest of consistency, TMAFM images were thus collected and analyzed for all nanopatterns.

[164] N. D. Denkov, O. D. Velev, P. A. Kralchevsky, I. B. Ivanov, H. Yoshimura, and K. Nagayama, *Langmuir*, **8,** 3183 (1992).

[165] A. S. Dimitrov and K. Nagayama, *Langmuir*, **12,** 1303 (1996).

[166] J. C. Hulteen, D. A. Treichel, M. T. Smith, M. L. Duval, T. R. Jensen, and R. P. Van Duyne, *J. Phys. Chem. B*, **103,** 3854 (1999).

[167] L. R. Zheng, L. S. Hung, and J. W. Mayer, *J. Vac. Sci. Technol., A*, **1,** 758 (1983).

[168] E. H. Rhoderick and R. H. Williams, Metal-Semiconductor Contacts, 2nd ed., Oxford University Press: New York (1988), pp. 197-202.

[169] H. Kobayashi, F. Mizuno, Y. Nakato, and H. Tsubomura, *J. Phys. Chem.*, **95,** 819 (1991).

[170] See Y. Nakato and H. Tsubomura, *Electrochim. Acta*, **37,** 897 (1992), and references therein.

Table 1: Variable definitions for equations 27 and 28: interacting contact (pinch-off) model[a]

[a]For an *n*-type SC/M|E electrode patterned with isolated, periodic, low contact potential SC/M regions on a strongly inverted SC/E field

Symbol	Variable	Definition or value	Units
A_{dots}	Expected diode quality factor for M dots on SC/M|E surface	$A_{dots} \approx A_M$	dimensionless
A_ℓ	Observed diode quality factor at SC/E electrodes	Determined experimentally from measurements at SC/E electrodes	dimensionless
A_{loc}	Expected local diode quality factor for SC/M|E contact	$A_{loc} \approx A_{dots} + \Gamma$	dimensionless
A_M	Observed diode quality factor for SC/M electrodes	Determined experimentally from measurements at SC/M electrodes	dimensionless
A^{**}	Effective Richardson constant	$A^{**} = 120\ A \cdot cm^{-2} \cdot T^{-2}$	$A \cdot cm^{-2} \cdot T^{-2}$
q	Elementary charge	$q = 1.602 \times 10^{-19}$ Coulombs	Coulombs
f_{actual}	Actual area fraction of M on nanopatterned surface	Determined from TMAFM images	dimensionless
f_{eff}	Effective area fraction of M dots on SC/M|E surface	$f_{eff} \equiv S_{eff}\, \rho_{dots}$	dimensionless
$J_{o,\,bare}$	Effective exchange current through bare portions of SC/M|E	$J_{o,\,bare} = (1 - f_{actual})\, J_{o,\,\ell}$	$A \cdot cm^{-2}$
$J_{o,\,dots}$	Effective exchange current through M dots on SC/M|E surface	$J_{o,\,dots} = A^{**}\, T^2\, f_{eff}\, \exp\left(\frac{q\,\Phi_{eff}}{k\,T}\right)$	$A \cdot cm^{-2}$
$J_{o,\,\ell}$	Observed exchange current density at SC/E electrodes	Determined experimentally from measurements at SC/E electrodes	$A\ cm^{-2}$
k	Boltzmann constant	$k = 1.381 \times 10^{-23}\ J \cdot K^{-1}$	$J \cdot K^{-1}$
N_C	Effective density of states in semiconductor conduction band	$N_C = 2.8 \times 10^{19}\ cm^{-3}$ in Si	cm^{-3}
N_D	Donor dopant density in semiconductor	Extracted from measured resistivity[155]	cm^{-3}
n_i	Intrinsic carrier concentration in undoped semiconductor	$n_i = 1.45 \times 10^{10}\ cm^{-3}$ in Si	cm^{-3}
R_o	Effective radius of M particles on SC/M|E surface	Determined from TMAFM images	nm or cm
S_{eff}	Effective area of each M dot on SC/M|E surface	$S_{eff} = \frac{4\,\pi\,\gamma\,\eta^{2/3}\,k\,T}{9\,q\,(U_{bb})^{2/3}}$	cm^2

Table 1, continued

Symbol	Variable	Definition or value	Units
T	Temperature	Measured directly during experiments	K
V_{app}	Corrected applied potential across electrochemical device	See equation 29	V
U_{bb}	Surface potential of macroscopic SC/E contact	$U_{bb} = U_{inv} + V_{app}$	V
U_{inv}	Surface potential at strong inversion limit[152]	$U_{inv} = \frac{2\,k\,T}{q} \ln\left(\frac{N_D}{n_i}\right)$	V
V_n	Fermi level to conduction band minimum potential offset in semiconductor bulk	$V_n = \frac{k\,T}{q} \ln\left(\frac{N_C}{N_D}\right)$	V
Δ	Surface potential difference, SC/E vs SC/M	$\Delta = \Phi_B^* - \Phi_{B,\,M}$	V
$\Phi_{B,\,M}$	Observed barrier height at SC/M electrode	Determined experimentally from measurements at SC/M electrodes	V
Φ_{eff}	Effective barrier height of each M dot on SC/M|E surface	$\Phi_{eff} = \Phi_B^* - \gamma \sqrt[3]{\frac{U_{bb}}{\eta}}$	V
Φ_B^*	Barrier height equivalent at strong inversion limit	$\Phi_B^* \equiv U_{inv} + V_n$	V
γ	Region parameter[21]	$\gamma \equiv 3\left(\frac{R_o^2\,\Delta}{4}\right)^{1/3}$	$V^{1/3}\,cm^{2/3}$
Γ	Space charge parameter[21]	$\Gamma \equiv \left(\frac{R_o^2\,\Delta}{4\,\eta\,U_{bb}^2}\right)^{1/3}$	dimensionless
η	Debye parameter	$\eta \equiv \frac{\varepsilon_s}{q\,N_D}$	$cm^2\,V^{-1}$
ρ_{dots}	Number density of M particles on SC/M|E surface	$\rho_{dots} = \frac{f_{actual}}{\pi\,R_o^2}$	cm^{-2}

Table 2: Variable definitions for equations 27 and 28: independent (non-interacting) contact model[a]

[a]Applicable to any SC/M|E system operating outside the pinch-off regime

Symbol	Variable	Definition or value	Units
A_{dots}	Expected diode quality factor for M dots on SC/M|E surface	$A_{dots} \approx A_M$	dimensionless
A_ℓ	Observed diode quality factor at SC/E electrodes	Determined experimentally from measurements at SC/E electrodes	dimensionless
A_M	Observed diode quality factor for SC/M electrodes	Determined experimentally from measurements at SC/M electrodes	dimensionless
A^{**}	Effective Richardson constant	$A^{**} = 120\ A \cdot cm^{-2} \cdot T^{-2}$	$A \cdot cm^{-2} \cdot T^{-2}$
q	Elementary charge	$q = 1.602 \times 10^{-19}$ Coulombs	Coulombs
f_{actual}	Actual area fraction of M on nanopatterned surface	Determined from TMAFM images	dimensionless
$J_{o,\ bare}$	Effective exchange current through bare portions of SC/M|E surface	$J_{o,\ bare} = (1 - f_{actual})\, J_{o,\ \ell}$	$A \cdot cm^{-2}$
$J_{o,\ dots}$	Effective exchange current through M dots on SC/M|E surface	$J_{o,\ dots} = A^{**}\, T^2\, f_{actual}\, \exp\left(\frac{q\, \Phi_{B,\ M}}{k\, T}\right)$	$A \cdot cm^{-2}$
$J_{o,\ \ell}$	Observed exchange current density at SC/E electrodes	Determined experimentally from measurements at SC/E electrodes	$A\ cm^{-2}$
$\Phi_{B,\ M}$	Observed effective barrier height at SC/M electrodes	Determined experimentally from measurements at SC/M electrodes	V
k	Boltzmann constant	$k = 1.381 \times 10^{-23}\ J \cdot K^{-1}$	$J \cdot K^{-1}$
T	Temperature	Measured directly during experiments	K
V_{app}	Corrected applied potential across electrochemical device	See equation 29	V

Table 3: Properties of *n*-type silicon used in this work

Wafer designation	Wafer thickness, cm	Measured resistivity, Ω cm	Empirical[155] N_D, cm^{-3}
Si-E2	0.0525 ± 18	5.35 ± 0.20	$8.4 \pm 0.3 \times 10^{14}$
Si-E3	0.0525 ± 18	5.56 ± 0.23	$8.1 \pm 0.3 \times 10^{14}$
Si-E4	0.0525 ± 18	5.85 ± 0.27	$7.7 \pm 0.4 \times 10^{14}$
Si-E5	0.0525 ± 18	5.91 ± 0.25	$7.6 \pm 0.2 \times 10^{14}$

Table 4: Typical bilayer crystal (nanosphere lithographic mask) growth conditions

Sphere diameter (D_s), nm	Sol concentration, $\%_{wt}$ polystyrene	Ambient growth temperature, C°	Relative humidity, %	Substrate extraction rate, $\mu m \cdot sec^{-1}$	Si wafers used (See Table 3)
174 ± 1.8	2.5	22.8	36	2.5	Si-E3 and Si-E4
365 ± 3.4	2.9	22.8	33	2.5	Si-E5
760 ± 1.4	9.5	22.8	27	3.0	Si-E4
1530 ± 18	10.0	22.8	12	3.0	Si-E2

Table 5: Observed physical properties of nanosphere masks and nanopatterns

Nominal sphere diameter designation	174 nm	365 nm	760 nm	1530 nm
Sphere diameter used in mask (D_s), nm[a]	174 ± 1.8	365 ± 3.4	760 ± 1.4	1530 ± 18
Effective Ni dot radius (R_o), nm[b,c]	27.5 ± 6.7	56 ± 12	106 ± 25	260 ± 60
Interparticle spacing, nm[d]	203 ± 5	384 ± 9	763 ± 19	1630 ± 50
Fractional areal coverage of Ni (f_{actual})[c]	0.071 ± 0.007	0.090 ± 0.014	0.071 ± 0.010	0.090 ± 0.011
Number density of dots (ρ_{dots}), cm^{-2}	3.0×10^9	9.2×10^8	2.0×10^8	4.4×10^7
Geometrically expected number density, cm^{-2}	3.81×10^9	8.67×10^8	2.00×10^8	4.93×10^7

[a]Manufacturers' reported physical diameters as obtained by transmission electron or optical array microscopy
[b]Radius of a circular region having the same area as the observed triangular Ni patch
[c]Obtained by tapping-mode atomic force microscopy, these values are approximate – the uncertainty indicated reflects only the variability in the measurements themselves, and is not intended to serve as an estimate of the accuracy of the method as a whole.
[d]Distance between centers of nearest-neighbor particles on patterned surface

Table 5, continued

Nominal sphere diameter designation	174 nm	365 nm	760 nm	1530 nm
Point vacancy defect density, cm^{-2}	8×10^6	8×10^6	4×10^6	1×10^6
Point vacancy defect effective radius, nm[e]	51 ± 17	126 ± 31	200 ± 80	540 ± 180
Point defect area fraction (upper bound)[f]	0.00052	0.0036	0.0039	0.0075
Dislocation density,[g] cm/cm^2	3.0×10^3	8.2×10^2	5.7×10^2	8.3×10^1
Dislocation defect particle density (upper limit), cm^{-2}	3.0×10^8	4.3×10^7	1.5×10^7	1.0×10^6
Dislocation defect effective radius, nm[e]	41 ± 10	70 ± 18	122 ± 32	390 ± 120
Dislocation defect area fraction (upper bound)[f]	0.00262	0.00013	0.00059	0.0016
Grain boundary density,[g] cm/cm^2	3.6×10^2	1.3×10^2	6.3×10^2	9.8×10^1
Grain size lower limit, μm[h]	56	150	32	200
Dominant source of defect particles of radius > $2R_o$	Dislocations	Point Vacancies	Point Vacancies	Point Vacancies
Total defect area fraction (upper bound)[h,i]	0.0031	0.0037	0.0040	0.0091

[e]Average effective radius of the largest Ni particle produced by a point vacancy defect
[f]Area fraction of electrode covered by defect-related particles of effective radius > $2R_o$
[g]The density of this one-dimensional defect is reported as the length of defect expected per unit area of nanopatterned substrate.
[h]Assuming square grains, the edge size of the grains as given by equation 35
[i]Total does not include grain boundary defects, which produce negligible defect area contributions for all values of D_s.

Table 6: Parameter values employed in application of equations 5, 7, 27, and 28

D_s, nm	174	365	760	1530
A_ℓ	2.02	1.90	1.75	1.92
A_M	1.64	2.04	1.21	2.03
f_{actual}	0.071	0.090	0.071	0.090
$J_{o,\,\ell}$, A·cm^{-2}	5.16×10^{-7}	8.78×10^{-8}	1.41×10^{-7}	1.13×10^{-7}
N_D, cm^{-3}	7.90×10^{14}	7.61×10^{14}	7.70×10^{14}	8.43×10^{14}
$R_{o,}$ nm	27.5	55.8	106	256
T, K	299.5	299.0	298.7	299.6
U_{bi}, V	0.563	0.560	0.560	0.567
V_{inv}, V	0.563	0.560	0.560	0.567
V_n, V	0.278	0.280	0.280	0.277
W ($V_{app} = 0$), nm	968	984	978	940
Δ, V	0.221	0.240	0.152	0.256
η, cm^2 V^{-1}	8.32×10^{-9}	8.64×10^{-9}	8.55×10^{-9}	7.80×10^{-9}
γ, $V^{1/3}$ $cm^{2/3}$	2.2×10^{-4}	3.7×10^{-4}	4.9×10^{-4}	1.04×10^{-3}
Γ ($V_{app} = 0$)	0.0541	0.0882	0.117	0.256
$\Phi_{B,\,M}$, V	0.621	0.601	0.688	0.587
Φ_B^*, V	0.842	0.840	0.840	0.843
ρ_{dots}, cm^{-2}	2.99×10^9	9.20×10^8	2.01×10^8	4.37×10^7

Table 7: Numeric results of interacting contact (pinch-off) model applied to *n*-Si/Ni|E electrodes[a]

[a]Where applicable, values are for equilibrium conditions ($V_{app} = 0$, $J = 0$) and employ the measured value of the effective particle radius (R_o).

Sphere Diameter (D_s), nm	174	365	760	1530
Actual fractional areal coverage of Ni (f_{actual})	0.071	0.090	0.071	0.090
Effective fractional areal coverage of Ni (f_{eff})	0.145	0.076	0.022	0.009
Effective Ni area : Actual Ni area (f_{eff}/f_{actual})	2.05	0.84	0.30	0.10
Measured effective particle radius (R_o), nm[b]	27.5 ± 6.7	56 ± 12	106 ± 25	260 ± 60
Best fit effective particle radius (R_o, fit), nm[b, d]	30.7	63	95	156[e]
Geometrically expected effective particle radius, nm[b]	17.3	36.3	75.6	152
Critical effective particle radius $\left(\frac{\Delta W}{2 V_{bb}}\right)$, nm[c]	190	211	133	212
Calculated solution barrier height equivalent (Φ_B^*), V	0.842	0.840	0.840	0.843
Best fit solution barrier height equivalent (Φ_B^*, fit), V[d]	0.832	0.819	0.869	1.25[e]
Analytic model estimate of effective barrier height (Φ_{eff}), V	0.750	0.692	0.644	0.408[e]
Point dipole estimate of effective barrier height (Φ_{eff}), V	0.752	0.696	0.652	0.449[e]
Dipole layer estimate of effective barrier height (Φ_{eff}), V	0.758	0.711	0.697	0.590[f]
Fraction of exchange current passing through Ni particles ($J_{o,\,dots} / [J_{o,\,dots} + J_{o,\,bare}]$)	0.439	0.957	0.960	1.000

[b]Radius of a circular dot having the same area as the triangular Ni dot formed

[c]The largest particle radius satisfying equation 6; particles with larger effective radii are not expected to exhibit the pinch-off effect.

[d]The optimal value obtained in fitting the experimental data with equation 27, when this variable is allowed to float and all others are held constant

[e]The interacting contact model is not applicable to these cases because the particles are not pinched off: the measured R_o exceeds the critical effective particle radius. These values are included in order to demonstrate the trends in the best fit parameters as the model becomes unable to adequately represent reality.

[f]The dipole layer model (correctly) predicts that this contact will not be pinched-off. The potential maximum along the central axis of the dipole layer occurs at the semiconductor surface, as shown in Figure 13d.

Table 8: Nanoparticles used in this work

Physical diameter(D_s), nm	Hydrodynamic diameter, nm	Manufacturer	Manufacturer's lot number	Chemical composition of nanospheres
174 ± 1.8[a]	203[c]	Seradyn, Inc. Indianapolis, IN	440CP3	Carboxylate-modified polystyrene
365 ± 3.4[a]	401[c]	Seradyn, Inc. Indianapolis, IN	612L	Carboxylate-modified polystyrene
760 ± 1.4[a]	777[c]	Seradyn, Inc. Indianapolis, IN	701T	Unmodified (sulphate-terminated) polystyrene
1530 ± 180[b]	–	Duke Scientific Corp. Palo Alto, CA	20109	Unmodified (sulphate-terminated) polystyrene

[a]Manufacturer's value as determined by transmission electron microscopy.
[b]Manufacturer's value as determined by optical array microscopy.
[c]Manufacturer's value as determined by quasielastic light scattering. These particles are catalogued based on this diameter.

Table 9: Best fit parameters obtained by application of diode equation (equation 32) to dark J-V curves

Sphere diameter used in mask (D_s), nm	174	365	760	1530
Number of SC/E electrodes included in average (n)	13	9	4	8
SC/E temperature (T), C°	25.7 ± 1.2	26.2 ± 1.1	25.6 ± 0.5	24.5 ± 2.4
SC/E exchange current density ($J_{o,\ \ell}$), A·cm^{-2}	$5.2 \pm 1.5 \times 10^{-7}$	$8.8 \pm 2.8 \times 10^{-8}$	$1.4 \pm 0.4 \times 10^{-7}$	$1.1 \pm 0.4 \times 10^{-7}$
SC/E effective barrier height ($\Phi_{obs,\ \ell}$), V	0.790 ± 0.008	0.837 ± 0.009	0.822 ± 0.010	0.825 ± 0.011
SC/E observed diode quality factor ($A\ell$)	2.02 ± 0.15	1.90 ± 0.16	1.75 ± 0.13	1.92 ± 0.17
Number of SC/M|E electrodes included in average (n)	6	3	5	7
SC/M|E temperature (T), C°	26.4 ± 1.1	25.8 ± 0.1	25.5 ± 0.9	26.5 ± 1.0
SC/M|E exchange current density (J_o), A·cm^{-2}	$9.9 \pm 3.0 \times 10^{-7}$	$2.5 \pm 0.8 \times 10^{-6}$	$5.5 \pm 1.7 \times 10^{-6}$	$4.8 \pm 3.2 \times 10^{-5}$
SC/M|E observed effective barrier height (Φ_{obs}), V	0.775 ± 0.008	0.749 ± 0.008	0.728 ± 0.008	0.675 ± 0.017
SC/M|E observed diode quality factor (A)	1.83 ± 0.13	2.13 ± 0.20	1.73 ± 0.15	1.8 ± 0.6
Number of SC/M electrodes included in average (n)	14	12	4	7
SC/M temperature (T), C°	25.6 ± 1.1	26.1 ± 0.3	25.2 ± 0.5	26.7 ± 1.1
SC/M exchange current density[a] ($J_{o,\ M}$), A·cm^{-2}	$4 \pm 21 \times 10^{-4}$	$8.1 \pm 11.4 \times 10^{-4}$	$2.6 \pm 1.6 \times 10^{-5}$	$1.5 \pm 7.8 \times 10^{-3}$
SC/M effective barrier height[a] ($\Phi_{B,\ M}$), V	0.62 ± 0.15	0.60 ± 0.04	0.688 ± 0.017	0.59 ± 0.14
SC/M observed diode quality factor[a] (A_M)	1.6 ± 7.8	2.0 ± 2.0	1.2 ± 0.3	2.0 ± 9.1

[a]The large uncertainty in these values reflects the limited number of data points that could be collected before the mass transport limit was reached.

X. FIGURES

Figure 1. Band-energy diagram for an ideal semiconductor heterojunction at equilibrium. The contact potential across a heterojunction drops primarily across the least-polarizable phase. Here, a lightly doped *n*-type semiconductor has been brought into intimate contact with a conductive material having a large work function. As a result, electrons have transferred from the dopant atoms in the semiconductor to the surface of the contacting phase just opposite the interface. This has left behind a region of completely ionized, immobile dopant atoms in the semiconductor. This region is called the depletion region, and it supports a "built-in" electric potential, U_{bi}. The built-in potential gives rise to the rectifying properties of the junction: the larger the depletion region (at a given dopant density), the larger the built-in potential becomes and the more effective a rectifier the junction is expected to be. The built-in potential is ideally expected to be linearly related to the work function of the contacting phase, ϕ_{cp}. E_F = Fermi level, E_g = semiconductor bandgap; CB = conduction band edge, VB = valence band edge; Vac = local vacuum level; U_{bi} = built-in potential, V_c = contact potential, Φ_B = barrier height; χ_{sc} = semiconductor electron affinity, ϕ_{sc} = semiconductor work function, ϕ_{cp} = work function of contacting phase

Figure 1, continued

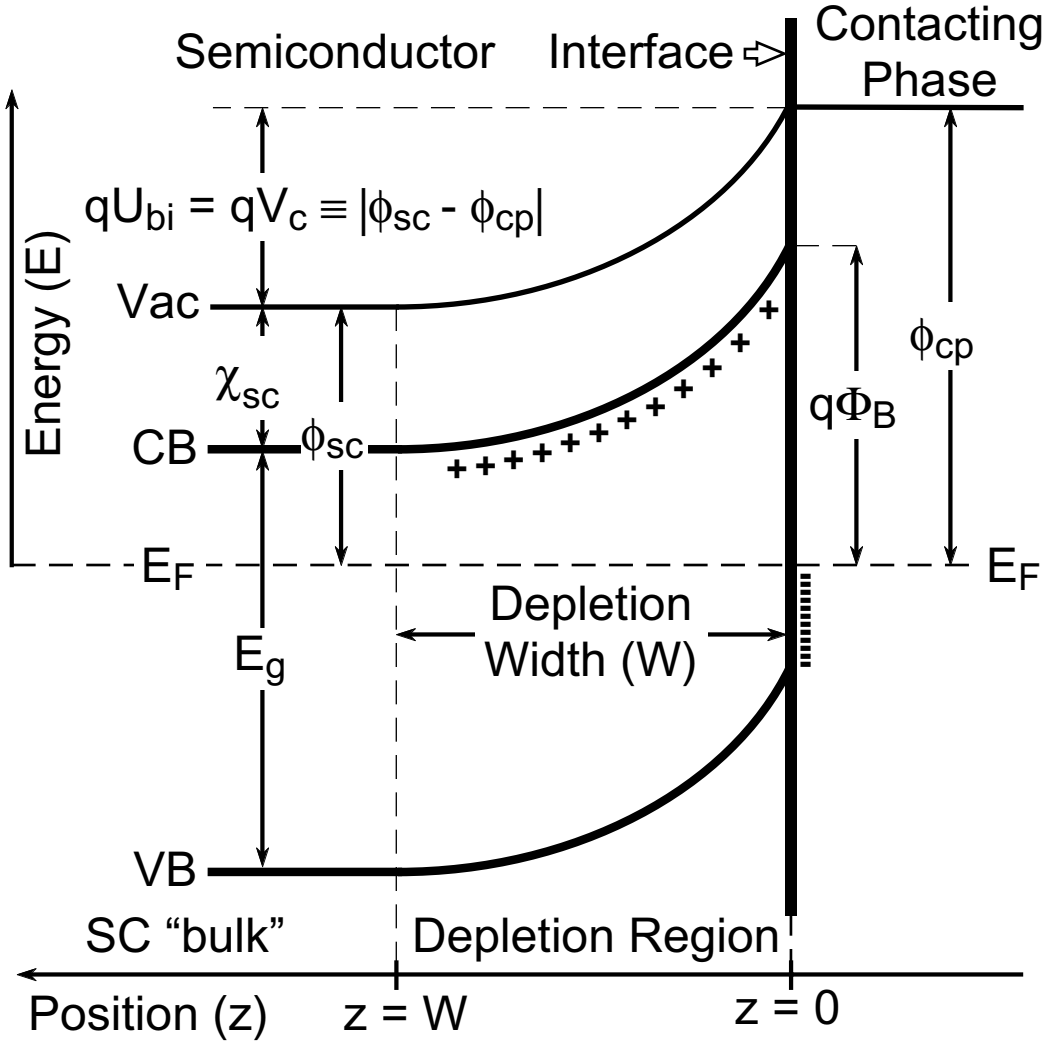

Figure 2. Deviations from ideal interfacial energetics at semiconductor heterojunctions. **(a)** A portion of the contact potential drops across an insulating layer (IL) between a semiconductor and the contacting phase. This does not reduce the efficacy of the resulting diode; to the contrary, it improves it. However, it places a resistance in series with this more effective diode, an impediment to solar energy conversion and power electronics applications. (The effect of the insulating layer may be considerably more complex if, as is often the case, the insulator can accumulate and store a significant internal charge.)

(b) and (c) "Fermi level pinning" occurs as a result of interfacial states (IS), either (b) localized or (c) distributed in energy. In this case there is no additional resistance developed across the junction because the potential barrier associated with the surface states is thin enough to be readily tunneled through. However, the rectification capability of the diode structure is different than it would have been in the absence of the interfacial states, and depends not only on the work function differential but also the energetics of the interfacial states.

Figure 2, continued

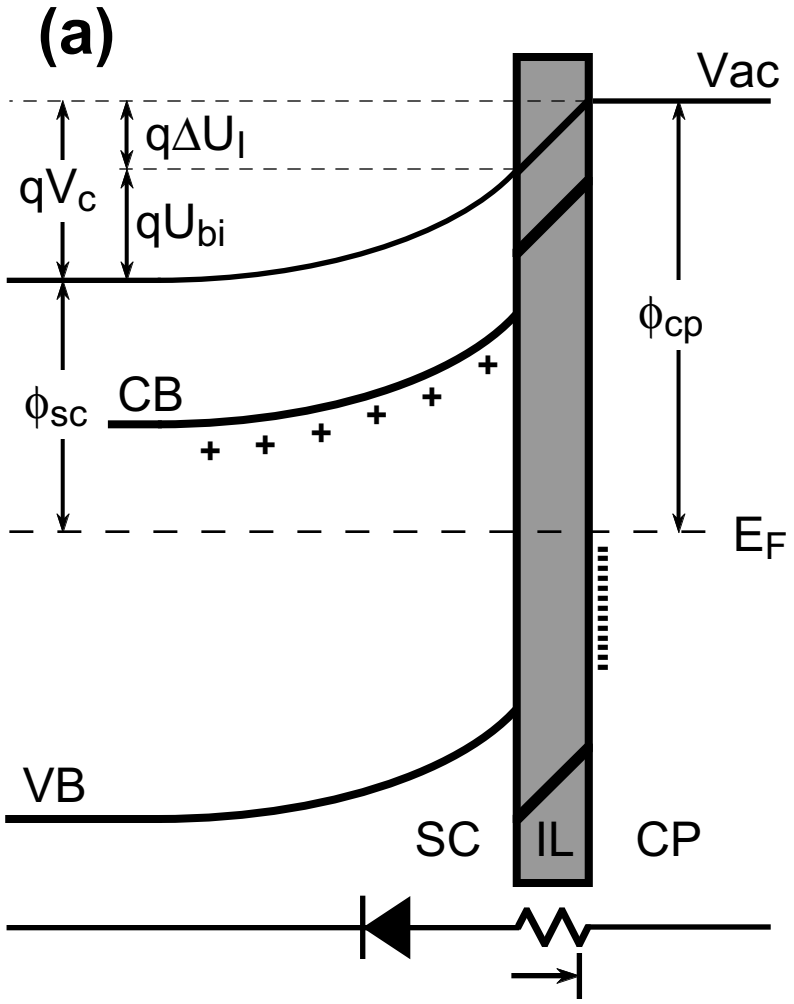

Figure 2, continued

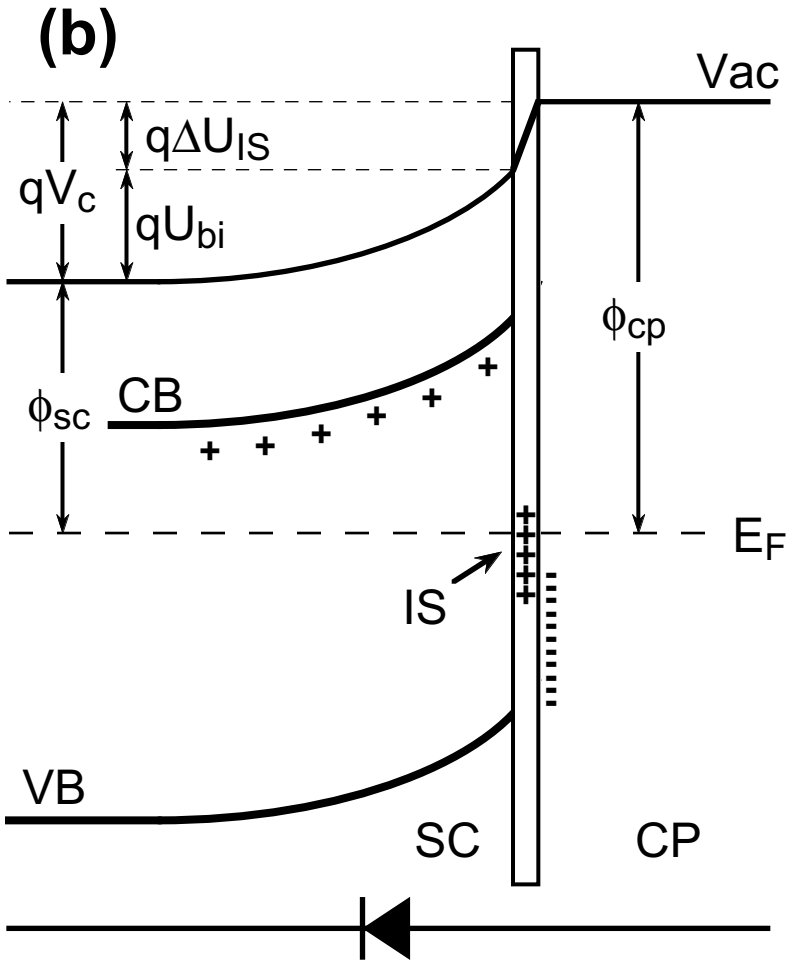

Figure 2, continued

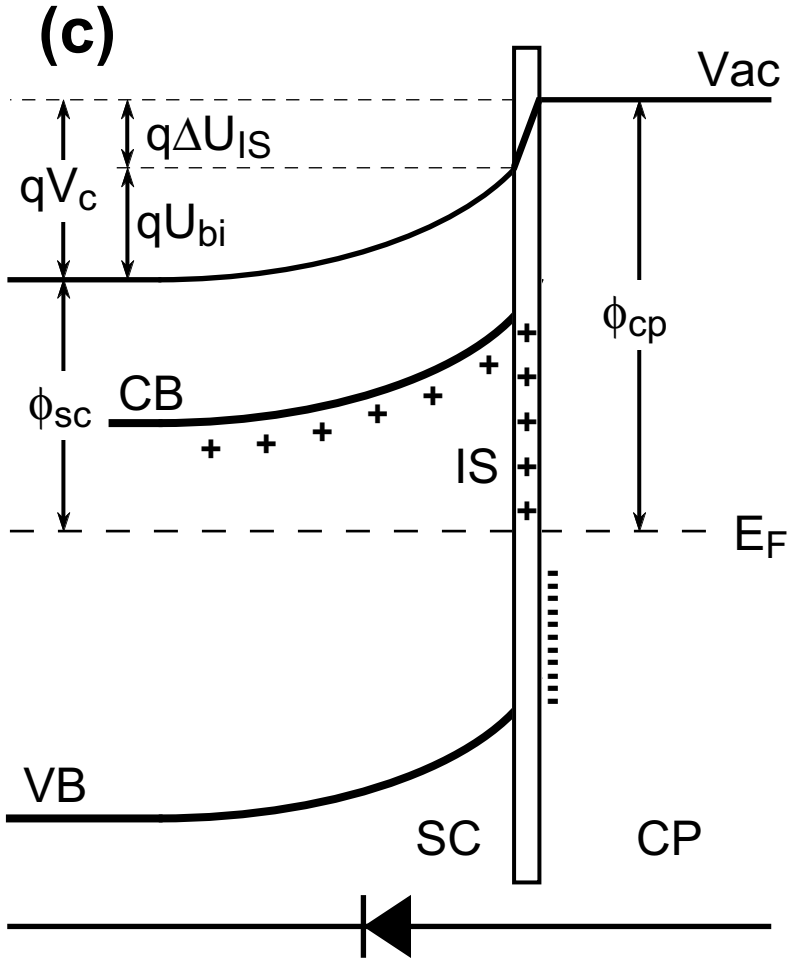

Figure 3. Separation of photogenerated charge carriers in a semiconductor. The electric field present in the depletion region of a semiconductor directs the movement of photogenerated charge carriers in opposite directions. When a photogeneration event occurs within the depletion region itself, the field immediately acts to separate the generated carriers. More often, the depletion region acts as a selective gate for photo-generated carriers diffusing to it following a photogeneration event in the field-free bulk in the semiconductor. In the example shown here, positively charged "holes" are swept to the semiconductor surface when they reach the edge of the depletion region, whereas negatively charged "free" electrons are repelled back into the bulk. Photogeneration occurs primarily in the semiconductor bulk for indirect-bandgap semiconductors, whereas a sizable proportion of it can occur in the depletion region for direct-bandgap semiconductors illuminated through the heterojunction.

Figure 3, continued

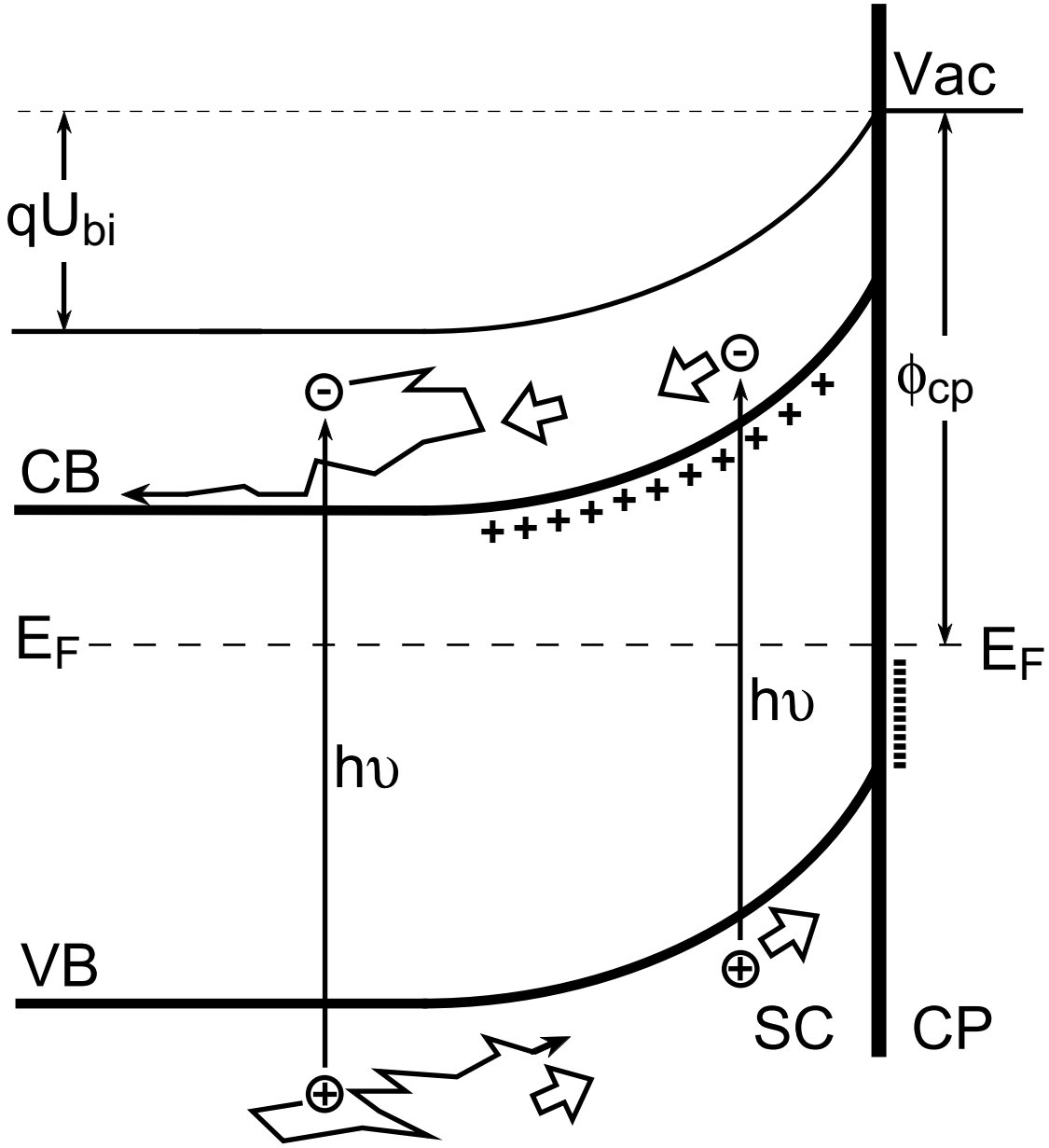

Figure 4. Variable and coordinate definitions employed in modeling inhomogeneous semiconductor contacts. (a) The Cartesian coordinate system and variable definitions applicable to equation 2. The surface potential at the semiconductor heterojunction interface has a base value of U_{bb}, modulated by a perturbation function $\delta(x, y)$. (b) The cylindrical coordinate system and variable definitions applicable to equations 4 - 6. The base value of the surface potential is again U_{bb}, but the system is now cylindrically symmetric and the perturbation term is fixed at a constant value of $-\Delta$ for all $\rho \leq R_o$. (c) Inhomogeneous SC/M model system definitions, applicable to equations 7 - 17. The semiconductor surface is covered with a SC/M junction of barrier height Φ_B^o everywhere except within a circular region of radius R_o centered at the origin, wherein a SC/M junction with a lower barrier height of $\Phi_{B,\,patch}$ contacts the n-type semiconductor surface. (d) SC/M|E model system for the case of a strongly inverted SC/E contact, applicable to equations 20 - 28. An n-type semiconductor is immersed in a redox-active solution capable of inducing strong inversion, leading to a band bending V_{inv} in the semiconductor and a corresponding equivalent barrier height Φ_B^*. A small circular patch of metal is present on the semiconductor surface at the coordinate origin; the SC/M barrier height is $\Phi_{B,\,M}$ and the patch radius is R_o.

Figure 4, continued

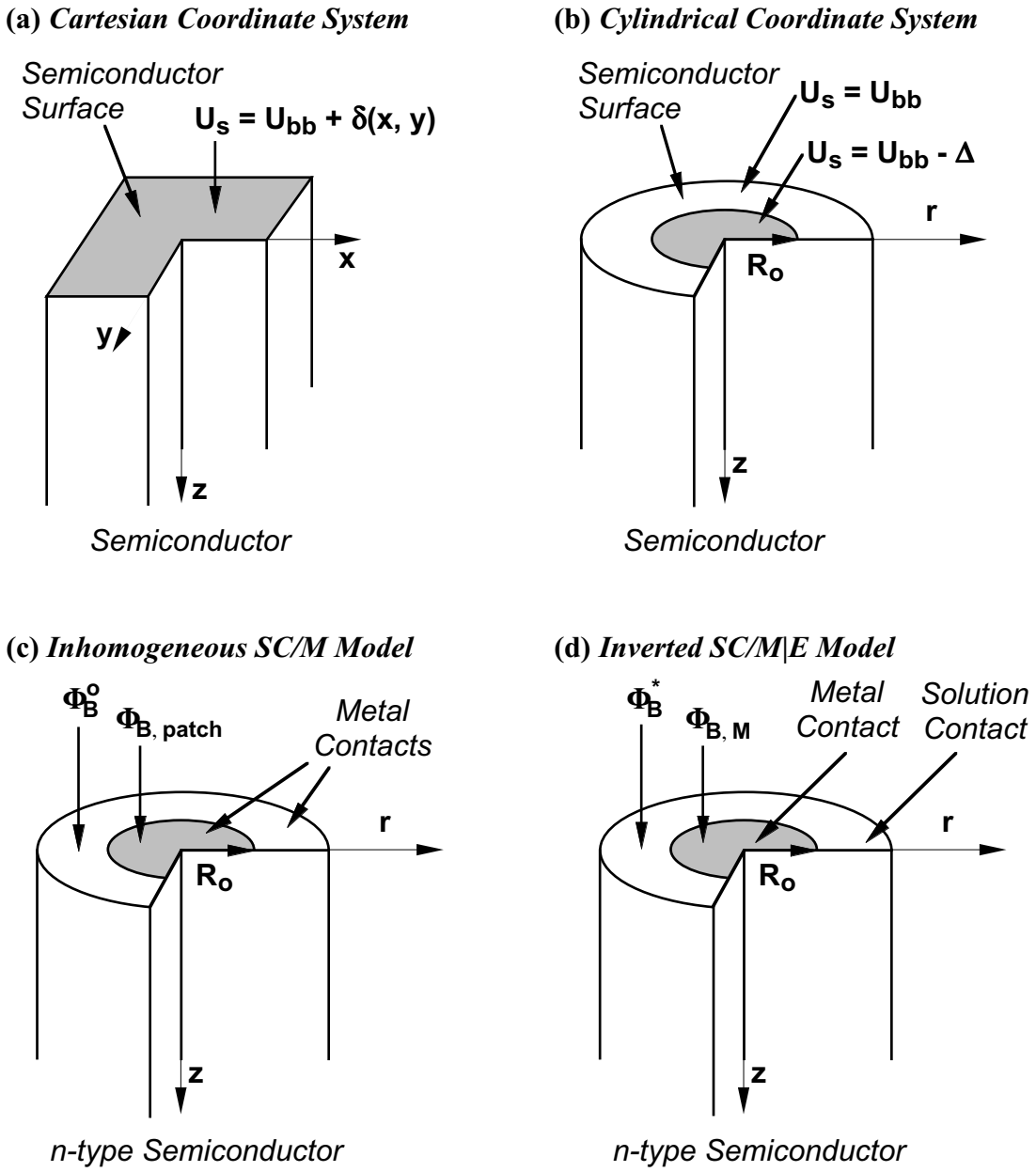

Figure 5. Calculated potential fields behind the *n*-Si/Ni|E structures employed in this work, based on the circular dipole layer model of equation 4. The coordinate system and variables used are those of Figure 1b. The cases represented here are those relevant to the SC/M|E electrode surfaces actually prepared in this study, formed using polystyrene nanospheres of diameter D_s (vide sequitur). (a) D_s = 174 nm. (b) D_s = 365 nm. (c) D_s = 760 nm. (d) D_s = 1530 nm; in this last case the circular Ni patch is not expected to exhibit the pinch-off effect.

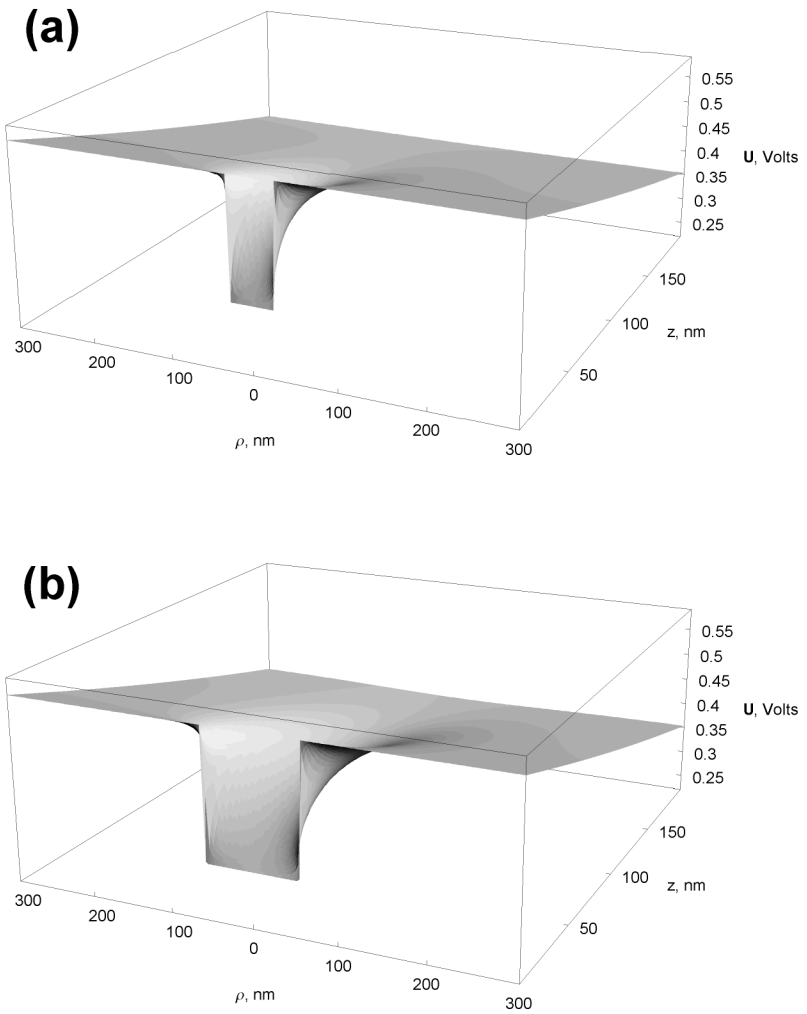

Figure 5, continued

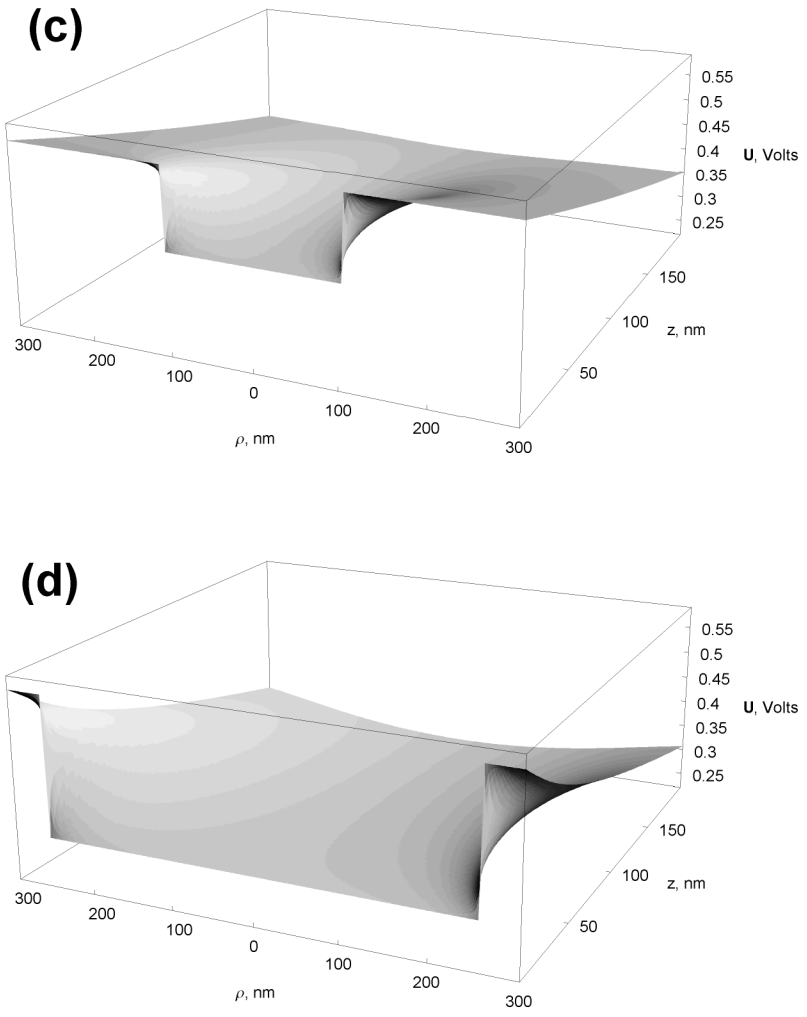

Figure 6. Equipotential contours within a semiconductor as a function of low barrier nanopattern scale. Calculated equilibrium potential contours for in homogenous barrier height interfaces, based on equation 4 and the assumption of simple superposition of electric potential perturbations. The model surfaces consist of metal disks of radius R_o, spaced $5 \cdot R_o$ apart, where (a) R_o = 20 nm, (b) R_o = 60 nm, or (c) R_o = 180 nm, on a 6.14 Ω·cm resistivity *n*-type Si substrate, with a doping density (N_D) of 7.2 x 10^{14} cm^{-3}, at 298 K. Other relevant parameters, as defined in Table 1 and Figure 4, are as follows: $\Phi_B^o = \Phi_B^* = 0.84$ V; $V_n = 0.28$ V; $\Delta = 0.20$ V; W = 1000 nm.

Figure 6, continued

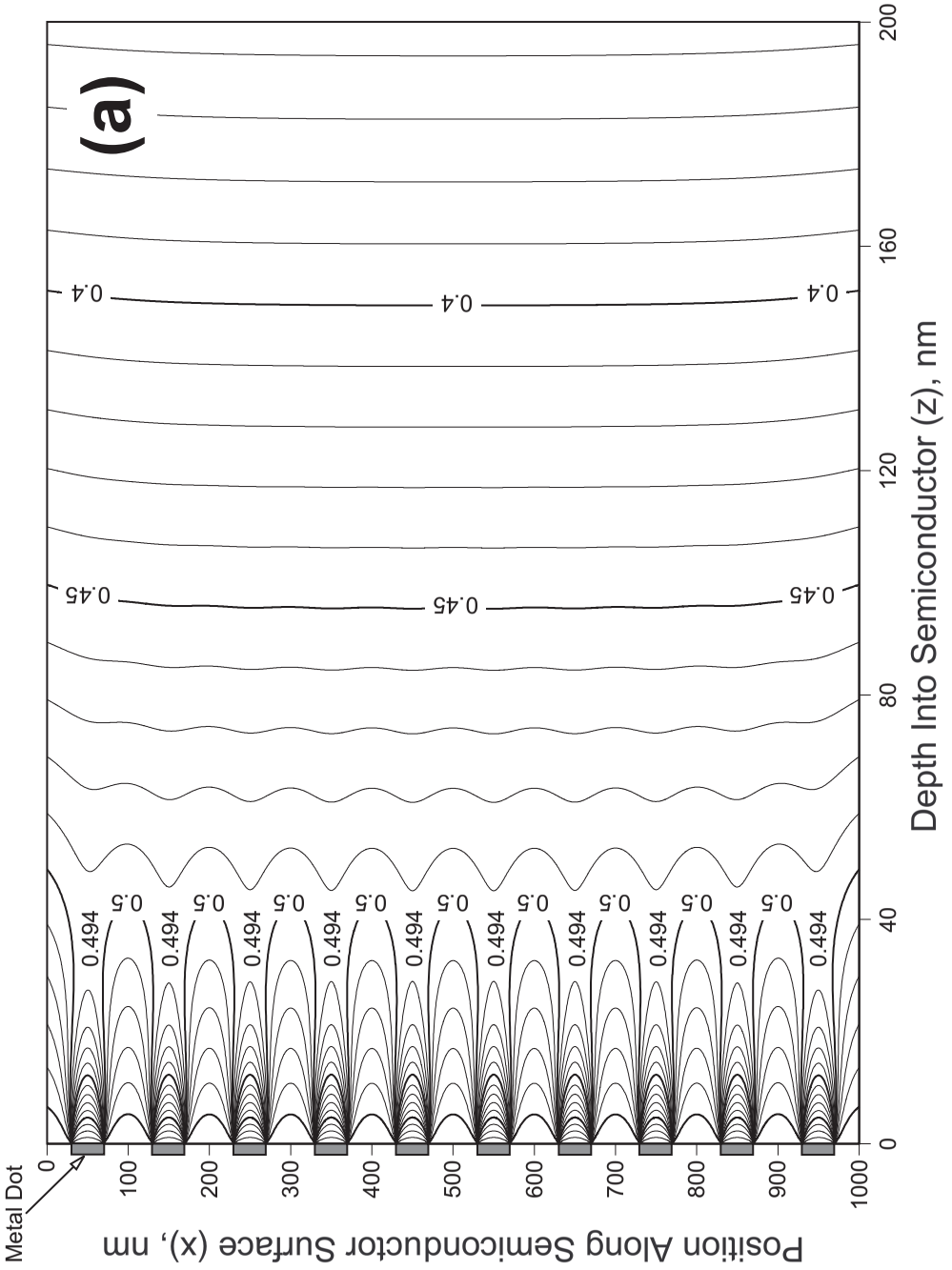

Figure 6, continued

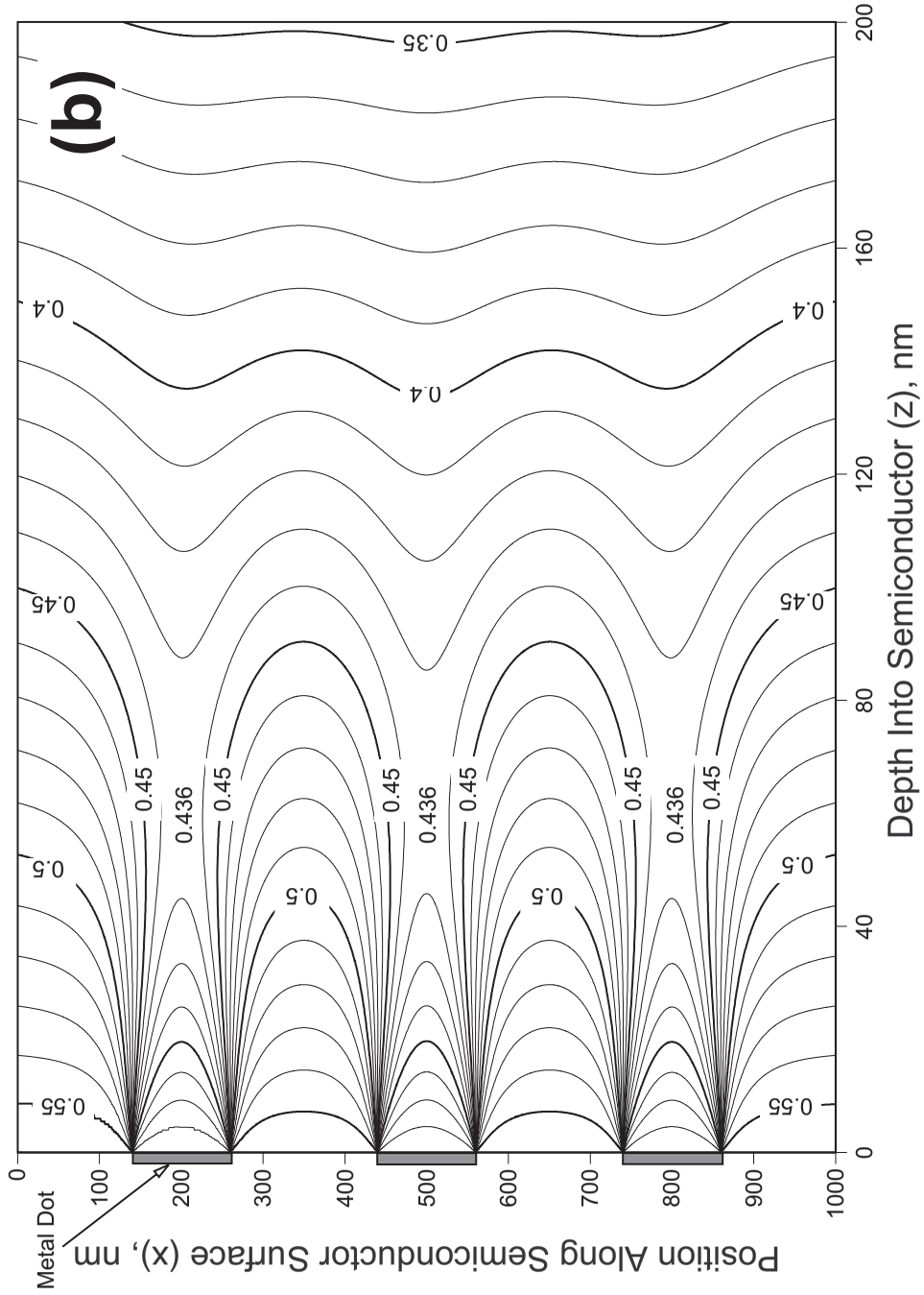

Figure 6, continued

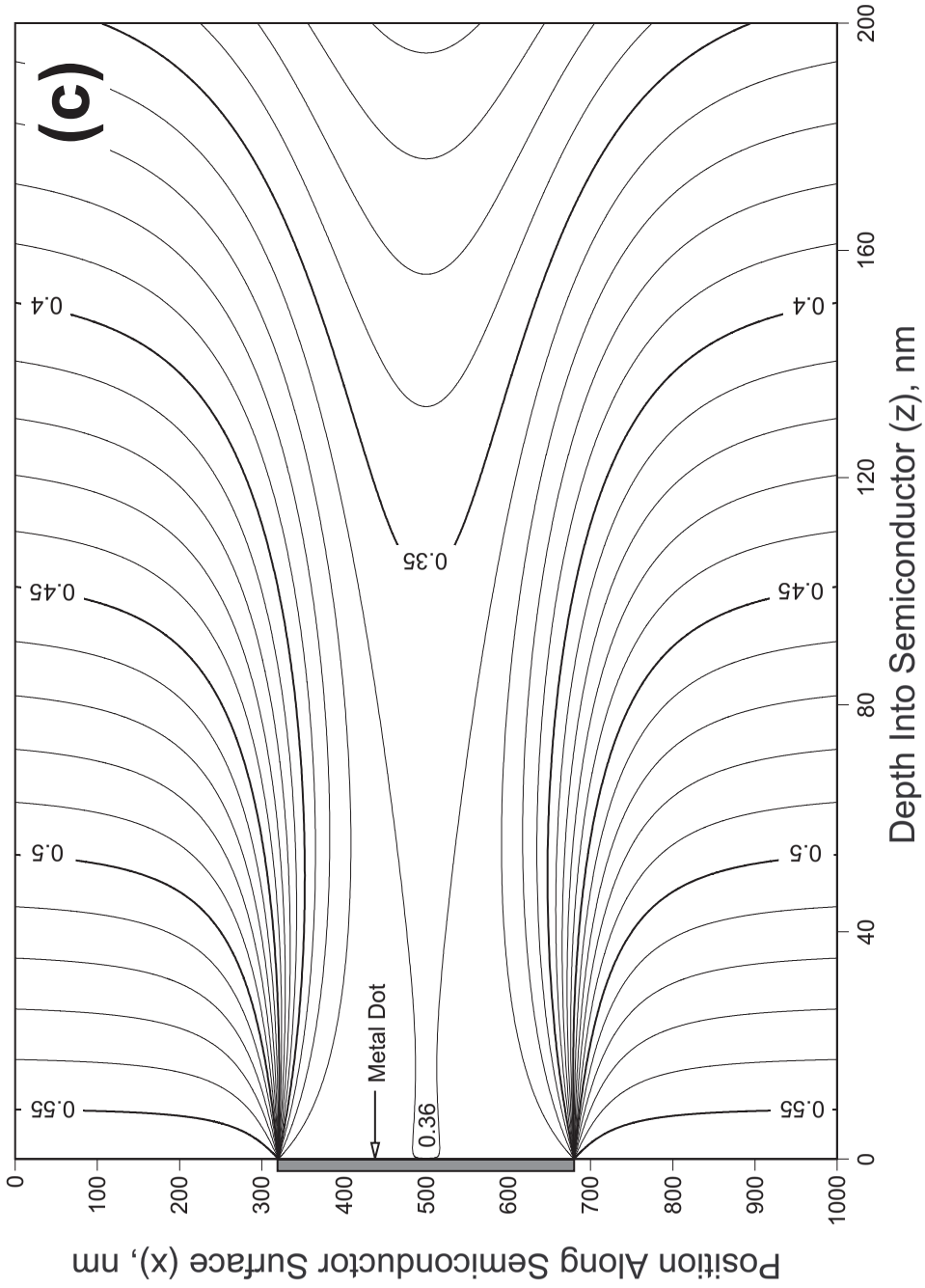

Figure 7. Conduction band diagram for a pinched-off heterogeneous contact. This scheme depicts the conduction band energy minimum as a function of position in a given *n*-type semiconductor. From top to bottom, the solid lines indicate the conduction band energy minimum behind a homogeneous contact of high barrier height Φ_B^o (top), behind a pinched-off mixed barrier height contact as shown in Figure 4c (center), and behind a homogeneous contact of low barrier height $\Phi_{B,\,patch}$ (bottom).

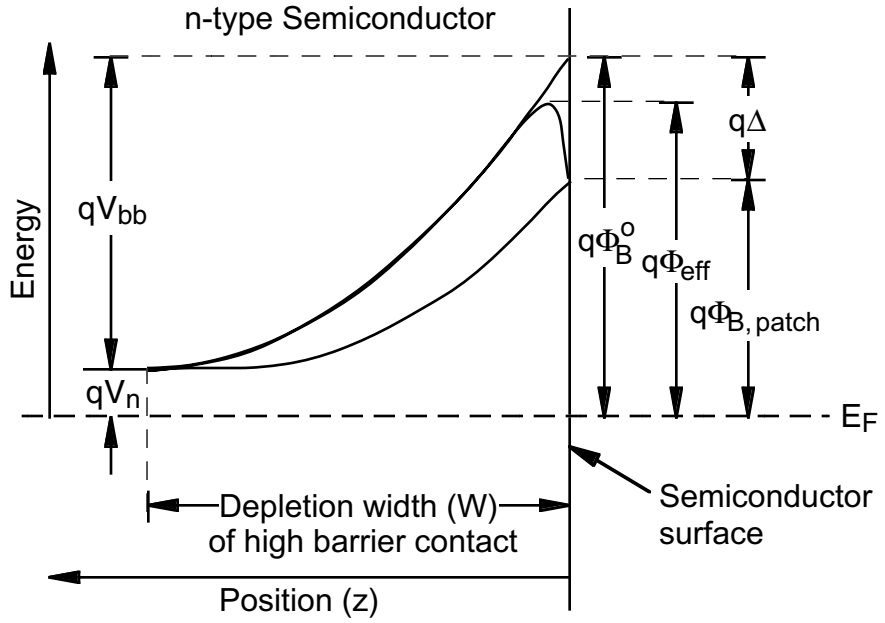

Figure 8. Apparatus and method employed in the preparation of two-dimensional crystals of nanospheres on silicon substrates. Both the nanospheres and the silicon substrate were very hydrophillic, such that the aqueous sol of nanospheres formed a meniscus on the silicon. As water evaporated from the meniscus, nanospheres were left behind on the semiconductor surface, eventually seeding a nanosphere crystal. These spheres being hydrophillic, the crystal remained water-logged and evaporation continued to occur from the crystal as it grew larger, drawing a flux of sol into the crystal that caused nanospheres to packed together at the crystal edge. By withdrawing the substrate from the sol at a properly selected speed, a steady-state condition was obtained wherein the evaporation from the water-logged crystal caused the formation of a close-packed two layer crystal at the growth interface at the same speed. Since the crystal would remain water-logged up to about 3 mm above the sol, steady-state conditions could only be obtained after that much substrate had been withdrawn; up to that point, the number of layers composing the nanosphere crystal was uncontrolled. The steady-state condition itself was usually metastable and slightly oscillatory: often the number of layers in the growing crystal would oscillate by one layer with a reliable periodicity. This periodicity had to be reduced (by adjusting the crystal growth conditions) to a point where a large contiguous two-layer crystal was obtained on the silicon surface.

Figure 8, continued

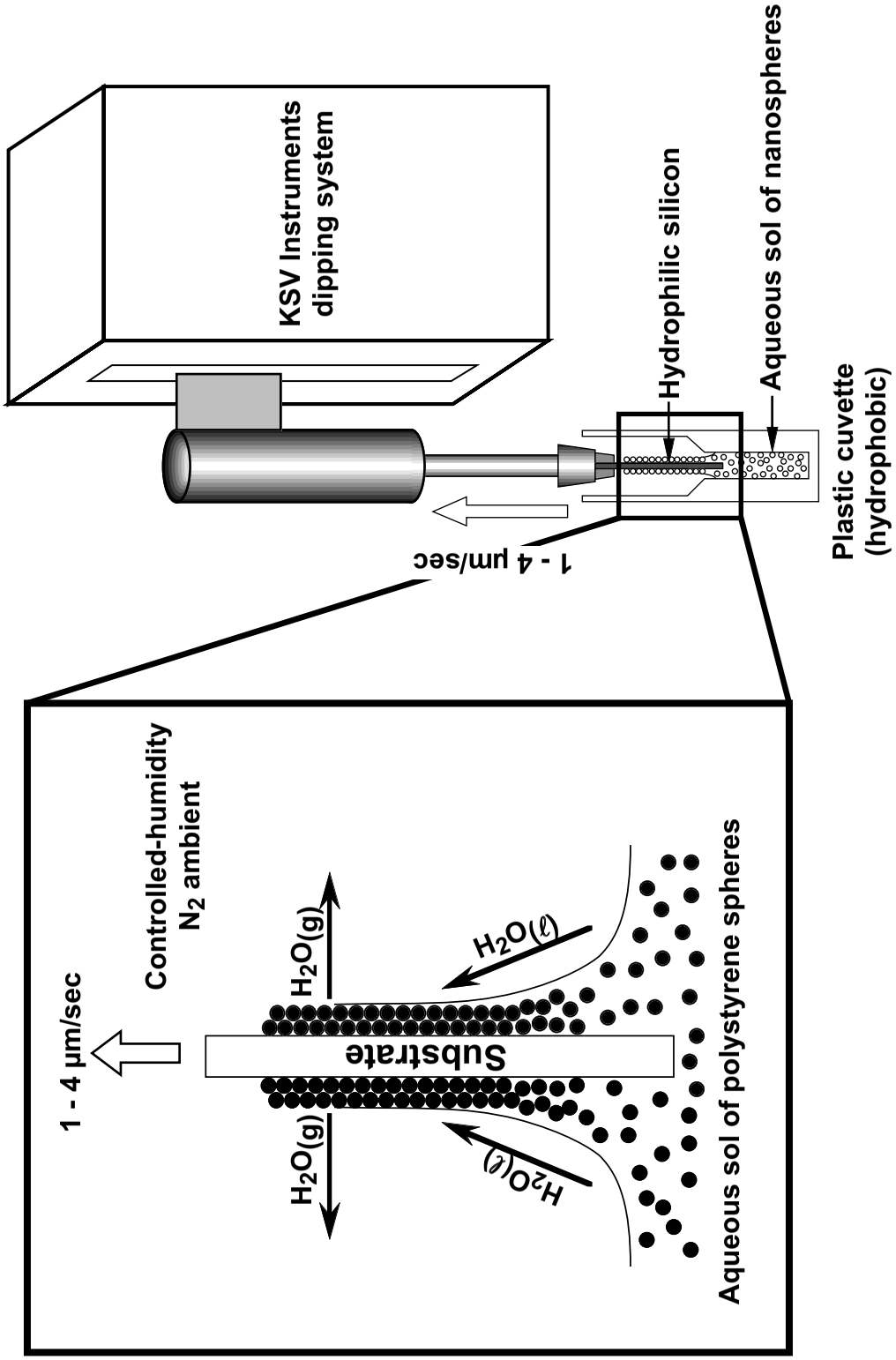

Figure 9. TMAFM images of nanosphere lithographic masks (a, b) and typical metal dot patterns prepared by nanosphere lithography (c, d). The mask in (a) consists of a two-layer crystal of 176 nm diameter polystyrene spheres grown on a silicon substrate. The spheres in the lower layer (not visible) pack such that every other hole between the spheres in the top layer is blocked by a sphere in the layer beneath. The remaining holes have a clear view down to the substrate, and these holes define the nickel patterns left on the wafer after metal evaporation. In this image a dislocation defect is clearly visible along the left edge, while five point vacancies can be seen in the top half of the image. The rightmost point vacancy can be seen to contain an undersized nanosphere. Image (b) is of a double-layer mask of 365 nm diameter nanospheres on a silicon substrate. Here two dislocations can be seen, running parallel to each other. The lowermost dislocation shifts where an oversize nanosphere has been incorporated into the crystal – this behavior was typical of dislocations, which often began, ended, and shifted along their length in response to over-sized spheres. The lower layer of nanospheres can be seen through the vacancies in the middle of this image. Evidence of an oversized sphere and an associated dislocation in the lower layer can also be seen at the center of this image, slightly below the midpoint. Images (c) and (d) are of typical Ni dot patterns produced by Ni deposition through two-layer crystal masks composed of 365 nm and 760 nm diameter latex spheres, respectively. In (c), a dislocation defect runs vertically through the left center portion of the image, leaving behind a telltale row of twin dots. Five point vacancy defects can also be seen in this image; the three to the left of the dislocation are oriented 180° to the two on the right. Analysis based on the positional registry of the defects suggests that all five point vacancies occurred in the same layer of the bilayer crystal, with the dislocation occurring in the other. The tendency of point defects to occur in the same layer was general, as was their tendency to reverse orientation across dislocations. Because point vacancies were often observed in images of the masks, we believe that they occur almost exclusively in the upper layer of the crystals. Image (d) is of a nanopattern

Figure 9, continued.

produced from a bilayer crystal of 760 nm diameter nanospheres. A low-angle grain boundary (arrowed) cuts across the lower left corner of this image, while several dislocations run through the image near vertical. Because the nanopattern resumes almost immediately on either side of the grain boundary, the position of the grain boundary must be correlated in the two layers of the crystal: it is fortuitous that such defects do not tend to lead to the formation of many large Ni patches. This image also serves to illustrate the variety of defect patterns that can be left behind by dislocations. Imaging conditions: Digital Instruments Nanoscope III TMAFM employing TESP probes and an E (a, c) or a J (b, d) scanner. Scan rate: 1.0 Hz (a, c) or 0.50 Hz (b, d); Setpoint: 1.62 V (a), 2.10 V (b), 1.46 V (c), 2.22 V (d); Free oscillation amplitude: 3.0 V; Scan angle: 45° (a, c), 0° (b, d); Sampling density: 512 x 512 pixels; Original scan size: 10 μm (a, c), 20 μm (b), 30 μm (d); Integral gain: 0.686 (a), 0.300 (b), 0.651 (c), 0.857 (d); Proportional gain: 8.0 (a), 10.0 (b), 6.1 (c), 10.9 (d); Look ahead gain: disabled; All images were planefit corrected to a third-order polynomial surface to correct for sample tilt and x-y piezo coupling, and then corrected line-by-line to the same vertical offset (zero order flattening).

Figure 9, continued

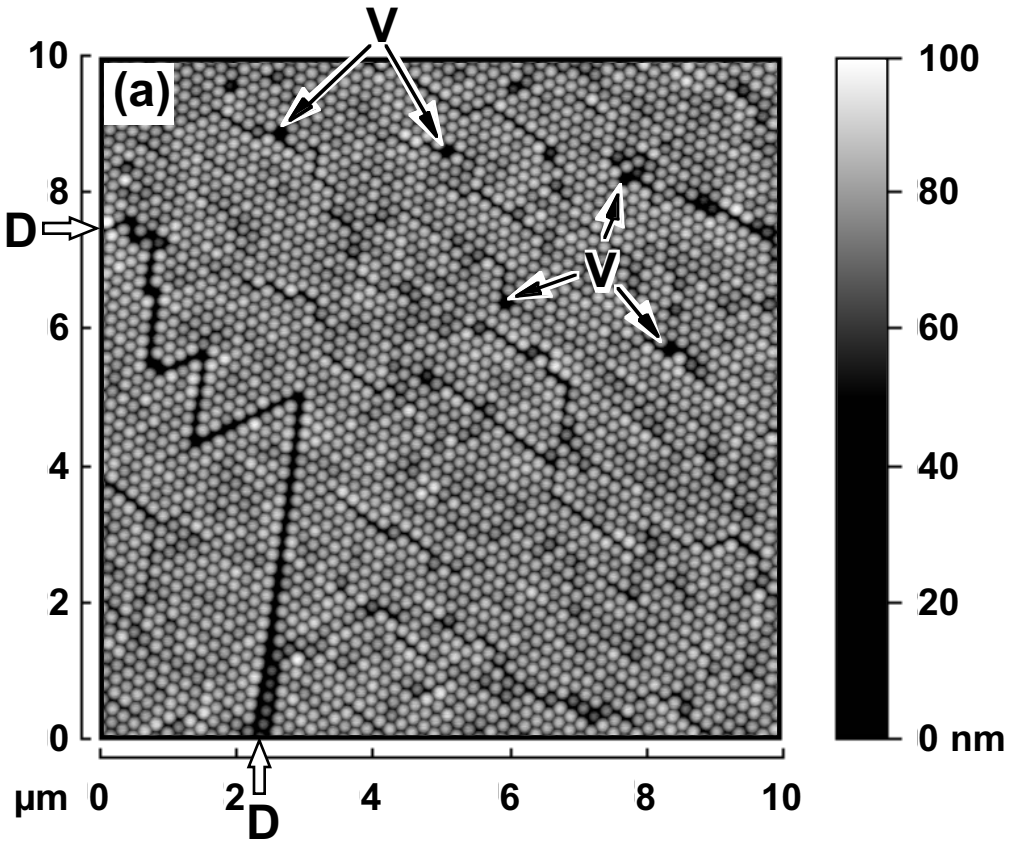

Figure 9, continued

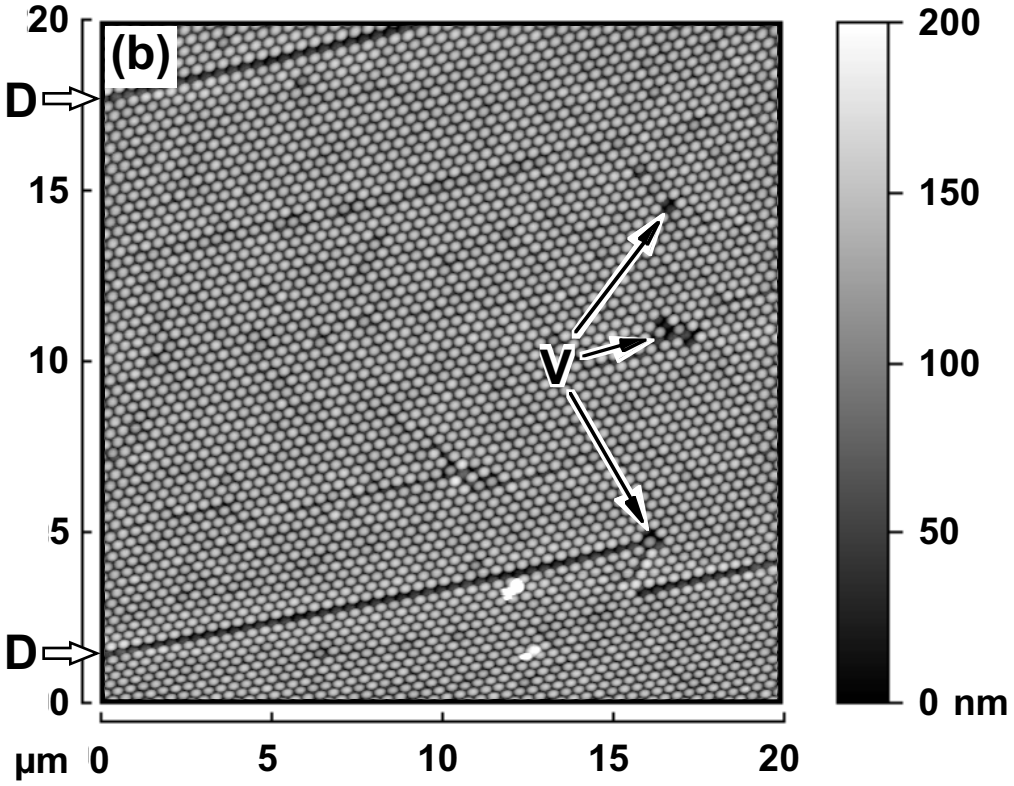

Figure 9, continued

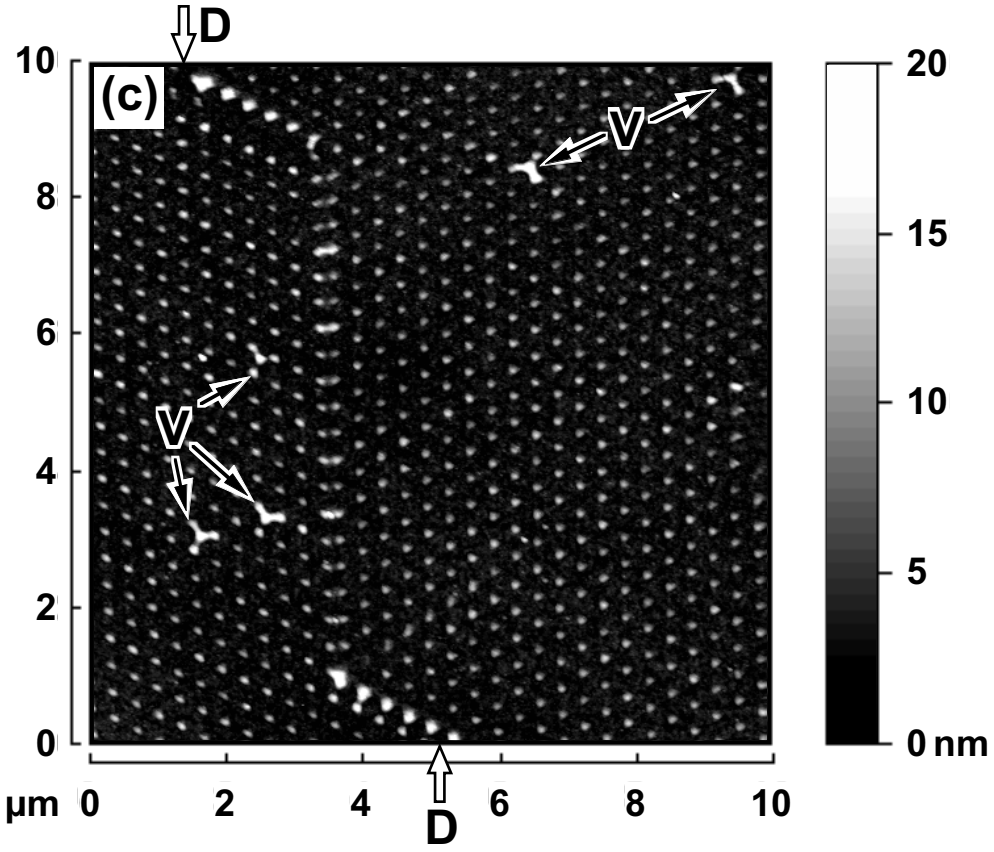

Figure 9, continued

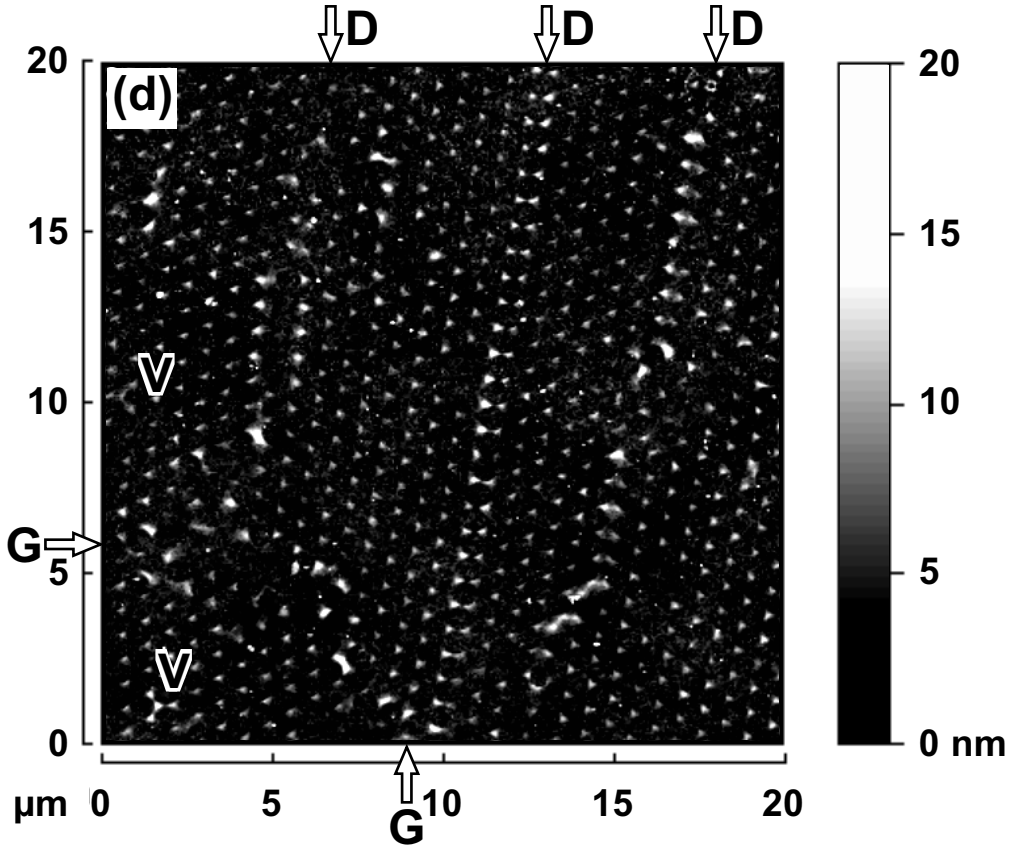

Figure 10. Ni particle cross-sections as obtained by TMAFM. Cross-sections of typical non-defect particles on nanopatterned surfaces prepared using nanospheres of (a) 174 nm, (b) 365 nm, (c) 760 nm, and (d) 1530 nm diameter (D_s). The horizontal lines indicate the cutoff height used in calculating particle sizes and fractional area coverages in each case.

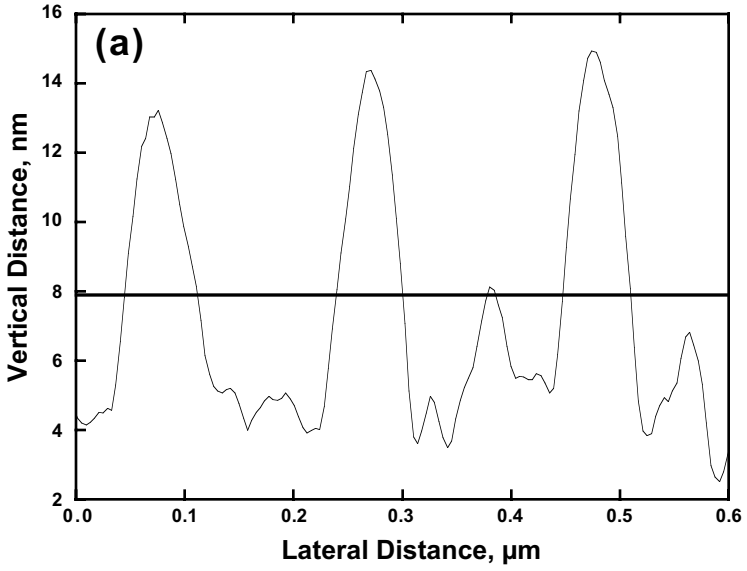

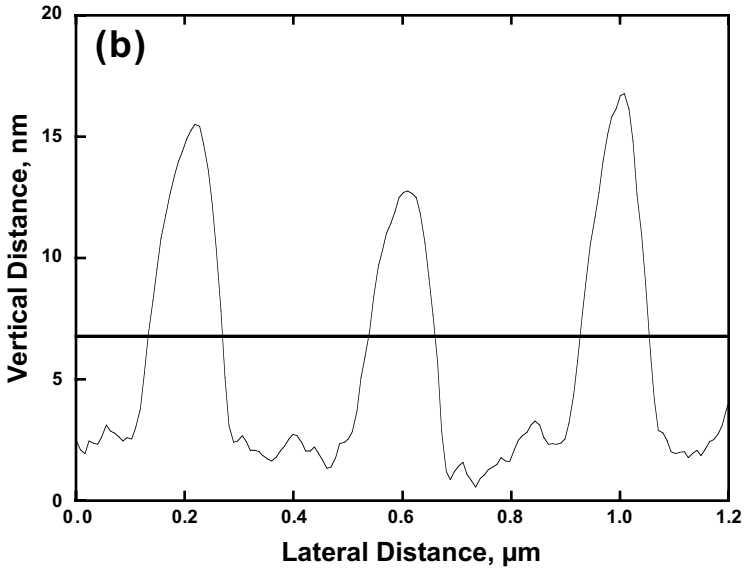

Figure 10, continued

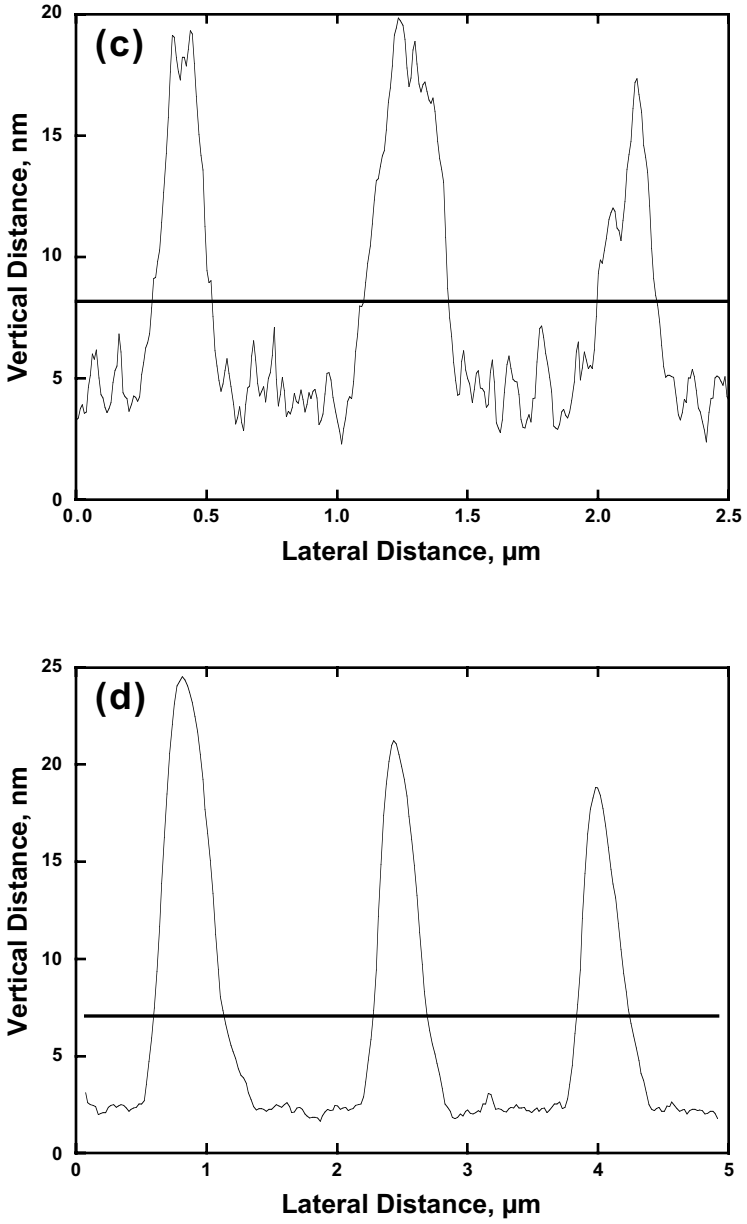

Figure 11. Ni particle size distributions. Effective diameters of particles on nanopatterned electrode surfaces prepared using nanospheres of (a) 174 nm, (b) 365 nm, (c) 760 nm, and (d) 1530 nm diameter (D_S).

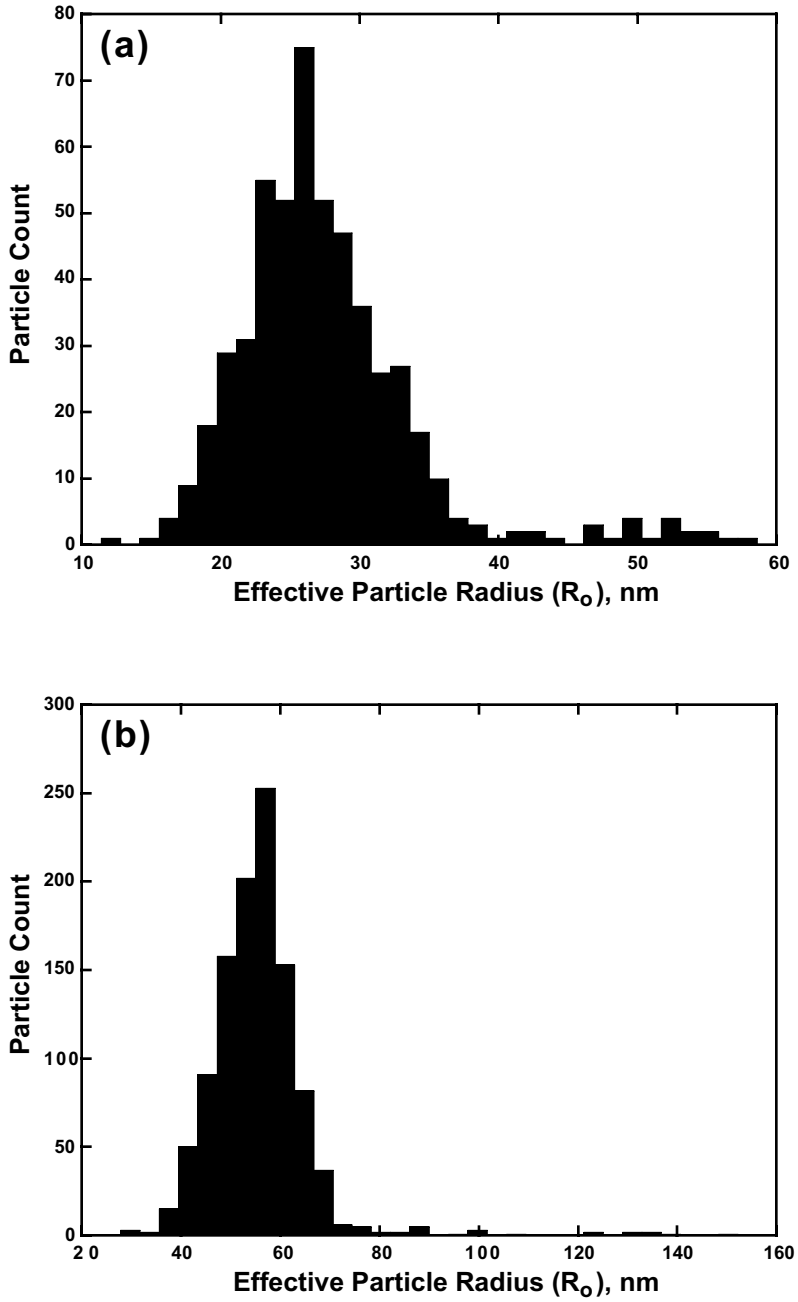

Figure 11, continued

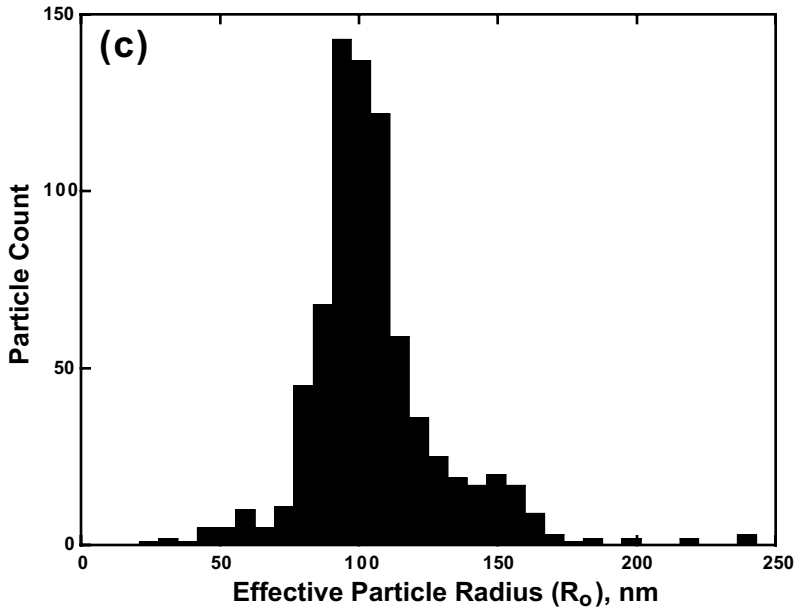

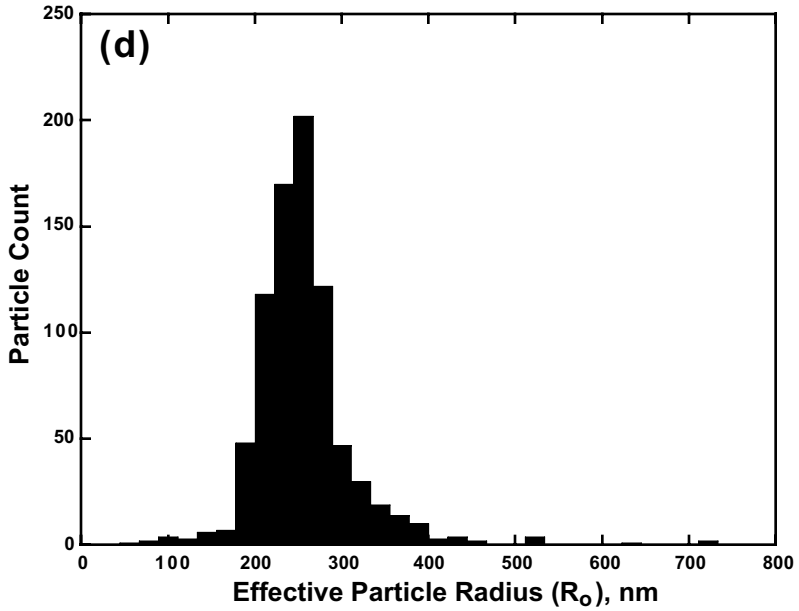

Figure 12. Point vacancy defect particle size distributions. Effective diameters of the largest particle associated with each point vacancy defect found on nanopatterned electrode surfaces prepared using nanospheres of (a) 174 nm, (b) 365 nm, (c) 760 nm, and (d) 1530 nm diameter (D_S).

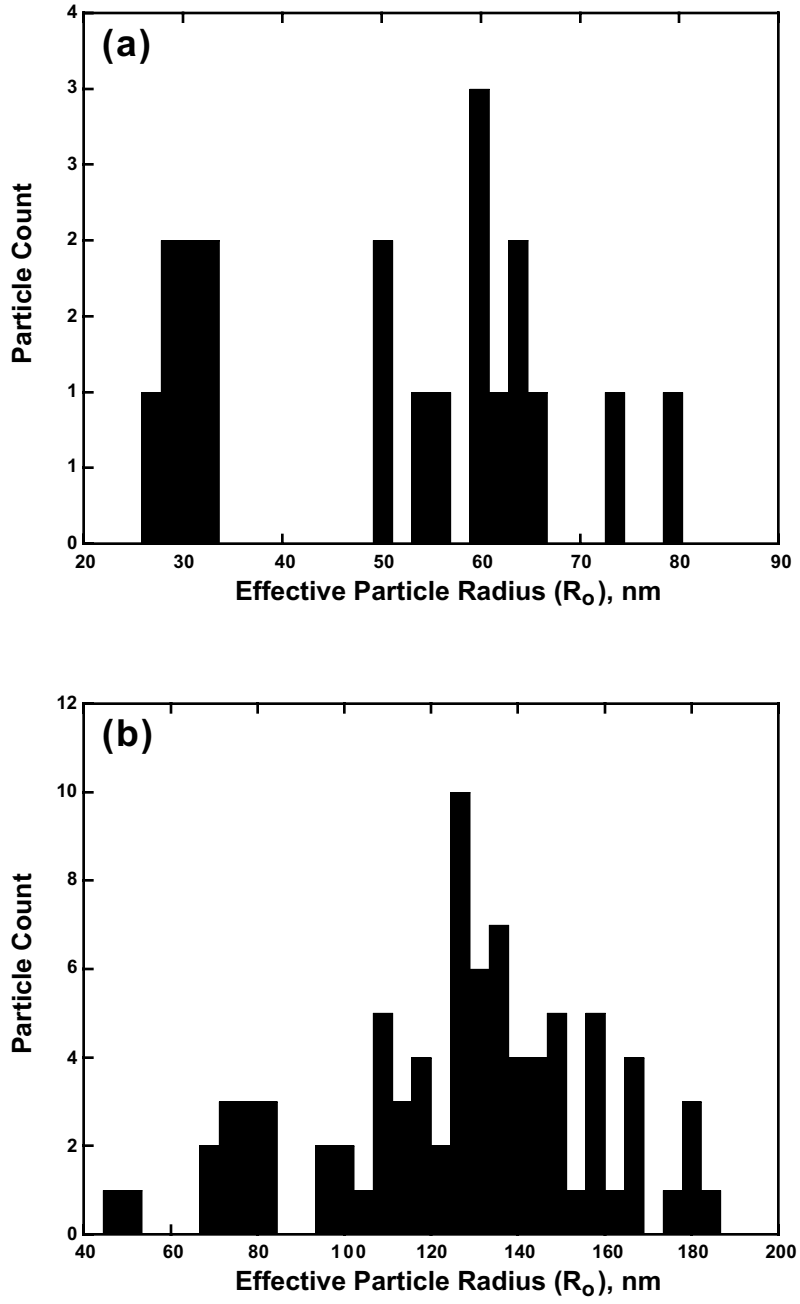

Figure 12, continued

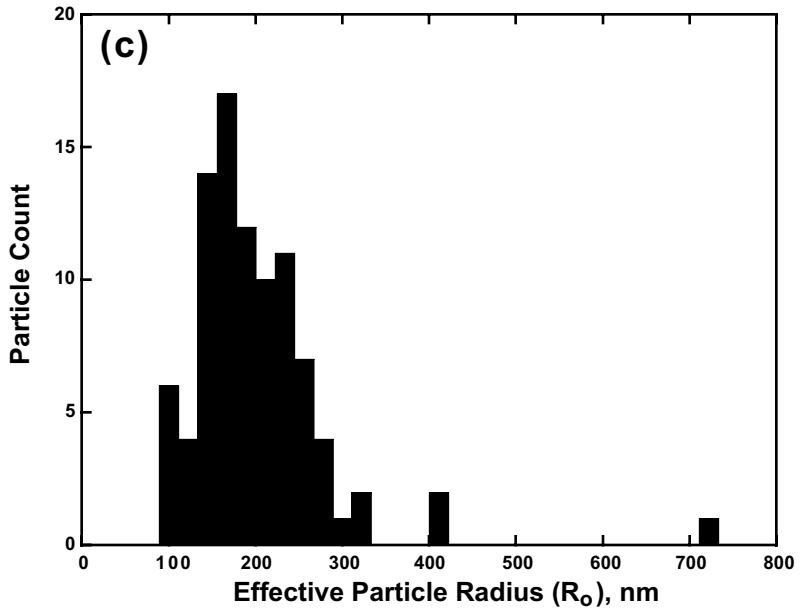

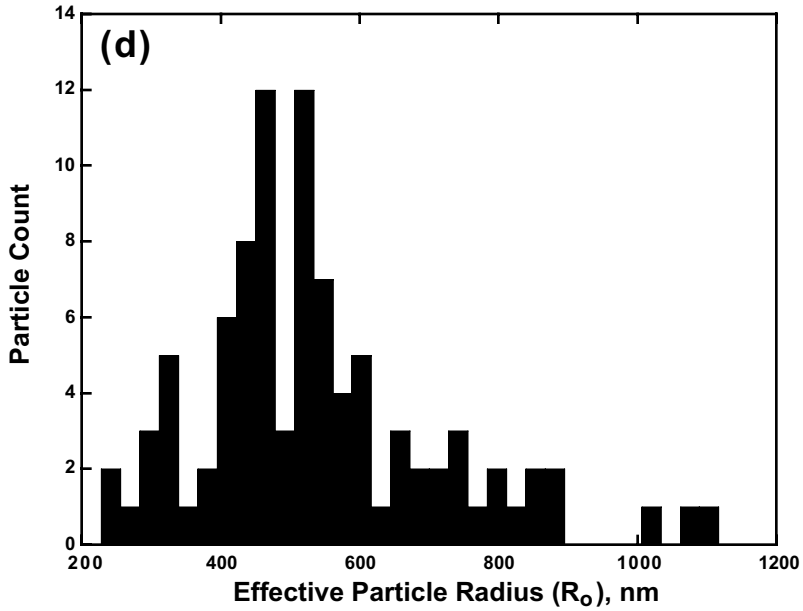

Figure 13. Dislocation defect particle size distributions. Effective diameters of the particles associated with dislocation defects found on nanopatterned electrode surfaces prepared using nanospheres of (a) 174 nm, (b) 365 nm, (c) 760 nm, and (d) 1530 nm diameter (D_S).

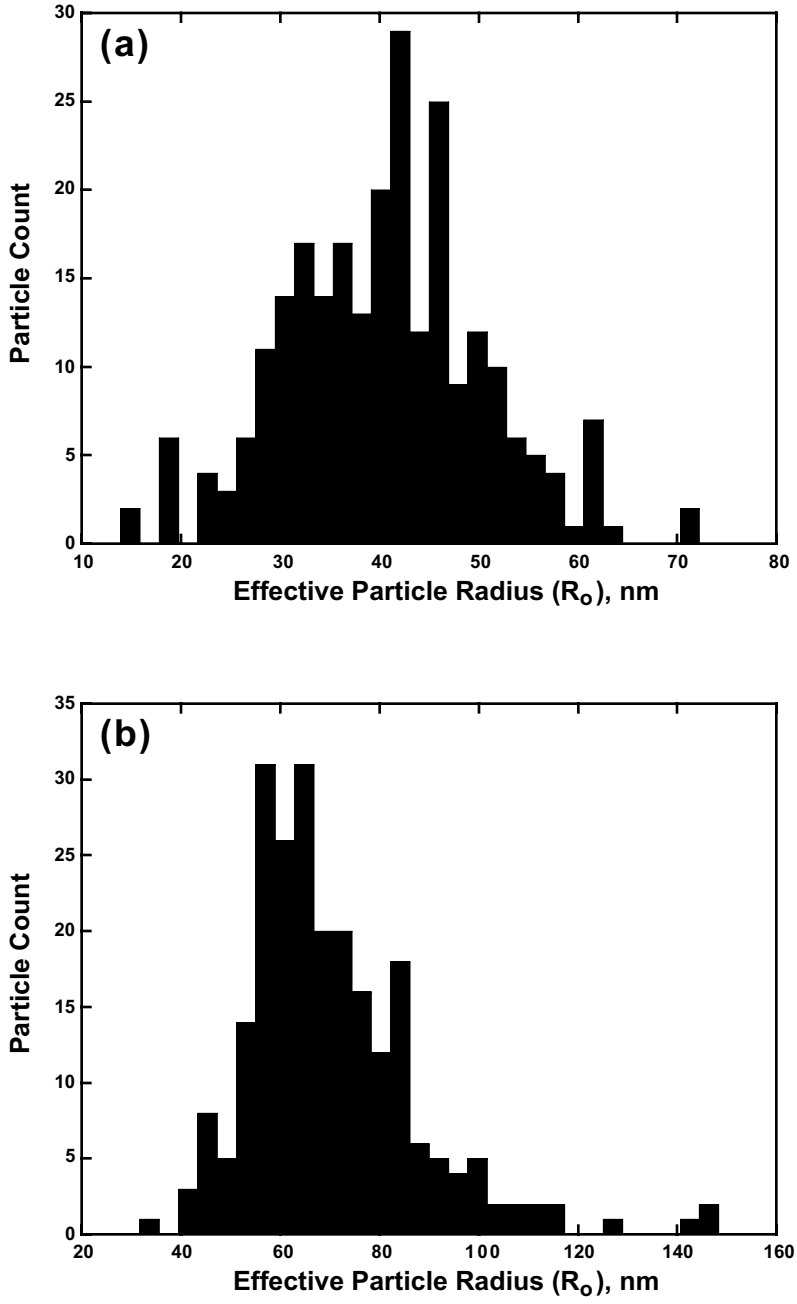

Figure 13, continued

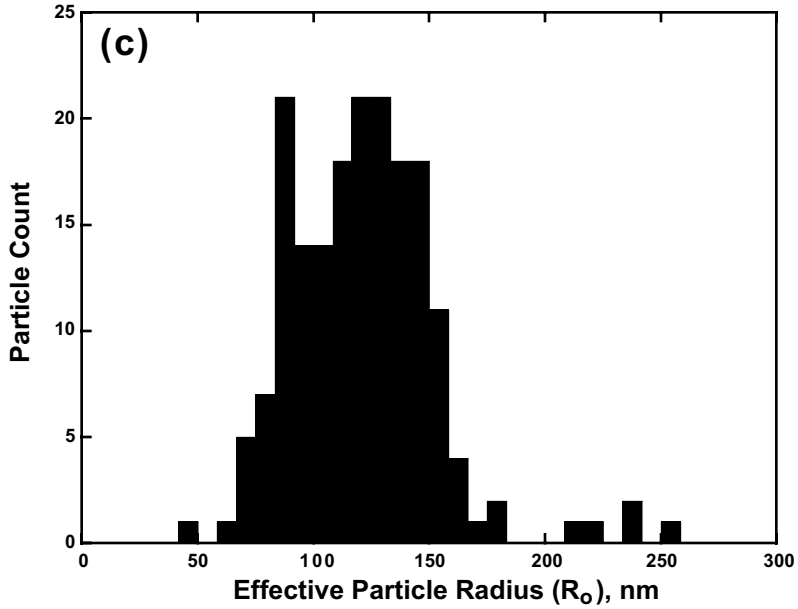

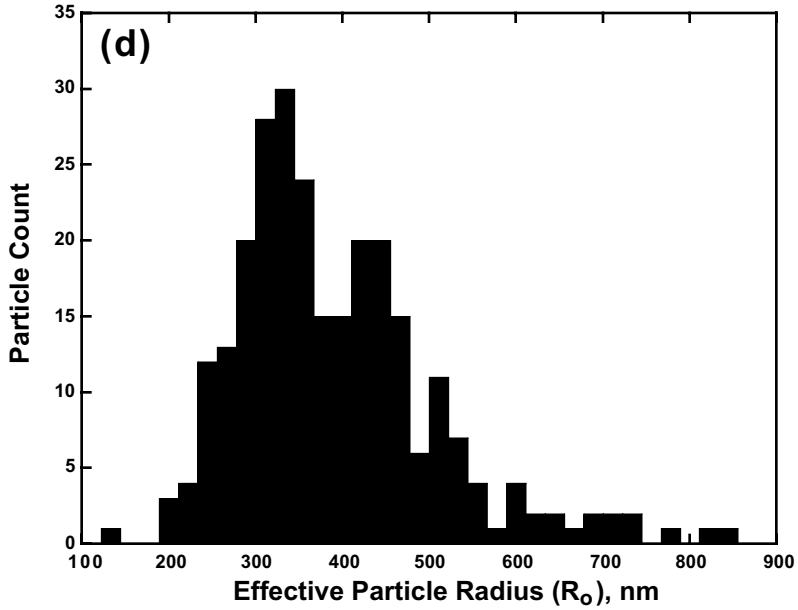

Figure 14. Forward bias dark J-V responses of the electrodes. Grouped by the diameter of the nanospheres (D_s) used in preparing the n-Si/Ni|E electrodes of each set, these are plots of the geometric mean current density obtained at n (Table 9) identically prepared electrodes at applied potential values corrected for series resistance and concentration overpotential losses. The error bars indicate the standard deviation in the current values measured across the n electrodes. Fits to the diode equation (equation 32) are indicated with thin lines, with the corresponding parameters appearing in Table 9. The thicker lines indicate the predictions of the interacting contact model (solid, calculated using equation 27 and Table 1), where applicable, and the independent contact model (dashed, calculated using equation 27 and Table 2) using the experimentally measured input parameters listed in Table 6. Results obtained for: (a) D_s = 174 nm, (b) D_s = 365 nm, (c) D_s = 760 nm, (d) D_s = 1530 nm.

Figure 14, continued

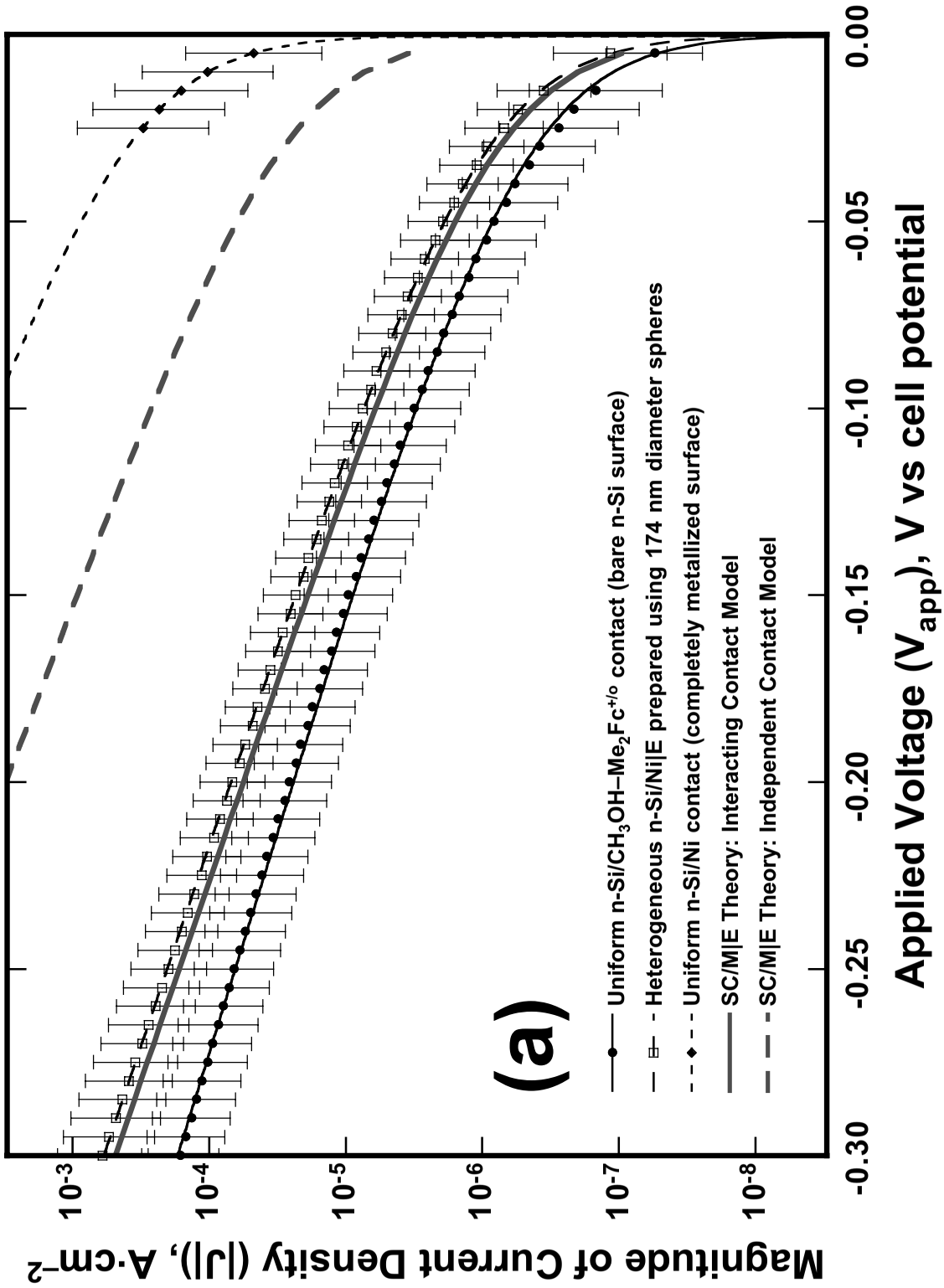

Figure 14, continued

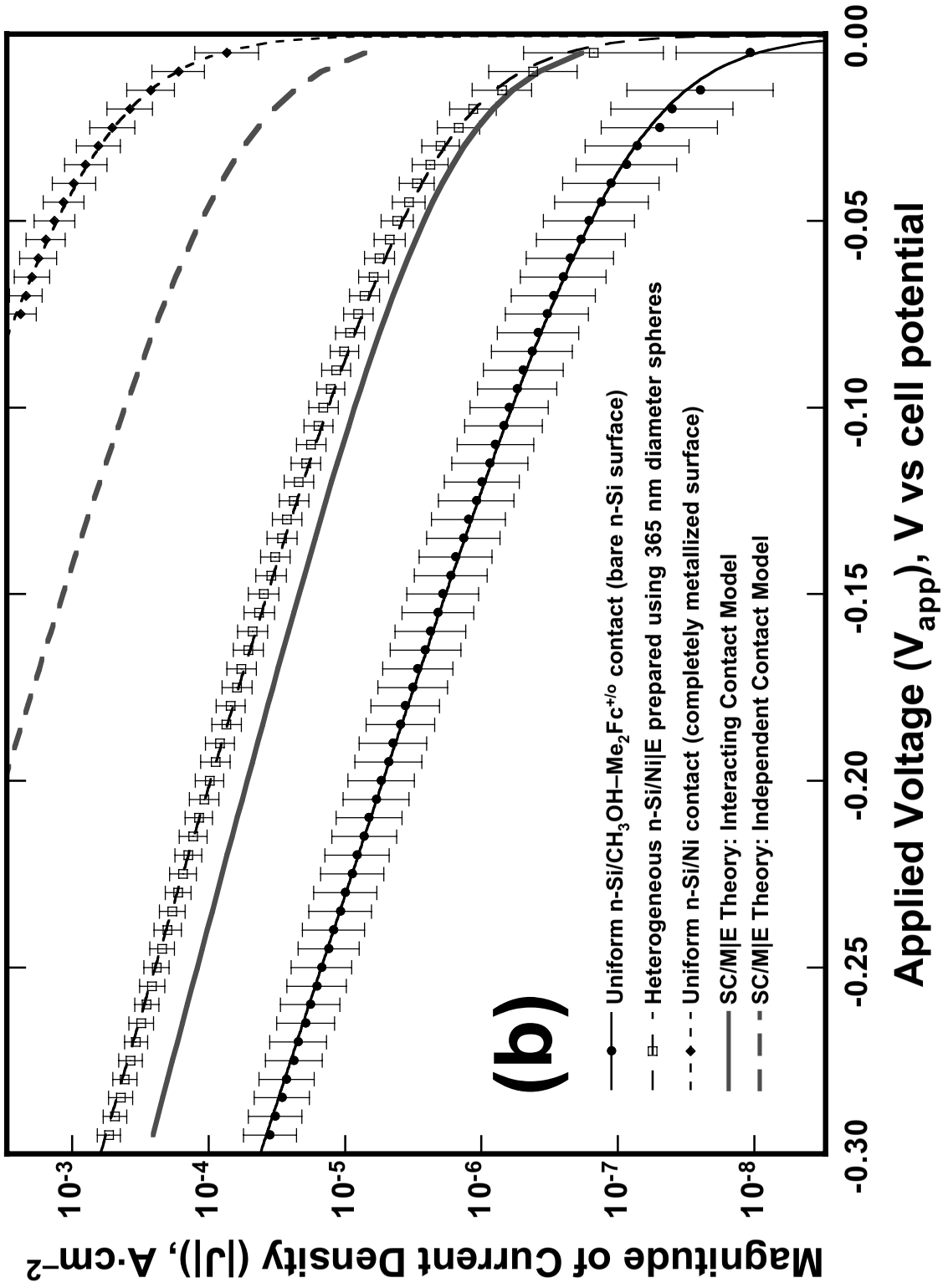

Figure 14, continued

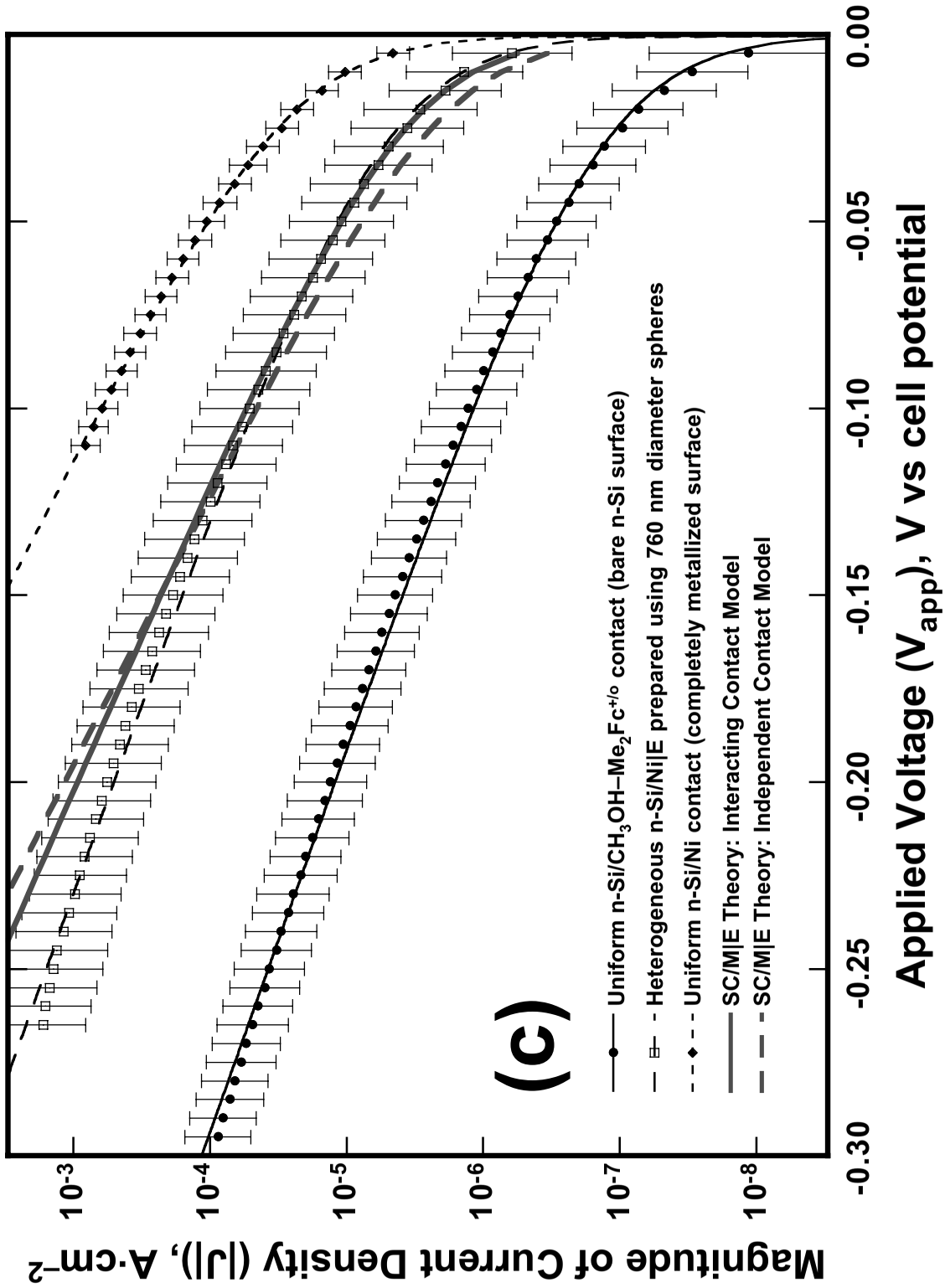

Figure 14, continued

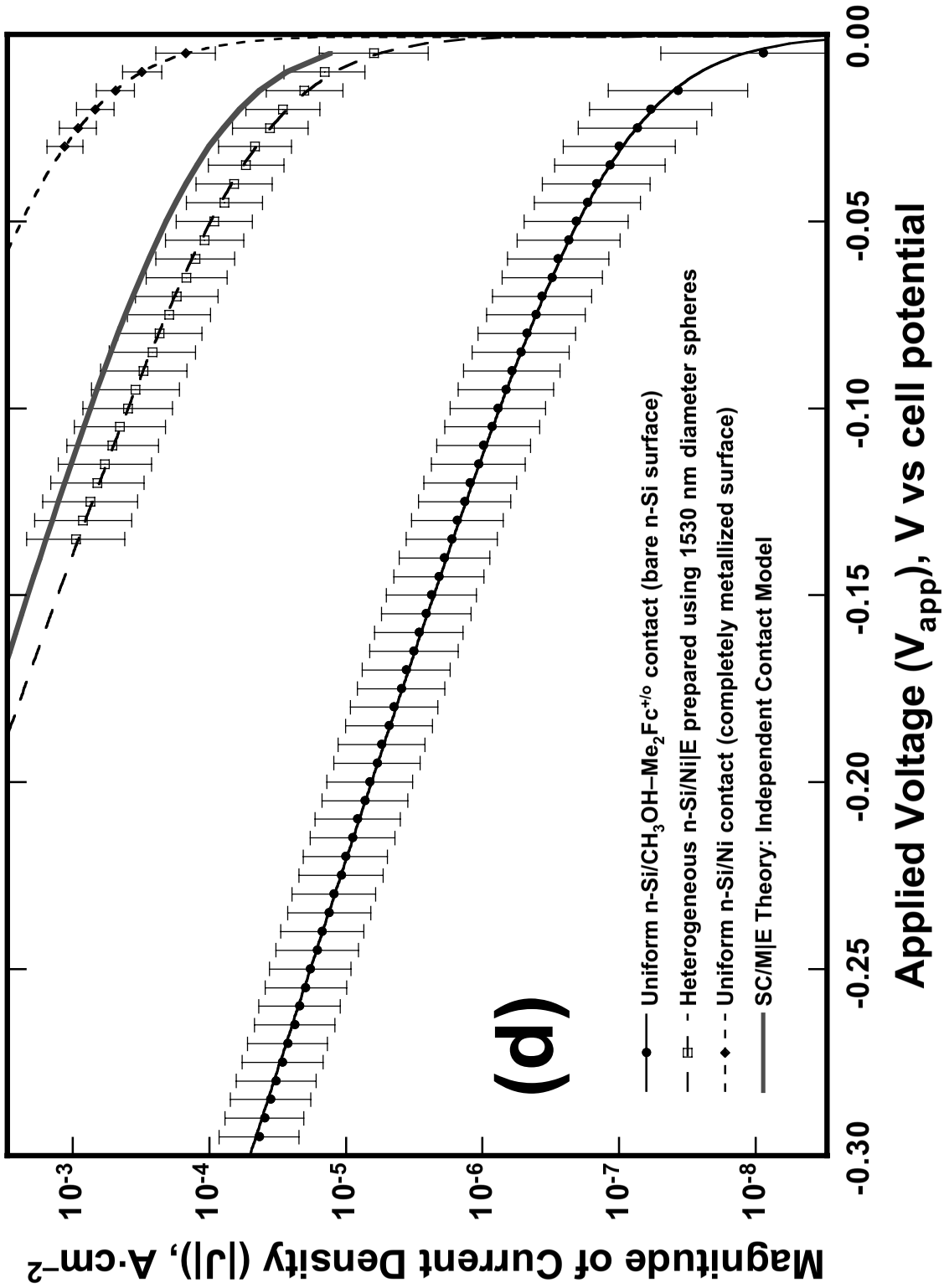

Figure 15. Effect of large defects in nanopattern on dark J-V behavior of *n*-Si/Ni|E electrodes. The dark J-V properties of two electrodes patterned with D_s = 174 nm diameter nanospheres are compared relative to the response of a bare (*n*-Si/E) electrode. One of the two nanopatterned electrodes (filled circles) has a high density of nanopattern defects exposed at its perimeter, and exhibits a disproportionately rapid rise in current at low bias. The other nanopatterned electrode (hollow squares) has a far lower exposed defect density and follows the diode equation well for all bias values. Though the behavior of the two electrodes becomes similar at large biases (see discussion), quantitative analysis of our results was carried out in the low bias region and thus electrodes having significant exposed defect areas had to be eliminated from the analysis.

Figure 15, continued

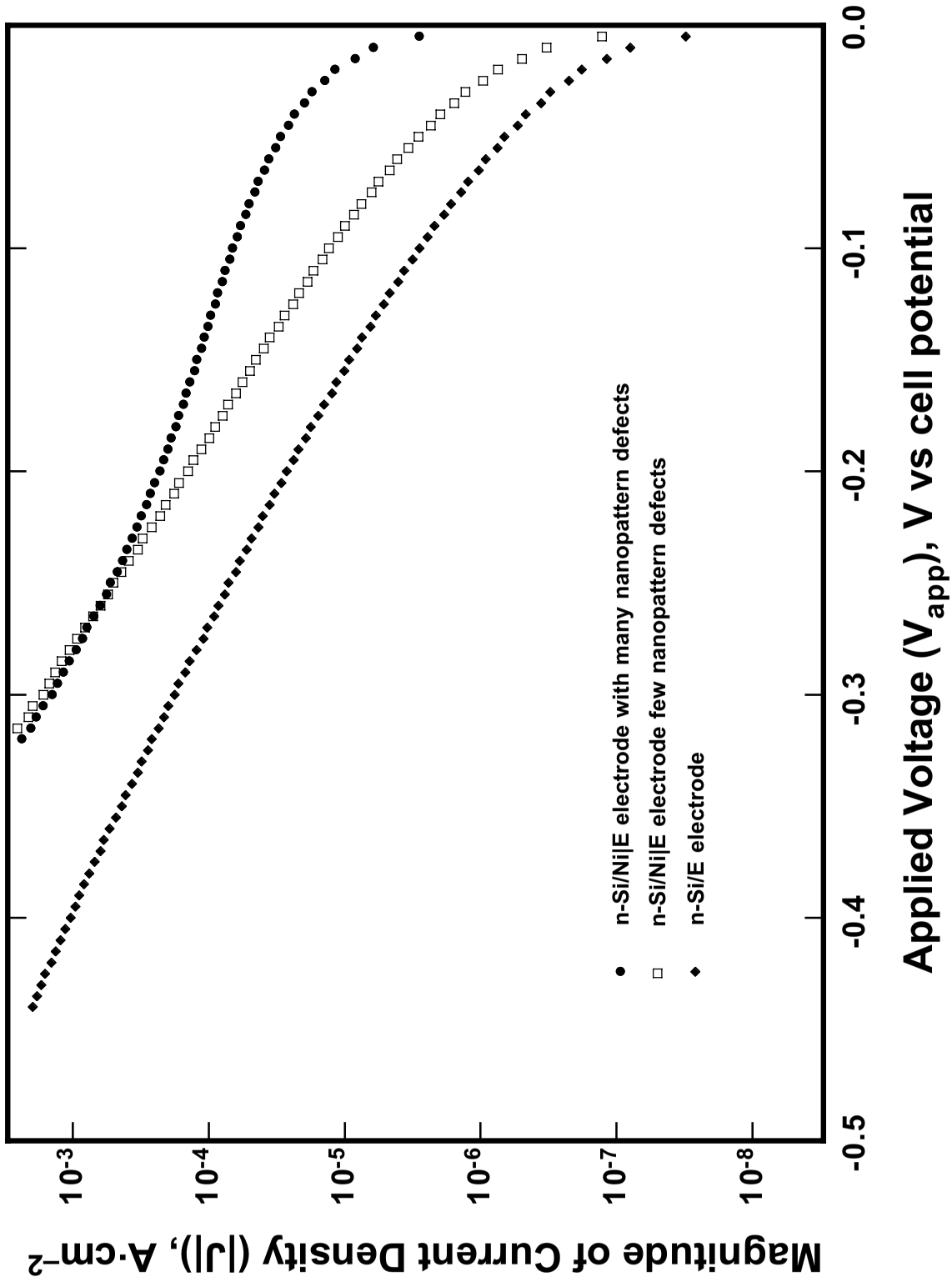

Figure 16. Photoresponses of the electrodes. Grouped by the diameter of the nanospheres (D_S) used in preparing the *n*-Si/Ni|E electrodes of each set, these are plots of the individual photoresponses of the same electrodes studied in Figure 14. The predicted photoresponses obtained from the diode equation (equation 32 modified as specified in text), based on the parameters extracted from the dark responses and tabulated in Table 9, are indicated with thin lines. The thicker lines indicate the predictions of the interacting contact model (solid, calculated on equation 28 and Table 1), where applicable, and the independent contact model (dashed, calculated using equation 28 and Table 2) using the experimentally measured input parameters listed in Table 6. Results obtained for: (a) D_S = 174 nm, (b) D_S = 365 nm, (c) D_S = 760 nm, (d) D_S = 1530 nm.

Figure 16, continued

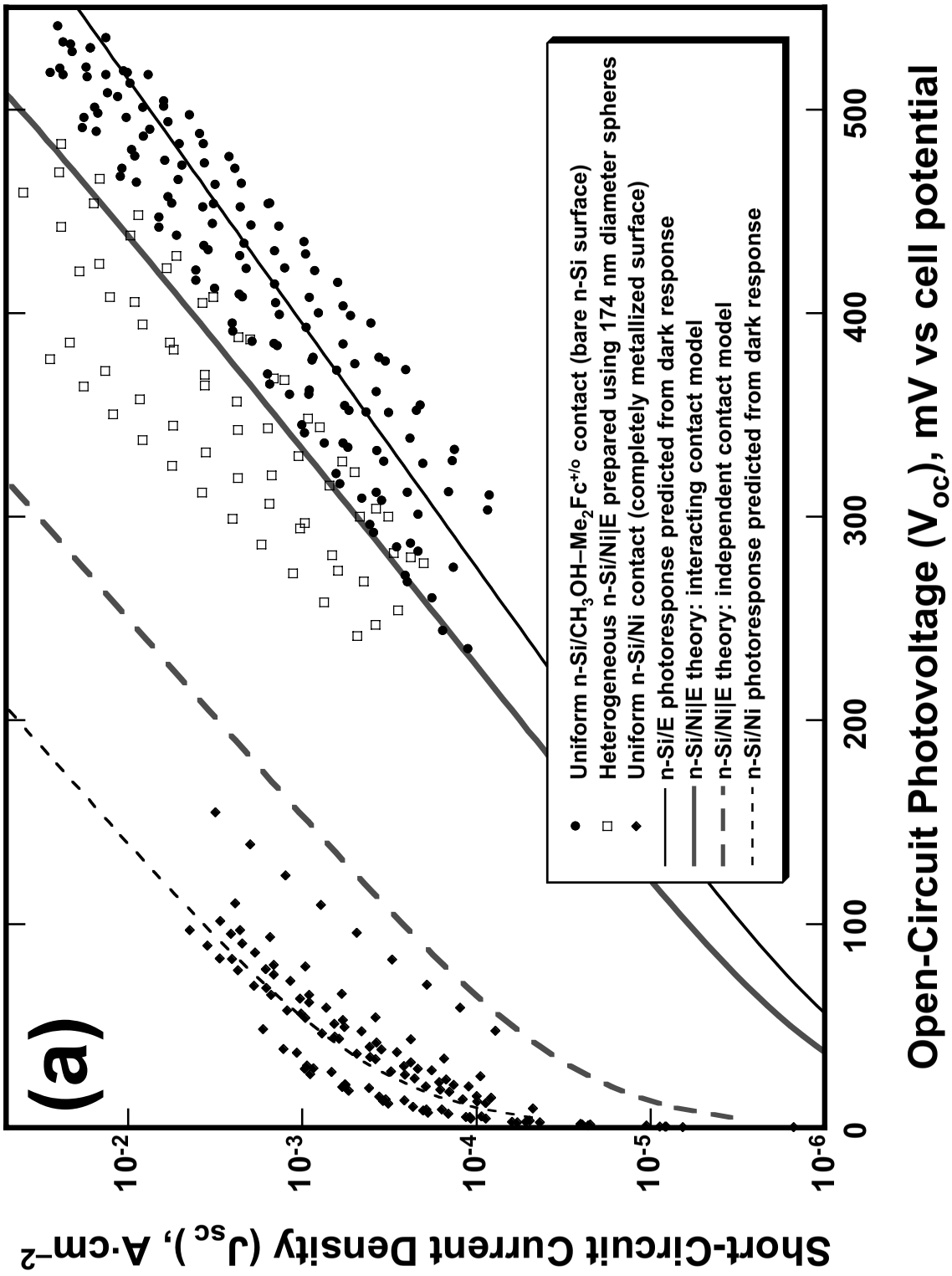

Figure 16, continued

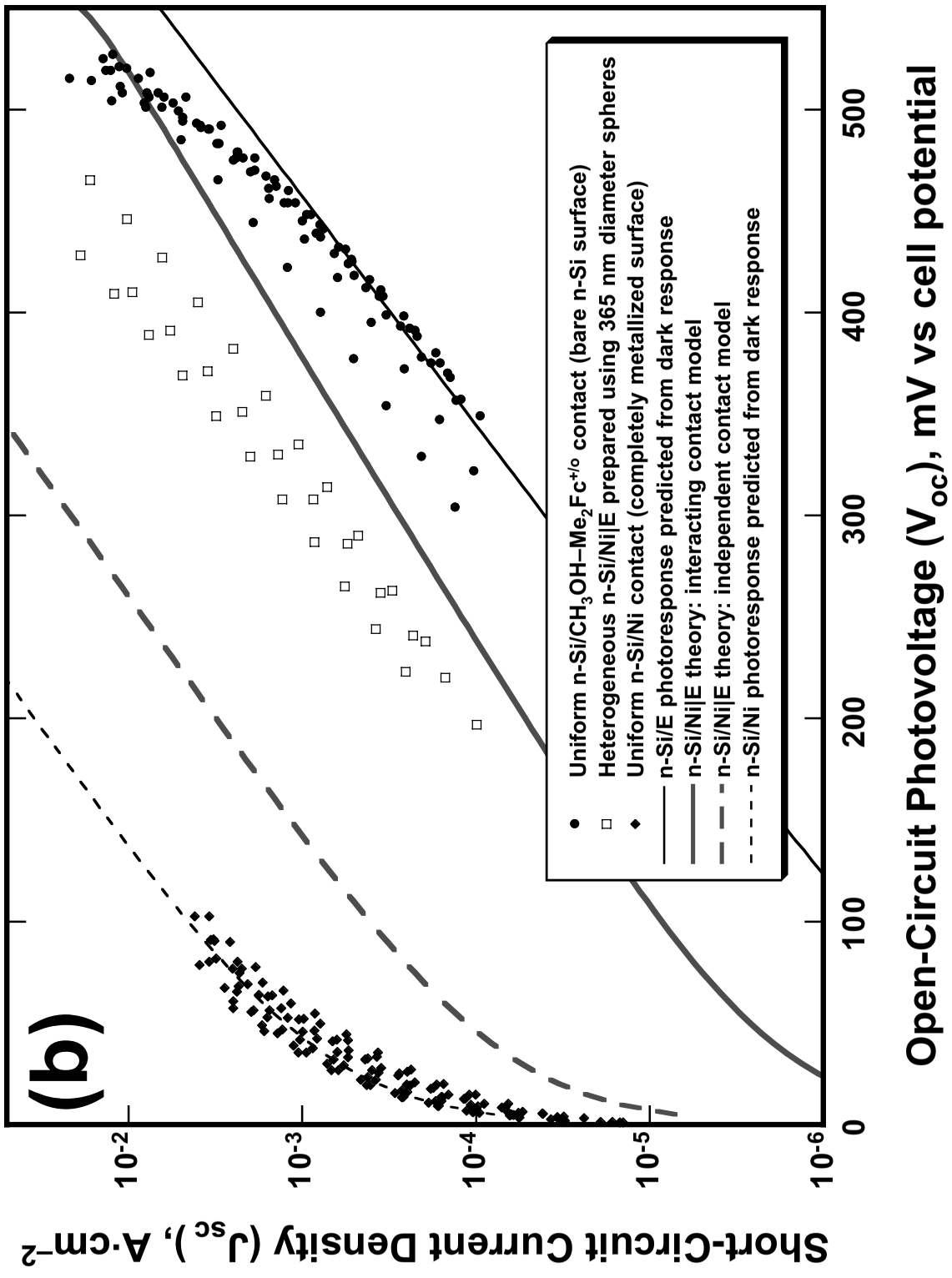

Figure 16, continued

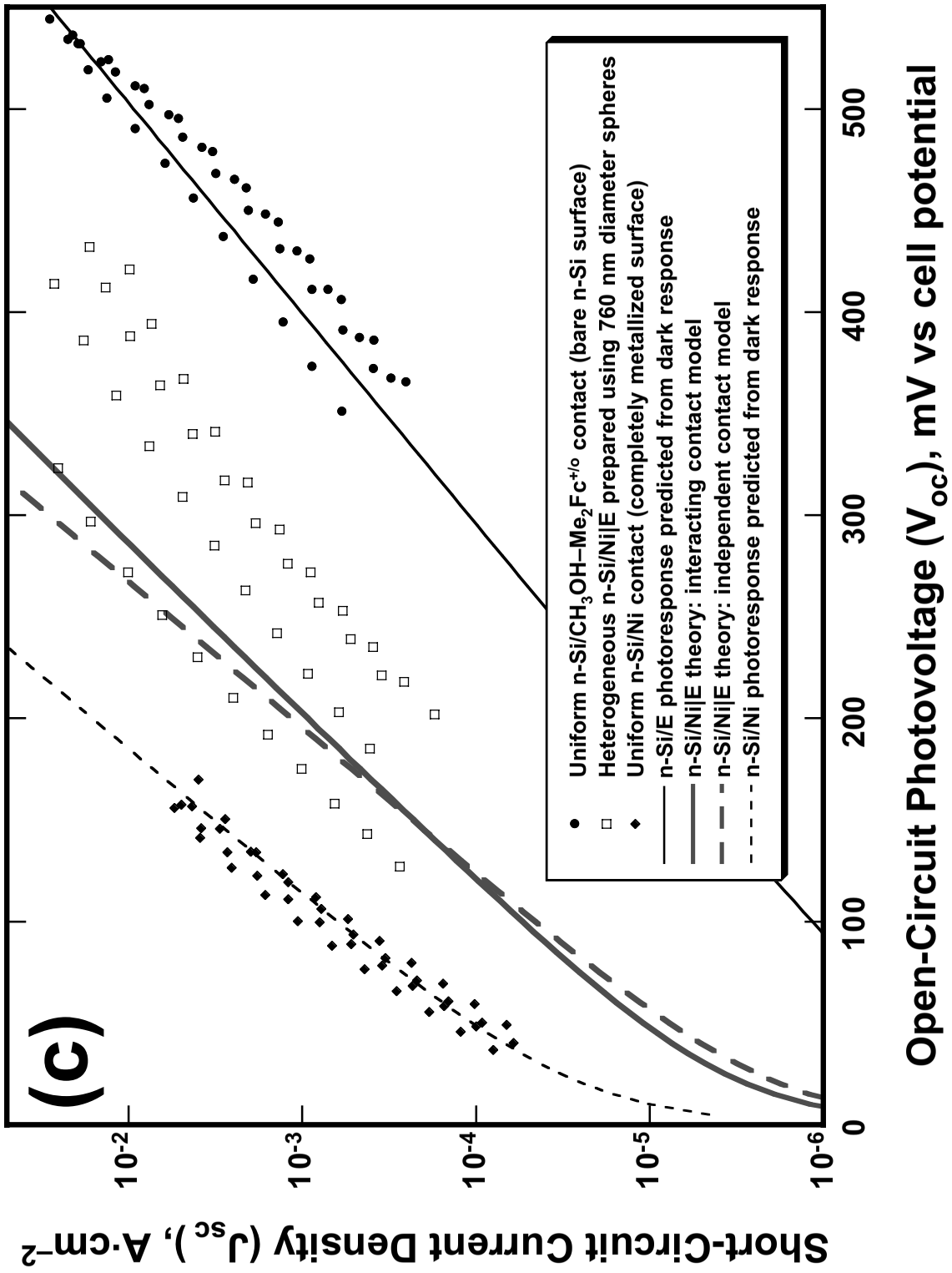

Figure 16, continued

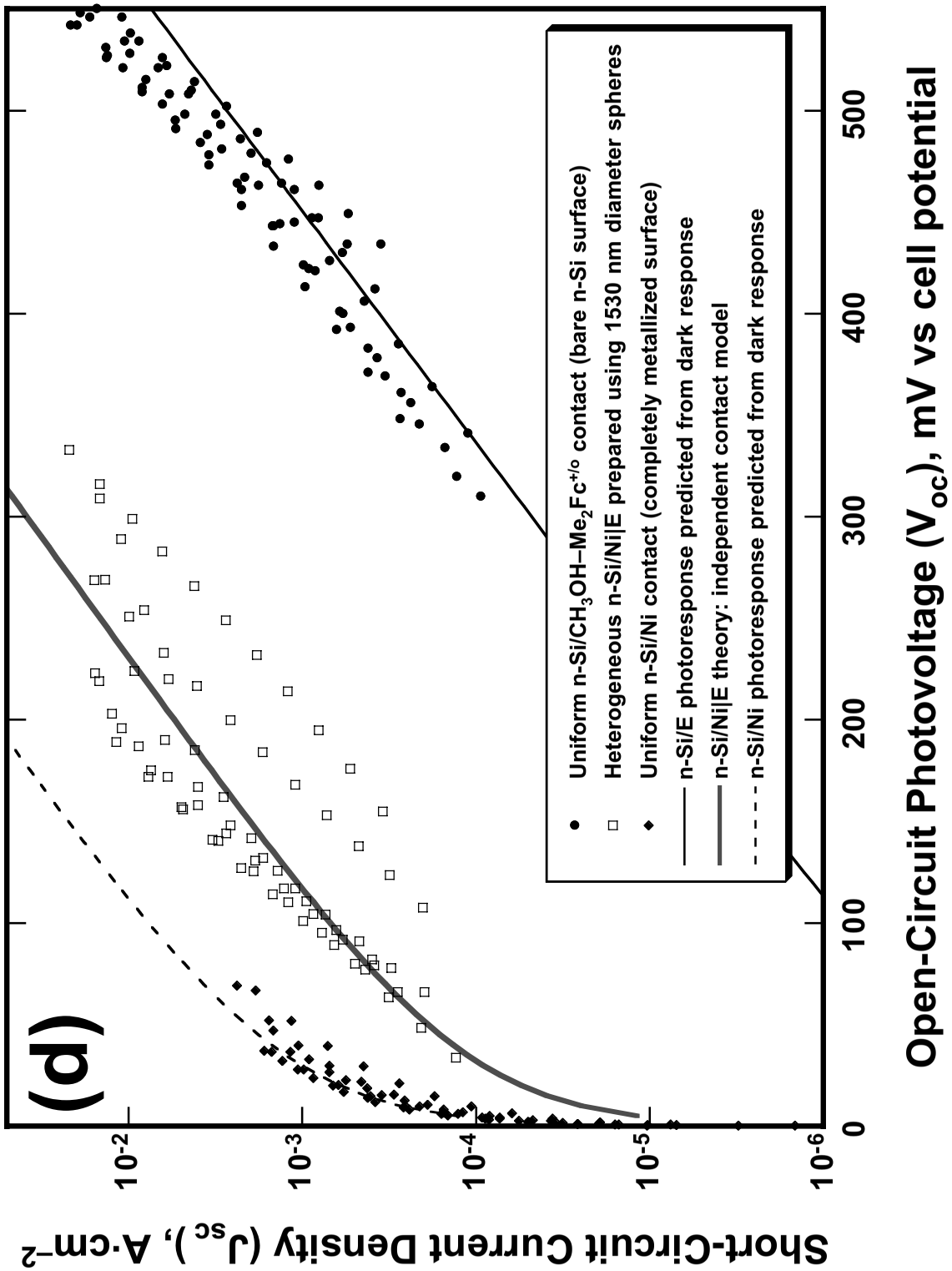

Figure 17. Geometrically expected behavior of single- and double-layer nanosphere lithographic masks. These schematic representations of (a) single-layer and (b) bilayer nanosphere lithographic masks, and the geometrically anticipated nanopatterns (c and d) expected in each case, include a point vacancy defect (arrowed) in the upper left corner. The size of the metal particle resulting from a single point vacancy defect in a single-layer mask is on the order of the nanosphere cross-section, while a much smaller defect arises as a result of a single point defect in a bilayer mask.

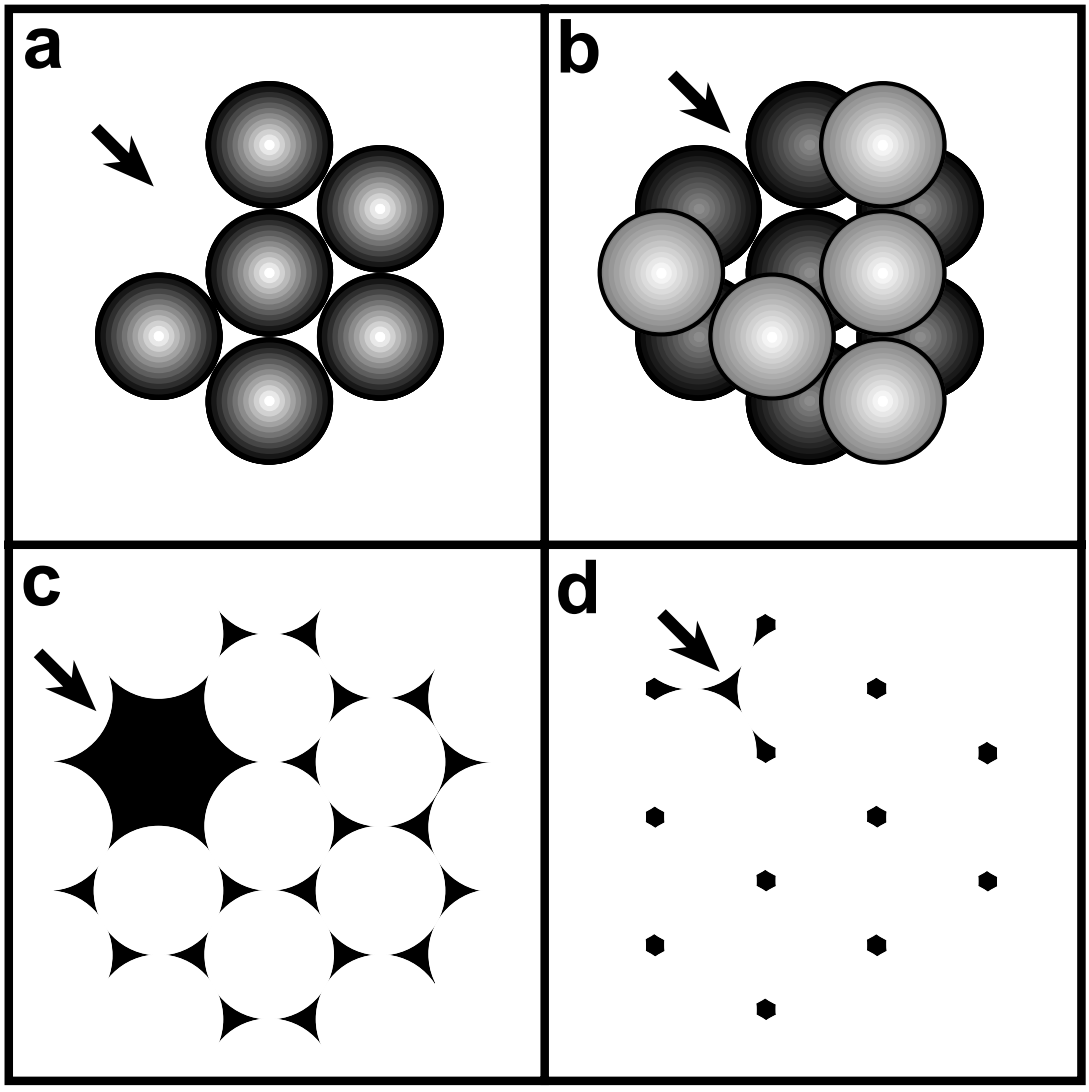

Figure 18. Point dipole model predictions compared with those of the dipole layer model. The potential contour expected to manifest itself along the central axis of the nanoparticles on each *n*-Si/Ni|E surface investigated in this work is calculated subject to the assumptions of the point dipole model (equation 17, solid curve) and the dipole layer model (equation 4, dashed curve). D_S = 174 nm (a), 365 nm (b), 760 nm (c), 1530 nm (d). The point dipole model systematically underestimates the saddle point potential, but the magnitude of the error clearly increases with D_S. In case (d), the point dipole model predicts a saddle potential where the dipole layer model (correctly) anticipates that none will exist. Use of equation 6 allows one to verify that the pinch-off effect is indeed expected to manifest itself, and thus avoid applying the point dipole model where its use would be unwarranted and would lead to unphysical predictions.

Figure 18, continued

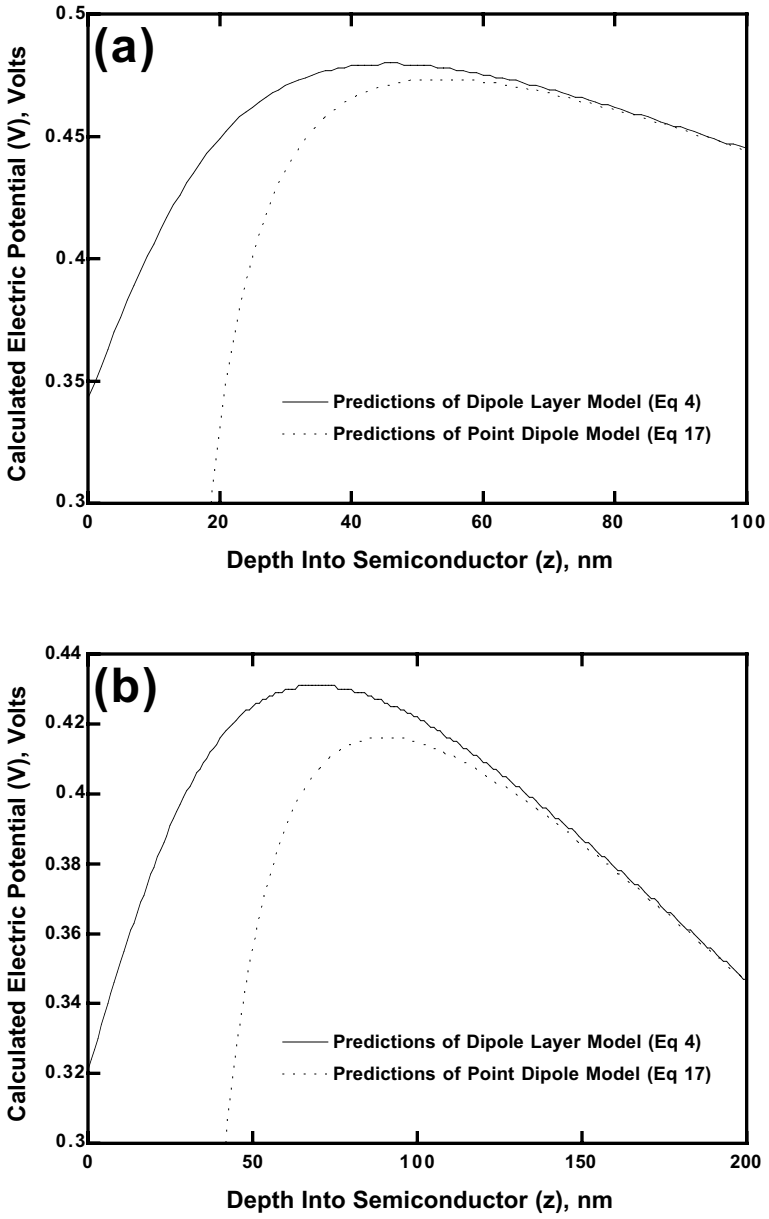

Figure 18, continued

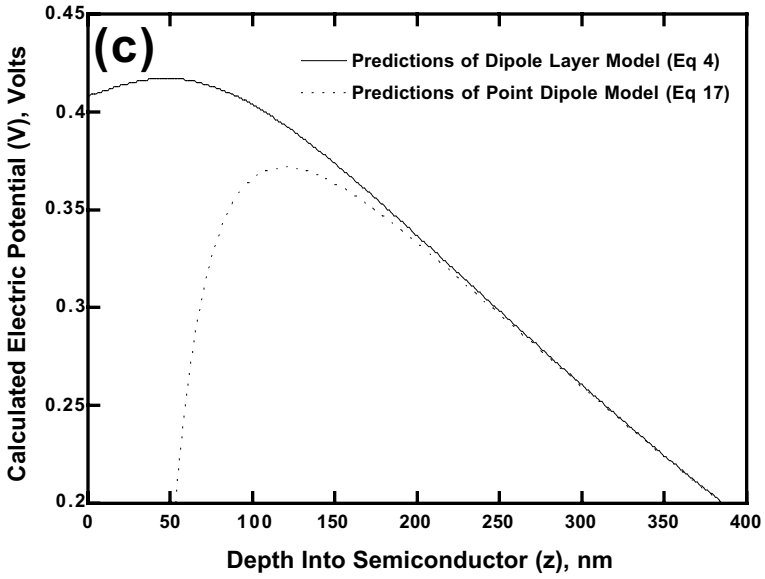

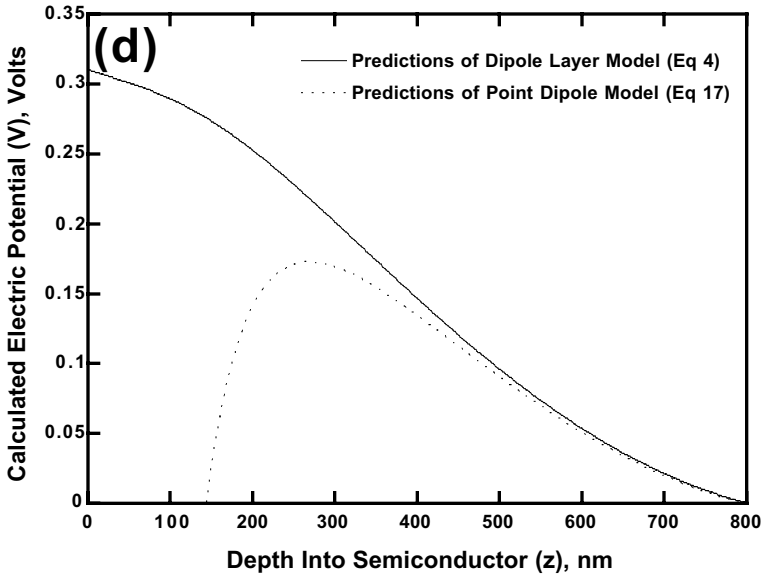

Appendix A: Abbreviations and symbols

NB: Standard abbreviations are used for all SI units

/ = In series with

| = In parallel with

BEEM = Ballistic emission electron microscopy

buffered HF = 36%$_{wt}$ $NH_4F_{(aq)}$ / 7%$_{wt}$ $HF_{(aq)}$ buffer, pH 5.0

CB = Conduction band

CP = Contacting phase (any material in intimate contact with a SC)

Me_2fc^o = 1,1'-dimethylferrocene

Me_2fc^+ = 1,1'-dimethylferrocenium

$Me_2fc^{+/o}$ = 1,1'-dimethylferrocene and 1,1'-dimethylferrocenium

E = Electrolytic or redox solution phase

IL = Interfacial layer

IS = Interfacial state(s)

I-V = Current vs voltage

J-V = Current density vs voltage

loc = Local

M = Metal

SC = Semiconductor

SC/E = Semiconductor/electrolyte contact

SC/M = Semiconductor/metal (Schottky) contact

SC/M|E = SC/M and SC/E contacts in parallel on the same semiconductor surface

SC/M/E = A completely metallized semiconductor immersed in an electrolyte

$SC/M_1|M_2$ = Two different metals in parallel on the same semiconductor surface

TMAFM = TappingMode (intermittent contact) atomic force microscopy

Vac = Local vacuum level

VB = Valence band

Appendix B: Variables and units

A = Diode quality (ideality) factor [dimensionless]

A^{**} = Effective Richardson constant [120 $A \cdot cm^{-2} \cdot K^{-2}$]

A_{dots} = Expected diode quality factor for current passing through a macroscopic metal dot on SC/M|E surface [dimensionless]

A_{ℓ} = Observed diode quality (ideality) factor of SC/E contact [dimensionless]

A_{loc} = Expected local diode quality factor for SC/M|E contact [dimensionless]

A_M = Observed diode quality (ideality) factor of SC/M contact [dimensionless]

D_s = Physical diameter of polystyrene nanospheres [nm]

E_F = Fermi level [eV]

E_g = Band-gap of semiconductor [eV]

F = Faraday constant [96485 $C \cdot mol^{-1}$]

f_{actual} = Actual area fraction of M on nanopatterned surface [dimensionless]

f_{eff} = Effective area fraction of metal dots on SC/M|E surface [dimensionless]

I = Net current [A]

I_{dot} = Net current through a single low barrier height dot [A]

$I_{o,\ dot}$ = Exchange current through a single low-barrier-height dot [A]

J = Current density, current per unit area [$A \cdot cm^{-2}$]

J_o = Equilibrium exchange current density across a heterojunction [$A \cdot cm^{-2}$]

$J_{o,\ bare}$ = Effective exchange current through bare portions of SC/M|E [$A \cdot cm^{-2}$]

$J_{o,\ dots}$ = Effective exchange current through metal dots on SC/M|E [$A \cdot cm^{-2}$]

$J_{o,\ \ell}$ = Observed exchange current density at SC/E electrodes [$A \cdot cm^{-2}$]

J_{bare} = Current density through bare (unmetallized) portions SC/M|E surface, based on total electrode area [$A \cdot cm^{-2}$]

J_{dots} = Current density through metal dots on SC/M|E surface, based on total electrode area [$A \cdot cm^{-2}$]

$J_{lim,\ a}$ = Mass-transport limited anodic current density [$A \cdot cm^{-2}$]

$J_{lim,\ c}$ = Mass-transport limited cathodic current density [$A \cdot cm^{-2}$]

$J_{nanopatterned}$ = Total net current density through SC/M|E electrode [$A \cdot cm^{-2}$]

J_{ph} = Photogenerated current density [$A \cdot cm^{-2}$]

J_{sc} = Short-circuit current density [$A \cdot cm^{-2}$]

k = Boltzmann constant [1.38065×10^{-23} $J \cdot K^{-1}$]

n = Number of electrons transferred in a single electron transfer reaction

n = Number of replicate samples

N_C = Effective density of states in semiconductor conduction band [cm^{-3}]

N_D = Donor impurity (dopant) concentration in *n*-type semiconductor [cm^{-3}]

n_i = Intrinsic carrier concentration in undoped semiconductor [cm^{-3}]

N_X = Majority carrier dopant concentration in semiconductor [cm^{-3}]

q = Elementary charge [1.602×10^{-19} Coulombs]

R = Universal gas constant [8.31451 $J \cdot mol^{-1} \cdot K^{-1}$]

R_o = Radius of low contact potential region on semiconductor surface [nm]

R_s = Series resistance between working and reference electrodes [Ω]

s = Side length of a nanosphere bilayer crystal (assumed square) [μm]

S = Exposed surface area [cm^2]

S_{eff} = Effective area of a single metal dot on SC/M|E surface [cm^2]

T = Absolute temperature [K]

U_{bb} = Band bending in semiconductor that would be observed behind a macroscopic SC/E region identical to that found on SC/M|E [V]

U_{bi} = Built-in potential ("band bending" at zero bias) [V]

U_{inv} = Surface potential at which surface lattice atoms of semiconductor begin to ionize [V]

U_s = Surface potential (electric potential difference between semiconductor bulk and local semiconductor surface) [V]

V_{app} = Electrochemical potential of electrons in bulk SC vs cell potential [V]

qV_c = Contact potential (work function differential across interface) [eV]

qV_n = Energy offset between CB minimum and E_F in semiconductor bulk [eV]

$V_{nominal}$ = Actual electrochemical potential difference measured between the working and reference electrodes of an electrochemical cell [V]

V_{oc} = Open-circuit voltage [V]

W = Depletion width for a homogeneous lateral contact [nm]

W_{max} = Depletion width at which surface lattice atoms of semiconductor begin to ionize [V]

x, y = Position on semiconductor surface, Cartesian (see Figure 4a) [nm]

x_1, y_1 = Cartesian variables of integration in equation 2 [nm]

z = Depth into semiconductor (see Figure 4) [nm]

χ = Electron affinity [eV]

δ = Local perturbation in surface potential [V]

Δ = Lateral surface potential difference at $SC/CP_1|CP_2$ interface [V]

ε = Dielectric permittivity [$C \cdot V^{-1} \cdot m^{-1}$]

ε_s = Dielectric permittivity of silicon [1.05×10^{-12} $C \cdot V^{-1} \cdot m^{-1}$]

ϕ = Work function [eV]

Φ_B = Effective barrier height at SC/M or SC/E junction [V]

Φ_{eff} = Effective local barrier height at a semiconductor heterojunction [V]

Φ_{obs} = Observed effective barrier height at a semiconductor heterojunction [V]

$\Phi_{B,\,M}$ = (Effective) barrier height at SC/M junction [V]

$\Phi_{B,\,patch}$ = Barrier height of low contact potential region on $SC/CP_1/CP_2$ [V]

Φ_B^o = Barrier height of high contact potential region on $SC/CP_1/CP_2$ [V]

Φ_B^* = Barrier height equivalent at strong inversion limit [V]

Γ = Space charge parameter (see Table 1) [dimensionless]

γ = Region parameter (see Table 1) [$V^{1/3}$ $m^{2/3}$]

η = Debye parameter (see Table 1) [$cm^2 \cdot V^{-1}$]

η_{conc} = Concentration overpotential at an electrode [V]

π = 3.141593

ρ = Radial distance from center of low barrier height disc on cylindrically symmetric SC/M|E surface (See Figure 4) [nm]

ρ_1 = Cylindrical variable of integration in equation 4 [nm]

$\rho_{dislocation}$ = Number density of metal dots associated with dislocations [cm^{-2}]

ρ_{dots} = Number density of metal dots on nanopatterned surface [cm^{-2}]

θ = Cylindrical angle in polar coordinate system (see Figure 4) [radians]

θ_1 = Cylindrical variable of integration in equation 4 [radians]

Appendix C: Sign conventions and reference levels

1) Electrochemical potentials (V) are measured relative to that of the bulk contacting medium, and become more positive as the potential energy of a species increases. Voltmeters measure the inverse of the difference in the electrochemical potential of electrons across their contacts, and thus a positive bias indicates a desire of electrons to flow from the bias point to the bulk of the contacting medium.
2) *Electric* potentials (U) are measured relative to the electric potential in the bulk of the semiconductor under no applied bias, and become more *negative* as the potential energy of a positive point charge increases. The dichotomy of symbols serves to underline the distinction between electric and electrochemical potentials, a common cause of confusion in both electrochemistry and solid-state physics.
3) Positive currents correspond to the flow of *electrons* from the contacting phase into the semiconductor *through the contact interface*. The spontaneous flow of *electrons* is from regions of more positive potential to regions of more negative potential. The potential energy of an electron *increases* as its energy becomes more positive, and thus electrons seek low energy regions. Holes behave just the opposite, and seek high energy regions. (It is useful to think of holes as "bubbles" when considering how they will behave in response to a band bending diagram.)

Appendix D: Mathematical derivations

Conversion of equation 2 into cylindrical coordinates and subsequent simplification to yield equation 4

The coordinate transformation of equation 2 into cylindrical coordinates begins with the standard variable substitutions:

$$\begin{aligned} x &= \rho\cos\theta \\ y &= \rho\sin\theta \\ x_1 &= \rho_1\cos\theta_1 \\ y_1 &= \rho_1\sin\theta_1 \\ dx_1dy_1 &= \rho_1 d\rho_1 d\theta_1 \end{aligned}$$

$$U(x, y, z) = U_{bb}\left(1 - \frac{z}{W}\right)^2 + \int\int \frac{\delta(x_1, y_1)}{2\pi} \frac{z}{\left[z^2 + (x_1 - x)^2 + (y_1 - y)^2\right]^{3/2}}\, dx_1\, dy_1 \quad \Rightarrow$$

$$U(\rho, \theta, z) = U_{bb}\left(1 - \frac{z}{W}\right)^2 + \int\int \frac{\delta(\rho_1, \theta_1)}{2\pi} \frac{z}{\left[z^2 + (\rho_1\cos\theta_1 - \rho\cos\theta)^2 + (\rho_1\sin\theta_1 - \rho\sin\theta)^2\right]^{3/2}}\, \rho_1\, d\rho_1\, d\theta_1$$

A portion of the integrand's denominator may be simplified by combining terms:

$$\begin{aligned} &(\rho_1\cos\theta_1 - \rho\cos\theta)^2 + (\rho_1\sin\theta_1 - \rho\sin\theta)^2 = \\ &\quad \rho_1^2\cos^2\theta_1 - 2\rho_1\rho\cos\theta_1\cos\theta + \rho^2\cos^2\theta + \rho_1^2\sin^2\theta_1 - 2\rho_1\rho\sin\theta_1\sin\theta + \rho^2\sin^2\theta = \\ &\quad \rho_1^2(\cos^2\theta_1 + \sin^2\theta_1) + \rho^2(\cos^2\theta + \sin^2\theta) - 2\rho_1\rho(\cos\theta_1\cos\theta + \sin\theta_1\sin\theta) \end{aligned}$$

and then applying the following trigonometric identities:

$$\cos^2 A + \sin^2 A = 1$$

$$\cos A\cos B = \frac{1}{2}\cos(A - B) + \frac{1}{2}\cos(A + B)$$

$$\sin A\sin B = \frac{1}{2}\cos(A - B) - \frac{1}{2}\cos(A + B)$$

The simplification then proceeds to give

$$\rho_1^2(\cos^2\theta_1 + \sin^2\theta_1) + \rho^2(\cos^2\theta + \sin^2\theta) - 2\rho_1\rho(\cos\theta_1\cos\theta + \sin\theta_1\sin\theta) =$$

$$\rho_1^2(1) + \rho^2(1) - 2\rho_1\rho\left(\frac{1}{2}\cos(\theta_1-\theta) + \frac{1}{2}\cos(\theta_1+\theta) + \frac{1}{2}\cos(\theta_1-\theta) - \frac{1}{2}\cos(\theta_1+\theta)\right) =$$

$$\rho_1^2 + \rho^2 - 2\rho_1\rho\big(\cos(\theta_1 - \theta)\big)$$

such that

$$U(\rho,\theta,z) = U_{bb}\left(1 - \frac{z}{W}\right)^2 + \int\int \frac{\delta(\rho_1,\theta_1)}{2\pi} \frac{z}{\left[z^2 + \rho_1^2 + \rho^2 - 2\rho_1\rho(\cos(\theta_1 - \theta))\right]^{3/2}} \rho_1\, d\rho_1\, d\theta_1$$

When δ is equal to zero for all points $\rho > R_o$, and equal to $(-\Delta)$ for all $\rho \le R_o$, the integral over all space reduces to the value for $0 \le \rho_1 \le R_o$ and $\delta\ (= -\Delta)$ may be pulled outside the integral. Further, because the system is in this case cylindrically symmetric, the value of the integral for any value of θ must equal that for $\theta = 0$, such that

$$U(\rho,\theta,z) = U_{bb}\left(1 - \frac{z}{W}\right)^2 + \int_0^{2\pi}\int_0^{\infty} \frac{-\Delta}{2\pi} \frac{z}{\left[z^2 + \rho^2 + \rho_1^2 - 2\rho\rho_1\big(\cos\big(\theta_1 - 0\big)\big)\right]^{3/2}} d\rho_1\, d\theta_1$$

$$\Rightarrow\quad U(\rho,z) = U_{bb}\left(1 - \frac{z}{W}\right)^2 - \frac{\Delta}{2\pi}\int_0^{2\pi}\int_0^{R_o} \frac{\rho_1 z}{\left[z^2 + \rho^2 + \rho_1^2 - 2\rho\rho_1\cos\big(\theta_1\big)\right]^{3/2}} d\rho_1\, d\theta_1$$